Ultra-High-Aspect-Ratio Nanofluidic Channels for High-Throughput Biological Applications

by

Pan Mao

B.S., University of Science and Technology of China, 2002
S.M., Massachusetts Institute of Technology, 2005

Submitted to the Department of Mechanical Engineering in Partial Fulfillment of the Requirements for the Degree of

Doctor of Philosophy

at the

Massachusetts Institute of Technology
September 2009

© 2009 Massachusetts Institute of Technology. All rights reserved

Signature of Author……………………………………………………………………
Department of Mechanical Engineering
August, 2009

Certified by………………………………………………………………………………
Jongyoon Han
Associate Professor of Electrical Engineering and Computer Science
Department of Biological Engineering
Thesis Supervisor

Certified by………………………………………………………………………………
Scott Manalis
Associate Professor of Mechanical Engineering
Department of Biological Engineering
Thesis Committee Chair

Accepted by………………………………………………………………………………...
David E. Hardt
Professor of Mechanical Engineering
Chairman, Department Committee on Graduate Students

Ultra-High-Aspect-Ratio Nanofluidic Channels for High-Throughput Biological Applications

by

Pan Mao

Submitted to the Department of Mechanical Engineering on August 21, 2009 in Partial Fulfillment of the Requirements for the Degree of Doctor of Philosophy in Mechanical Engineering

Abstract

The development of micro/nanofluidics is expected to be the enabling technology for sample preparation of proteomic biosamples, which has been the bottleneck in proteomics. Most microfabricated nanofluidic channels, such as planar nanochannels and square nanochannels, suffer from small open volume and, as a result, low sample throughput, compared to microchips and conventional gel-based systems. For practical and wider applications of artificial nanochannels, it is of crucial importance to enhance sample throughput of nanofluidic systems. To address this severe problem, we proposed to build high-aspect-ratio vertical nanochannels, which have the advantage of large open volume, enabling their use for high-throughput applications.

Two fabrication methods for creating massively-parallel, ultra-high-aspect-ratio nanochannels have been developed by using a combination of anisotropic wet etching and thermal oxidation. Vertical nanochannels with a uniform gap size of 55 nm and aspect ratio as high as 400 have been demonstrated. In addition, we have implemented high-aspect-ratio nanochannels into a two-dimensional anisotropic nanofilter array (ANA) device and demonstrated continuous-flow separation of DNA and proteins. Compared to other nanofilter devices, the vertical ANA device achieves comparable separation speed and efficiency but allows a much higher sample throughput.

Lastly, we have demonstrated the uniform layer-by-layer deposition of polyelectrolyte multilayers (PEM) within high-aspect-ratio nanochannels. Conformal, uniform deposition has been achieved along the entire depth of nanochannel and linear growth has been observed. Compared with the growth on flat substrate, significantly slower deposition per bilayer within nanochannels was found, which we attribute to the partioning effect. We also have performed dc condutance measurement to determine the wet-state thickness of PEM. The ability of uniform growth of PEM inside nanochannels not only allows the control of gap size, but also provides new functionalities with desired surface properties such as surface charge density, charge polarity, and hydrophobicity.

Thesis Supervisor: Jongyoon Han

Title: Associate Professor of Electrical Engineering and Computer Science and Department of Biological Engineering

Dedicated to my family and friends

Acknowledgements

I have been extremely fortunate to have the people around me, who supported, encouraged, and help me throughout my doctoral study, and made this thesis a reality. First and foremost, I owe my deepest gratitude to my thesis supervisor, Professor Jongyoon Han, for his guidance, encouragement, intellectual wisdom, and professional support. I truly appreciate his introducing me to this exciting research area, and he is the mentor who has supported me through difficult times that I faced during my study at MIT.

I would like to give my special thanks to the other members of my thesis committee, Professor Scott Manalis and Professor Carol Livermore, for their time, constructive input, and intellectual support. I also thank my collaborators Professor Robert Cohen and Professor Michael Rubner and their students Jonathan DeRocher and Daeyeon Lee for enjoyable, beneficial interaction and technical support. They introduce me into the exciting world of polymer coating. I am also grateful to have been able to work with Professor Patrick S. Doyle and his student Anthony Balducci for studying DNA dynamics.

I am indebted to my fellow group members in the Prof. Han's laboratory, who have made my graduate student experience wonderful and worthwhile. I would like to thank Jianping Fu, Ying-chih Wang, Yong-Ak Song, Sung Jae Kim, Jeong Hoon Lee, Masumi Yamada, Hansen Bow, Lih Feng Cheow, Aniruddh Sarkar, Leon Li, Sung Hee Ko, Michael Chan, Junmin Lee, Myungji Kim, Hongchul Jang, Chang-Soo Lee, and Arnaud Le Coguic for their help and friendship. I really enjoyed the life at MIT with them and have learned a great deal from them in many different aspects. In addition, I also thank other colleagues, Mike Vahey, Salil Desai, for their kind help both intellectually and emotionally.

I would like to thank MIT Mechanical Engineering Department (especially Ms. Leslie Regan), and Microsystems Technology of Laboratories (Dr. Vicky Diadiuk, Kurt Broderick, Paul Tierney, Bob Bicchieri, Bernard Alamariu) for device fabrication. I also gratefully acknowledge financial support from National Science Foundation (CTS-0347348), NIH (EB005743), DuPont-MIT Alliance, Singapore-MIT Alliance (SMA-II, CE program), and Korea Institute of Science and Technology (KIST) –IMC.

Finally, I would like to express my deepest appreciation to my grandparents, parents, and family for their selfless love and support, as well as to my great friends both in United States and in China for their lifelong friendship and support. Especially, I would like to thank my wife, for her forever love and meticulous care, and for everything.

Table of Contents

List of Figures 11

List of Tables 13

Chapter 1 Introduction 15

1.1 Micro/Nanofluidic Technology for Sample Preparation of Proteomics ... 15

1.2 Artificial Nanostructures 18

1.3 Thesis Objective 21

1.4 Thesis Outline and Scope 23

Chapter 2 Fabrication of Ultra-High-Aspect-Ratio Nanofluidic Channels 25

2.1 Introduction 25

2.2 Fabrication Method I (Non-Conformal Trench Filling) 28

2.3 Characterization of Fabrication Method I 32

2.3.1 Alignment for Finding (111) Planes 34

2.3.2 Etching Defects (Non-Uniform Etch Depth) 36

2.3.3 Control of Gap Size 38

2.3.4 Sealing and Bonding Issues 43

2.4 Fabrication Method II (Conformal Trench Filling) 44

2.5 Characterization of Fabrication Method II 46

2.5.1 Various Trench Sealing Methods 46

2.5.2 Combination of PECVD and LPCVD Processes 50

2.5.3 Micro-Nanochannel Connection 53

2.6 Summary 53

Chapter 3 Vertical Nanofilter Array for Continuous-Flow Separation of DNA and Proteins **55**

3.1 Introduction 55

3.2 Molecular Sieving and Filtering Mechanism 57

3.3 Device Design and Fabrication 60

3.4 Experimental Setup and Sample Preparation 67
3.5 Continuous-Flow Separation of Long DNA 68
3.6 Continuous-Flow Separation of Native Proteins 72
3.7 Sample Throughput of Vertical ANA Devices 75
3.8 Summary 76

Chapter 4 Layer-by-Layer Assembly of Polyelectrolytes in High-Aspect-Ratio Nanochannels 77
4.1 Introduction 77
4.2 Experimental Section 82
4.2.1 Materials 82
4.2.2 Device Fabrication 84
4.2.3 PEM Deposition 89
4.2.4 Multilayer Film Characterization 89
4.2.5 dc Conductance Measurement 90
4.3 Results and Discussion 93
4.3.1 Polyelectrolyte Multilayer Growth in Nanochannels 93
4.3.2 Wet-State Thickness of PEM Film 103
4.3.3 Applications 110
4.4 Summary 113

Chapter 5 Conclusions and Outlook 115
5.1 Thesis Contributions 115
5.2 Ongoing Work 117
5.3 Outlook and Future Direction 121

Appendix I 123

Bibliography 131

List of Figures

Figure 1.1 Schematic illustrating the comparison of the planar (low-aspect-ratio) nanochannel system (a) and vertical (high-aspect-ratio) nanochannel 22

Figure 2.1 Schematic diagram of fabricating vertical nanochannels by the non-conformal trench filling method. 30

Figure 2.2 Schematic showing detailed process flow for fabricating high-aspect-ratio nanochannels.. 31

Figure 2.3 Cross-sectional SEM micrographs of slot-like vertical nanochannels with a uniform gap size of 250 nm, 72 nm, 55 nm, and 30 nm........................... 33

Figure 2.4 Alignment marks for determining the (111) planes of (110) Si wafers. 35

Figure 2.5 Cross-sectional SEM images of 40 μm (**a**) and 120 μm (**b**) deep trenches produced by KOH etching at room temperature 37

Figure 2.6 (a) Schematic showing height difference between the regions of pillars and the plateau after thermal oxidation.. 41

Figure 2.7 Cross-sectional SEM image showing trench sealing by PECVD oxide 42

Figure 2.8 Schematic diagram of fabrication process using the method II of conformal trench filling 45

Figure 2.9 Cross-sectional SEM micrographs showing the behaviors of trench sealing by various deposition methods 49

Figure 2.10 Cross-sectional SEM images of 15 μm deep trenches deposited with 900 nm thick PECVD oxide and 1.37 μm thick LPCVD polysilicon sequentially . 52

Figure 2.11 Tilted-view SEM images showing the interfaces between micro- and nano-channels 54

Figure 3.1 Schematics of a two-dimensional, vertical, anisotropic nanofilter array device 61

Figure 3.2 Schematic of the fabrication process for the vertical ANA device 62

Figure 3.3 Cross-sectional SEM images of 35 μm deep trenches etched by DRIE 63

Figure 3.4 Schematic showing bidirectional motion of negatively charged macromolecules in vertical ANA device in two orthogonal electric fields 65
Figure 3.5 Fluorescence micrograph and intensity profiles showing continuous-flow fractionation of the mixture of λ-DNA Hind III digest 71
Figure 3.6 Fluorescence micrograph and intensity profiles showing continuous-flow separation of the mixture of FITC and R-phycoerythrin 73
Figure 4.1 Schematic showing the concept of layer-by-layer assembly of polyelectrolytes 78
Figure 4.2 Schematic showing the fabrication process of nanofluidic-PEM channels 83
Figure 4.3 (a) Schematic and SEM images of the device used for the dc conductance measurement 87
Figure 4.4 Cross-sectional SEM micrographs showing nanochannel arrays coated with 40 bilayers of PAH/SPS after plasma etching of 2 minutes (a) and 5 minutes (b) 88
Figure 4.5 Scanning electron micrographs depicting conformal coating of 20 (a), 40 (b), 39 (c) bilayers of PAH/PSS in an open nanochannel array 95
Figure 4.6 Comparison of dry state PEM thickness outside of and inside of a nanochannel with PEM thickness grown on flat surface 96
Figure 4.7 Comparison of dry-state PEM thickness in channels and on a flat surface at different ionic strengths 98
Figure 4.8 Representative *I-V* curves to determine the gap size of nanochannels 104
Figure 4.9 Comparison of the final gap sizes of nanochannels obtained by dc conductance measurement in 0.2M (red triangle), 1M (green square), 3M KCl (blue circle) 106
Figure 4.10 Comparison of dry-state (diamonds) and wet-state (circles) multilayer thickness both on flat substrate (open) and in nanochannels (filled) 109
Figure 4.11 The high-throughput concentration device 112
Figure 5.1 The concept of integrated multi-scale continuous-flow sorter 118

List of Tables

Table 4.1 Bilayer Thickness 97
Table I Troubleshooting Table 128

Chapter 1

Introduction

1.1 Micro/Nanofluidic Technology for Proteomic Sample Preparation

Proteomic sample preparation refers to isolating proteins of interest from complex biological cells or organisms before downstream biosensing. A series of fractionation, purification, and concentration steps (often multiples of each) are required to obtain high sensitivity and specificity of detection. One of the major challenges in sample preparation is that proteomic samples are complex, diverse, and often scarce. They contain analytes spanning an enormous dynamic range of relative abundance, and usually contain large quantities of contaminants, salts, and surfactants (*1*). The dynamic range, defined as the relative difference between the most and least abundant proteins, could be over 10^6 and even 10^{10} in plasma proteins (*2*). What makes it worse is that the proteins of most interest are often the least abundant. The unusually high abundance of some serum proteins (such as albumin and immunoglobulin G) can significantly affect the detection of low-abundance proteins in immuno-biosensors. Hence an important part of the sample preparation process is to remove extraneous proteins present in high abundance. The large numbers of background proteins and tremendous differences in their physical properties demand that separation techniques be of the highest efficiency and the broadest range of

applicability. Additionally, although polymerase chain reaction (PCR) technology works for DNA detection, no similar method is available to amplify proteins. Therefore, sample preparation has been and will continue to be the bottleneck in proteomics (*1*).

Currently two-dimensional gel electrophoresis (2D PAGE) (*3-5*) and multi-dimensional liquid chromatography (LC) (*6, 7*) , coupled with mass spectrometry (MS), are routinely used for broad proteomic separations. Both techniques demonstrate the separation peak capacity of ~ 3000 and dynamic range of detection (~ 10^4), which is, however, not enough to profile low-abundance but information-rich proteins that exist in blood serum (*1, 2*). In addition, they require manual, lab-intensive, and time-consuming sample-handling steps, leading to challenges in automation of sample preparation systems and further decreasing throughputs of proteome analysis. For example, in 2D gel electrophoresis, recovery of the separated sample is often problematic and inefficient: the location of the band in the gel must be physically cut out, and additional washing steps are necessary to extract the desired sample from the gel, which often leads to significant sample loss. In the meanwhile, substantial efforts have been made to develop alternative separation techniques, such as various capillary electrophoresis (CE) (*8-10*). The challenges here lie in separation capabilities, recovery of material, and throughput. Typically it is necessary to concentrate or enrich separated samples before the detection step, especially for detection of low-abundance proteins. Integration and automation are the keys to truly widespread acceptance and utilization of any sample preparation technique (*11*). However, none of these conventional separation technologies satisfies all the above-mentioned requirements.

Recent advances in micro- and nanofluidic technologies have opened up new opportunities for sample preparation of proteomics because they promise low sample consumption, miniaturization, automation, and easy integration into micro total analysis systems (µTAS), aiming at integrating all steps of biological/chemical analyses in one single chip (*12-14*). Various microchip-based gel electrophoresis (*15, 16*), capillary electrophoresis (*9, 17-19*), and chromatography techniques (*20-22*) as well as amplification techniques (*23-25*) have been demonstrated with similar or better performance to conventional techniques. The versatile integration methods of different components or functions on chip, such as combination of preconcentration and separation steps (*26, 27*) and large scale integration (*28*), have also been developed. However, most of these microfluidic systems still utilize conventional polymeric gel materials as sieving matrix for separation and preconcentration, which are randomly disordered and whose physical and chemical properties are difficult to control and manipulate. Furthermore, these foreign nanoporous gel materials have intrinsic challenges for the integration of automated multi-step chip-based bioanalysis systems. Over the last decades, there have been numerous efforts to develop regular artificial nanofluidic structures, aiming as a promising alternative to disordered gel materials to achieve better performance in separation and preconcentration (*29-31*). The advantages of patterned regular structures include the design flexibility and precise control on structural parameters and geometries. Exciting examples include growing interests on the fabrication of anisotropic sieving structures for continuous fractionation of biomolecules (*32, 33*), in contrast with isotropic gel media. With amenability to

miniaturization, automation, and seamless integration, the micro/nanofluidic technology would become the enablers for efficient sample preparation of proteomics.

1.2 Artificial Nanostructures

To realize them as a substitute for gel materials which consist of cross-linked nanometer-sized pores, it is not difficult to recognize that artificial structures have to be created with the critical feature size (at least one dimension) comparable to the molecular scale. Spurred by the applications in sample preparation of proteomics, various top-down and bottom-up fabrication techniques of regular nanostructures have been developed (*34, 35*). Nuclear track-etched membrane (NTE membrane) is one of the first artificial membranes widely used for various filtration applications, and its development dates back to the early 1970s (*36*). NTE membranes are generated by irradiation of plastic films (polycarbonate (PC) or polyethylene terephthalate (PET)) with a highly energetic beam of heavy fission fragments. The energetic particles produce damage tracks in the material to allow a highly directional subsequent chemical etching. The pore number density and pore radius are controlled by the particle dose and etching conditions, respectively, and therefore can be varied independently. The drawback of these membranes is the difficulty to integrate them with other fluidic systems.

In contrast, conventional semiconductor microfabrication techniques have been implemented to create nanofluidic structures with seamless integration to microfluidic and other systems. One straightforward way would be using nanolithography tools,

such as e-beam, focused ion beam, and x-ray lithography, to define narrow channels with nanometer-sized lateral dimensions. For example, Turner *et al.* used a monolithic sacrificial etching technique combined with e-beam lithography to generate ~50 nm fluidic obstructions (*37*). Austin *et al.* used focused ion beam (FIB) lithography to fabricate 50 nm nanoslits (*38*). These nanolithography-based techniques allow precise control of channel dimensions and positions with a resolution as high as a few nanometers, but are very expensive and time-consuming. Instead of fabricating very narrow channels as nanolithography techniques accomplish, an easy alternative way is to make shallow but wide channels, referred as planar nanochannels. The advantage of this approach is that, compared to a channel width, the channel depth can be much easily controlled and machined smaller in a rather inexpensive way, e.g., by chemical etching. This technique was explored by Han *et al.* (*39*), and successfully applied to biomolecule separation. Recently, this technique has been fully characterized to provide accurate planar nanochannels as shallow as 20 nm (*40*). However, one critical bottleneck of this technique is that these planar nanochannels exhibit extremely small open volume (sample processing volume), and as a result, much lower sample throughput, compared with microfluidic systems and traditional membrane materials such as gels. For practical applications of artificial nanochannels, it is of great importance to enhance sample throughput of nanofluidic systems.

Alternative fabrication strategies, including self-assembled colloidal particle packing (*41*) and micro/nanofabricated ultra-thin membranes (*42, 43*), have been explored to provide high-throughput applications. Zeng and Harrison used a self-

assembled silica bead array confined in microfluidic channels as the sieving matrix to separate both DNA and proteins (*41*). Close-packed beads create a three-dimensional array with holes (openings) with a diameter of approximately 15% the size of the bead and hence the pore size is tunable by varying bead sizes. Sample throughput can be further increased by simply enlarging the dimensions of microchannels, similar to liquid chromatography system. One drawback of this bead array system is that there is no control in the orientation of nanofilters and it lacks the flexibility in integration with other microfluidic systems. Another interesting approach is to create ultra-thin membranes, whose thickness is comparable to the pore size of tens of nanometers such that the transport rate of molecules across membranes can be significantly enhanced. Using focused ion beam (FIB) drilling, Tong *et al*. (*42*) produced an ultra-thin silicon nitride membrane with a thickness of 10 nm and a uniform cylindrical pore diameter of 25 nm. A more recent exciting development of relatively inexpensive ultra-thin porous membranes have been demonstrated by Striemer *et al*. (*43*). Using standard microfabrication techniques, the authors were able to fabricate a 15-nm-thick porous nanocrystalline silicon (pnc-Si) membrane with a narrow pore size distribution and a well-defined average pore size that ranged from 5 to 25 nm. Although the 200×200 μm^2 pnc-Si membrane was shown to sustain several bars of transmembrane pressure without fracturing, the structural rigidity of ultra-thin membranes remains an issue because of the nature of thinness. In addition, these techniques still fall short of providing enough flexibility to integrate nanofilters within microfluidic systems in an arbitrary or carefully-designed manner, which may be critical to provide advanced functionality.

1.3 Thesis Objective

An ideal artificial nanofluidic structure would be robust and allow high sample throughput. It would be scalable for large-scale applications, and it would also allow easy integration of nanofilters / nanopores with other microchannels / micropores in an arbitrary way. In this thesis, we propose to build high-aspect-ratio (ratio of depth to width) vertical nanochannels to meet these requirements, in particular addressing the challenges of low sample throughput in nanofluidic systems. **Figure 1.1** shows the conceptual comparison of the planar nanochannel and vertical nanochannel systems. The cross-sectional flow area (open pore volume per unit length) of the vertical channels could be more than hundreds of times higher than that of the planar channels. Therefore, the sample throughput (volume flow rate) of the vertical nanochannel system could be a few orders of magnitude higher than the one of the planar nanochannel system assuming a similar flow velocity, while they possess the similar device characteristics due to the same critical dimension. This can also be recognized by the fact that, compared to the planar system, the vertical system makes the most of material usage and resemble more closely the gel matrix with the exception of using well-engineered structures rather than the disordered pore networks.

Fabrication of high-aspect-ratio nanochannels usually requires both high-resolution nanolithography and anisotropic etching of deep trenches (*35*). For example, Kendall used e-beam lithography and anisotropic KOH etching for generating very narrow (0.6 μm wide), deep (~44 μm) trenches on Si substrate (*44*). However, expensive and time-consuming e-beam lithography greatly limits the capability for large-scale

applications. The goal of this thesis is to develop inexpensive methods to create high-aspect-ratio nanochannels with standard microfabrication techniques as well as utilize them for high-throughput biological applications.

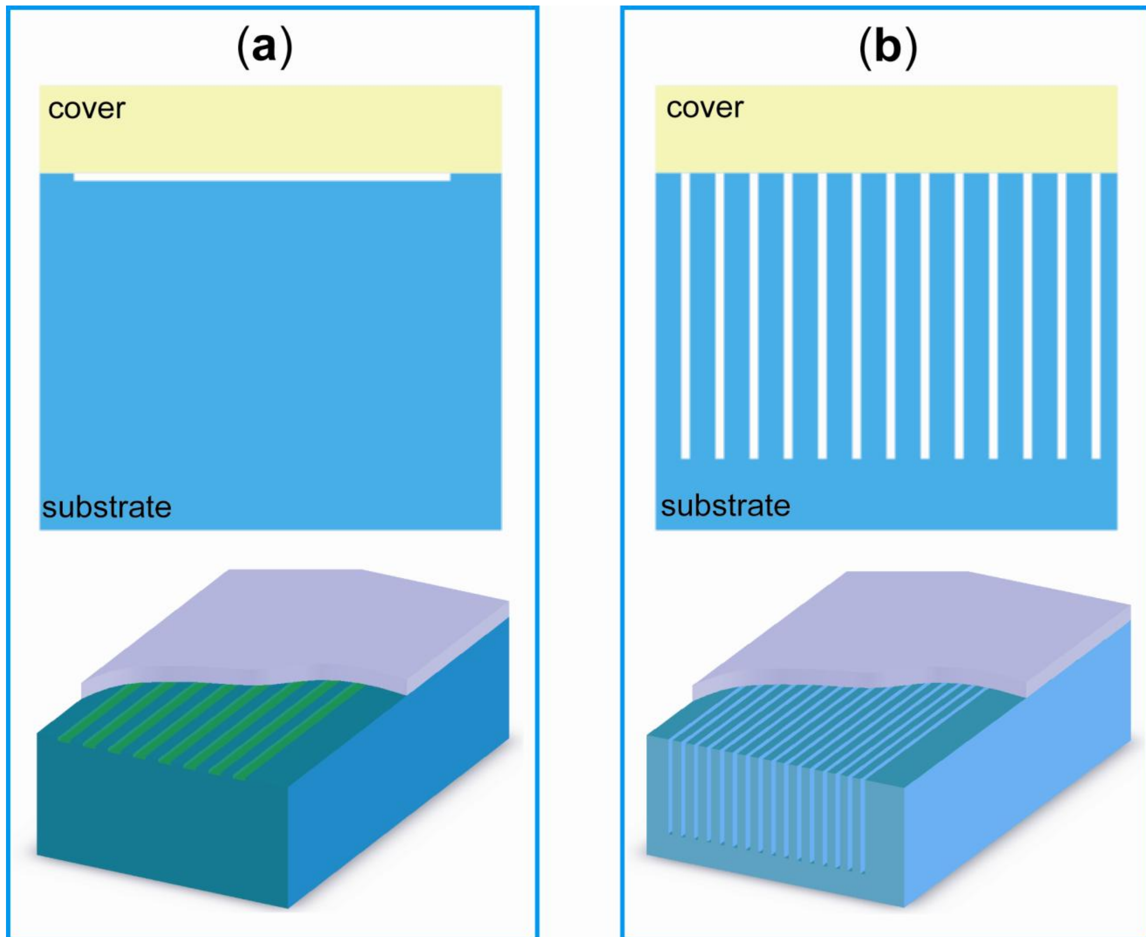

Figure 1.1 Schematic illustrating the comparison of the planar (low-aspect-ratio) nanochannel system (**a**) and vertical (high-aspect-ratio) nanochannel system (**b**). They both have the same critical dimension (depth for planar channels and width for vertical channels) but the open volume of vertical channels can be more than a hundred times larger than that of planar channels.

1.4 Thesis Outline and Scope

In recognizing the crucial importance of high throughput in sample preparation because of the large number of proteins involved, we have developed fabrication techniques for creating high-aspect-ratio nanochannels to address the challenges of low sample throughput suffered in current nanofluidic systems. These ultrahigh-aspect-ratio nanochannels have the advantage of large open volume, enabling their use for high-throughput applications.

Chapter 2 describes two novel fabrication methods for creating ultrahigh-aspect-ratio nanochannels with well-controlled gap sizes by using only standard semiconductor microfabrication techniques. The uniformity of gap sizes of vertical nanochannels and the limitations of these techniques have been characterized. Also, the ability to seamlessly integrate micro-sized and nano-sized channels is demonstrated.

In Chapter 3, we describe the design and fabrication of a two-dimensional vertical anisotropic nanofilter array (ANA) device and demonstrate its implementation for continuous-flow separation of large DNA and proteins. The designed structural anisotropy of the ANA causes biomolecules of different sizes and charges to follow distinct trajectories, leading to efficient continuous-flow separation. The sample throughput in vertical ANA device can be as high as µL/hour.

In Chapter 4, layer-by-layer assembly of polyelectrolyte multilayers (PEM) is introduced and employed to coat high-aspect-ratio nanochannels to form novel nanofluidic-PEM channels. The growth of multilayers not only provides new functionalities on the nanochannel surface, but also an alternative way to reduce the

gap size of nanochannels in a well-controlled manner. In addition, dc conductance measurements are performed to obtain wet-state PEM thickness, which is compared with dry-state thickness measured by SEM.

Chapter 5 summarizes the thesis contributions and presents ongoing works as well as future directions.

Appendix I shows the detailed fabrication procedure for making the 2D vertical ANA device as well as a guide for trouble shooting.

Chapter 2

Fabrication of Ultra-High-Aspect-Ratio Nanofluidic Channels

2.1 Introduction

In order to build high-aspect-ratio structures shown in **Figure 1.1**(**b**), a method to etch the substrate preferentially in one direction (anisotropic etching) would be needed. Anisotropic etching is one of the oldest techniques used in silicon micromachining and MEMS. The etch rate of silicon in some aqueous etchants such as potassium hydroxide (KOH), tetramethyl ammonium hydroxide (TMAH) and ethylenediamine based solutions (EDP) greatly depends on the crystallographic orientation of the etched surface. Etching of (111) crystallographic planes is extremely slow compared with other planes. Anisotropic wet etching of (110) silicon provides an attractive and effective method for fabrication of high-aspect-ratio structures with smooth and vertical sidewalls because of the high selectivity between (110) and (111) planes (larger than 100:1) (*44-46*). The ability to etch high-aspect-ratio structures with high precision offers numerous possibilities of technological application including the fabrication of sensors and actuators (*45, 47*). As early as in 1975, Kendall used KOH etching for generating very narrow (0.6 μm wide), deep (~44 μm) trenches on Si wafers (*44, 48*). However, expensive and time-consuming e-beam lithography would be needed to pattern narrow

channels for subsequent KOH etching, if one were to generate nanochannel membrane structures needed for biomolecule separation.

Electrochemical etching of silicon in hydrofluoric acid (HF) is a well-known technique for the formation of high-aspect-ratio micro/macroporous silicon (*49-52*). Anodic dissolution of n-type Si in an HF containing solution requires a supply of holes to the surface. Often illumination is used to generate holes in the backside of silicon substrate as well as to provide directionality in etching. Under anodic biasing conditions, the photo-generated holes are prone to move towards the sharp spots such as surface defects, pore tips, and pre-etched initial pits, where the electrical fields concentrate. This causes a much faster etch rate vertically than on pore sidewalls. The macropore morphology highly depends on anodization conditions (current density, HF concentration, bias, temperature) and substrates (doping and orientation). Using this technique, Létant *et al.* fabricated nanochannel arrays with the diameter of 30 nm and aspect ratio up to 250 (*53*). The limitation of this technique has been discussed by Lehmann *et al.*, including macropore diameter, pore depth, pore growth direction, and pore patterns (*52*). It still remains quite challenging in formation of reproducible, defect-free, and uniform macropores.

Deep reactive ion etching (DRIE) is another popular technique widely used in MEMS fields. The Bosch process consists of alternating the etching and passivating steps, enabling anisotropic dry etching of silicon trenches (*49*). Compared to wet etching, DRIE does not have an inherent restriction on silicon substrate (type and orientation) and allows much more flexibility on pattern geometries and profiles. Careful tuning of

etching parameters produces almost vertical sidewalls (~89°). However, the typical sidewall roughness (scallops), inherent from the Bosch process (lateral etching), is about tens of nanometers or even more than hundreds of nanometers (*54*). This prevents the possibility of producing nanochannels with uniform trench widths down to 50 nm. Besides, DRIE technique has demonstrated poor applicability in etching sub-micrometer wide trenches while maintaining vertical sidewalls and small surface roughness (*55*). Mogensen *et al. (56)* reported the fabrication of high-aspect-ratio 500-nm-wide channels by DRIE and thermal oxidation. The aspect ratio of 150 was achieved but the gap size (lateral trench width) was non-uniform due to the surface roughness mentioned above.

In this chapter, we describe two novel fabrication strategies for creating ultrahigh-aspect-ratio nanochannels by using conventional semiconductor microfabrication techniques. Channel patterns are defined by standard photolithography instead of high-resolution nanolithography such as e-beam or x-ray lithography. Anisotropic KOH etching is performed to generate high-aspect-ratio trenches, followed by thermal oxidation which narrows the gap size (trench width) down to the desired value (< 100 nm). These fabrication processes are inexpensive and simple, without any nanolithography and other special tools, and can be well controlled. In addition, these methods allow much flexibility and easy system integration, and it is straightforward to create massively-parallel nanochannels for large-scale membrane applications (*57*). In the first method, non-conformal trench sealing is done by CVD oxide deposition after thermal oxidation, which applies to the situation where the

device dimensions are small. The second method, where conformal trench sealing takes place before thermal oxidation, is more complicated but does not have constraints on device dimensions. Hence, it allows easy connection between micro- and nano-channels and much more flexibility in device design and fabrication.

2.2 Fabrication Method I (Non-Conformal Trench Filling)

Anisotropic KOH etching is chosen to produce high-aspect-ratio channels over DRIE and electrochemical etching since it allows smooth surface and vertical sidewalls, and can be easily controlled, and is reproducible. Alternatively, DRIE technique can also be used to achieve deep channels with Bosch process, but a short period of KOH etching step should be followed to smooth the rough sidewall scallops resulting from the DRIE process, which further enlarges the trench width (*58*). The overall fabrication process as well as detailed process flow for creating massively parallel, vertical nanochannels is outlined in **Figure 2.1** and **2.2**, respectively. Commercial p-type Czochralski grown 6" (110) wafers with a resistivity of 10-20 Ω cm and a thickness of 625 μm are used (El-CAT, Inc., NJ). First, a thin layer of low-stress low-pressure chemical vapor deposition (LPCVD) silicon nitride is deposited on the (110) silicon substrate to provide an etch mask for KOH etching. Both the fan-shaped and diamond-shaped alignment marks for determining the direction of (111) planes are patterned and etched in aqueous KOH solution to a depth of more than 30 μm. Then channel patterns are defined by standard photolithography and etched to form narrow, deep trenches by anisotropic KOH etching (**Fig. 2.1a, b**). The features in this step must be aligned to the (111) planes of silicon within 0.1 degree. The

etch rate of (110) planes in 44 wt% KOH is around 75 nm min^{-1} at room temperature without stirring. After KOH etching, the sidewalls will end up with smooth, vertical (111) planes, which is important for ensuring nanochannel uniformity in the downstream oxidation process. It is well known that thermal oxidation process of Si results in a volume expansion of about a factor of 2.3, which can be used for reducing the trench widths in a highly controlled manner. After removal of the silicon nitride layer, scanning electron microscopy (SEM) is used to measure the gap size (trench width) in order to determine the necessary oxide thickness. Based on this gap size, an oxide layer with appropriate thickness is grown to narrow the gap down to below 100 nm or even 10 nm (**Fig. 2.1c**). Finally, non-conformal PECVD (plasma-enhanced chemical vapor deposition) oxide deposition is performed to seal the trenches and form closed vertical nanochannels (**Fig. 2.1d**). Alternatively, the backside of the wafer can be etched to make a thin, vertical membrane across the Si wafer, if such geometry is preferred (**Fig. 2.1d**). Using this method, one could fabricate a large area of membranes with regular pores if needed.

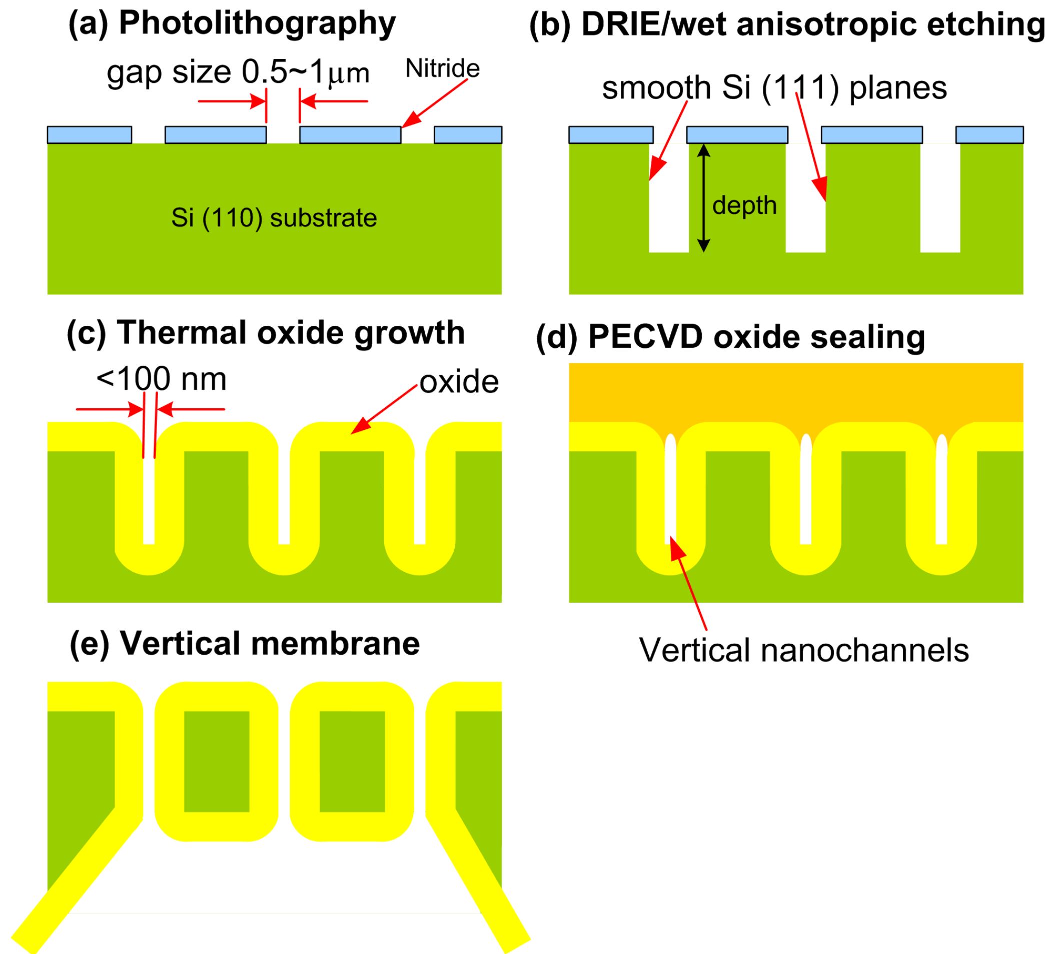

Figure 2.1 Schematic diagram of fabricating vertical nanochannels by the non-conformal trench filling method. (**a**) Photolithography defines pattern structures. (**b**) Vertical trenches with smooth sidewalls are etched by either DRIE or anisotropic wet etching (KOH). (**c**) Thermal oxide growth further decreases the gap size. (**d**) Uniform PECVD oxide is deposited to seal narrow trenches. (**e**) Alternatively, backside etching of Si wafer yields thin membranes over a large area (~6 inch wafers).

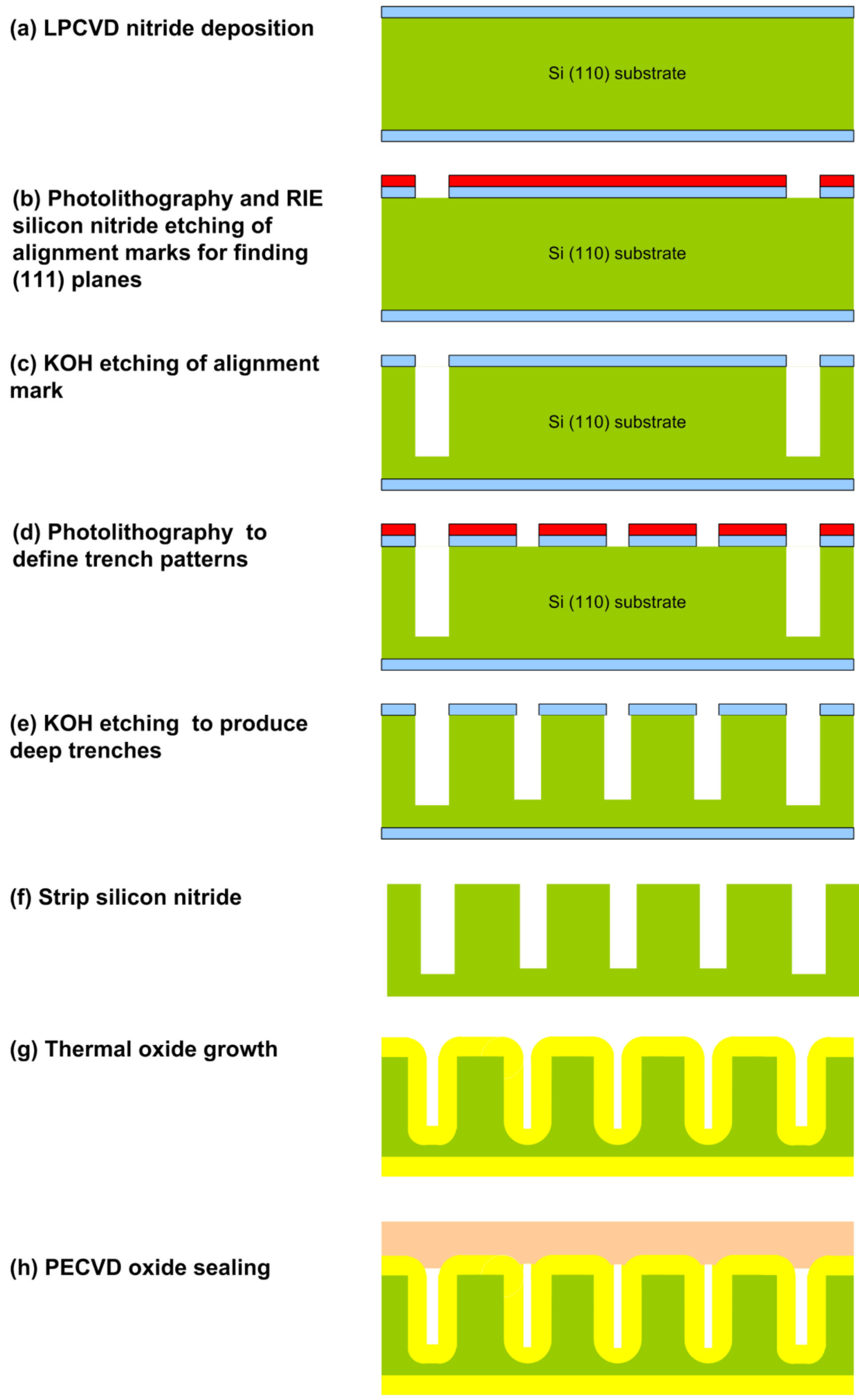

Figure 2.2 Schematic diagram showing detailed process flow for fabricating high-aspect-ratio nanochannels.

2.3 Characterization of Fabrication Method I

We have been able to fabricate 28 µm deep, slot-like nanochannel arrays with a uniform gap size (lateral trench width) as narrow as 72 nm, even down to 30 nm throughout the depth of the trench, as shown in **Figure 2.3**. Compared with fabrication of high-aspect-ratio sub-micrometer channels with DRIE process reported by Mogensen *et al*. (*56*), our strategy allows to produce nanostructures with much higher aspect ratio and a smaller, more uniform nanofilter gap size by minimizing the sidewall roughness during the vertical etching process. The aspect ratio (depth-to-width ratio) of the vertical nanochannels can be as high as 400. The depth of the nanochannel can be further increased to at least 40 µm (**Fig. 2.5a**) with the current process techniques. Nanochannel gap uniformity achieved is typically better than 5~10% across the entire 6" wafer as well as along the depth of the trench, which is believed to be adequate for the biological applications such as biomolecule sorting. In fact, it has been demonstrated that proteins of ~ 10 nm in size can be separated by much larger nanofilters (~ 55 nm) with Ogston sieving (*59*).

During the characterization process, special care should be taken for a few technical issues, which are described in the following.

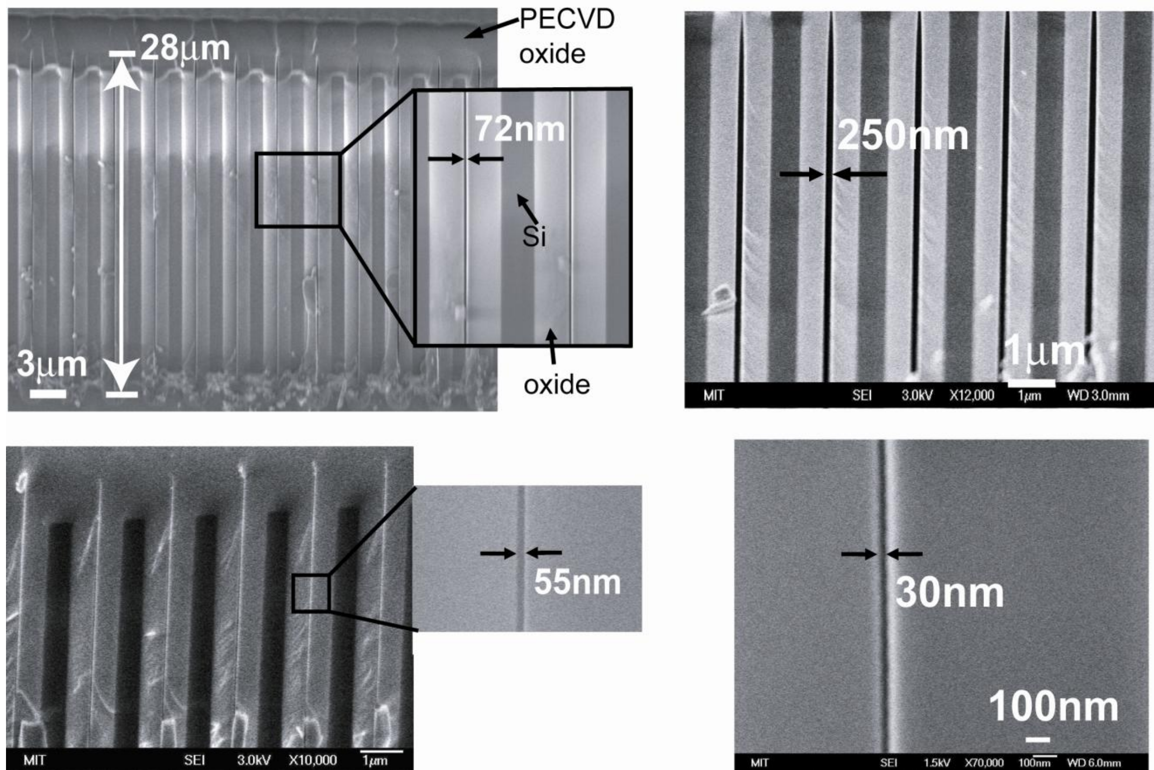

Figure 2.3 Cross-sectional SEM micrographs of slot-like vertical nanochannels with a uniform gap size of 250 nm, 72 nm, 55 nm, and 30 nm, respectively. The channels are produced by KOH etching and have a depth of 28 μm. The channels are completely sealed by depositing 3 μm thick PECVD oxide.

2.3.1 Alignment for Finding (111) Planes

Precise alignment of the features to the true (111) planes is of critical importance for achieving high-aspect-ratio structures. It has been confirmed by previous researchers that precise alignment within 0.1 degree is required to obtain high anisotropy ratio in KOH etching (*44-47*). This requirement is an order of magnitude smaller than the accuracy of the major flat of commercially available (110) silicon wafers, which is typically 2 degrees. We used both fan-shaped and diamond-shaped alignment marks, reported by Uenishi *et al.* (*45*) and Hölke *et al.* (*46*), respectively, for finding the minimum under-etch of the (111) planes, as shown in **Figure 2.4**. For the fan-shaped alignment pattern, the (111) planes can be determined by examining the narrowest line after wet etching, where minimum underetching takes place (**Fig. 2.4a**). The diamond-shaped window is etched anisotropically, until it ends up with a hexagon bounded by the (111) planes (**Fig. 2.4b**). Hence the pattern will be aligned between the resulting top and bottom lines of the etched window, which represent the (111) planes with the smallest possible rate.

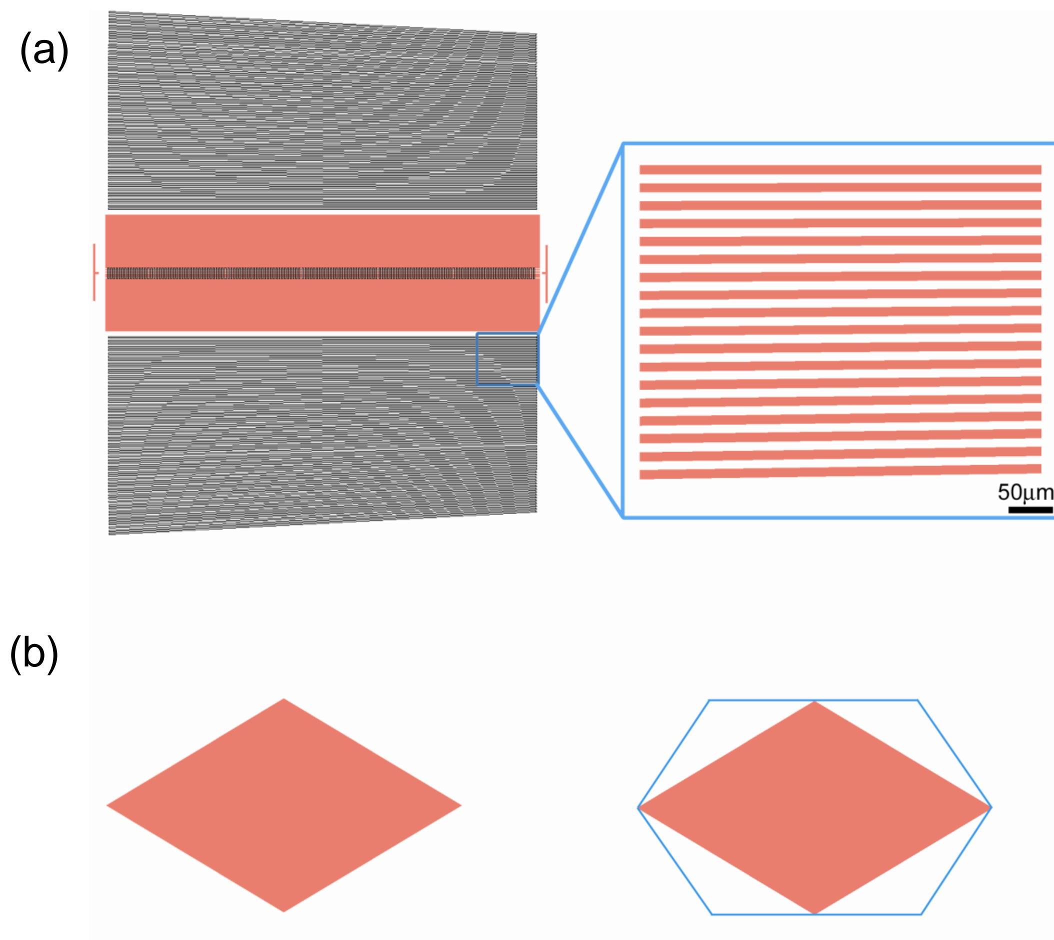

Figure 2.4 Alignment marks for determining the (111) planes of (110) Si wafers. **(a)** A fan-shaped pattern consists of 3 mm long and 10 µm wide lines spaced by 10 µm, which fan out at 0.05 degree angles to one another and span from -2 degrees to 2 degrees. The most narrow line with the minimum undercut represents the real (111) plane. **(b)** A diamond-shaped window. The final etch pattern of the diamond shaped window is defined by the intersection of (111) planes.

2.3.2 Etching Defects (Non-Uniform Etch Depth)

In this technique, KOH etching is performed at room temperature in contrast to conventional high temperature etching (~70 ^{o}C) (*44*). We have found out that etching at high temperature tends to form trenches of non-uniform depths with the same widths, as shown in **Figure 2.6c**. This non-uniformity in depth further causes a serious problem of non-uniform gap sizes after thermal oxidation, caused by uneven expansion and distortion of oxide film. Therefore, it is important to produce channels with uniform depths in order to achieve a uniform gap size. KOH etching at room temperature can produce highly uniform channel depths, as shown in **Figure 2.5**. The major cause for such nonuniformity might be gas bubbles generated on the silicon surface during the etching process. When bubbles get trapped and remain in a narrow trench, the etch rate in that particular region would be hindered significantly (*60*). High temperature etching generates a much larger quantity of bubbles (due to higher etch rates) than low temperature process. Hence it has higher possibility that some bubbles could not get out smoothly and then retard the etch rate in those channels. It has been reported that dynashock-type ultrasonic waves can be used to obtain uniform groove depth independent of pattern widths and spacing by Ohwada *et al.* (*60*). The cavitation effect of ultrasonic oscillation smoothly promotes the bubble detachment and return current during etching process at high temperature. We attempted KOH etching at 70 ^{o}C in ultrasonic cleaner (40 kHz), but no improvement on uniformity of trench depth was observed. We also observed more surface damage due to ultrasonication (data not shown here).

In contrast, at low (room) temperature etching, the non-uniformity of trench depths is greatly improved, which allows us to produce deeper trenches by simply increasing KOH etching time. In fact, we were able to produce 120 μm deep trenches uniformly (**Fig. 2.5b**), where the maximum attainable depth is limited only by the slow etching of the sidewall (111 plane).

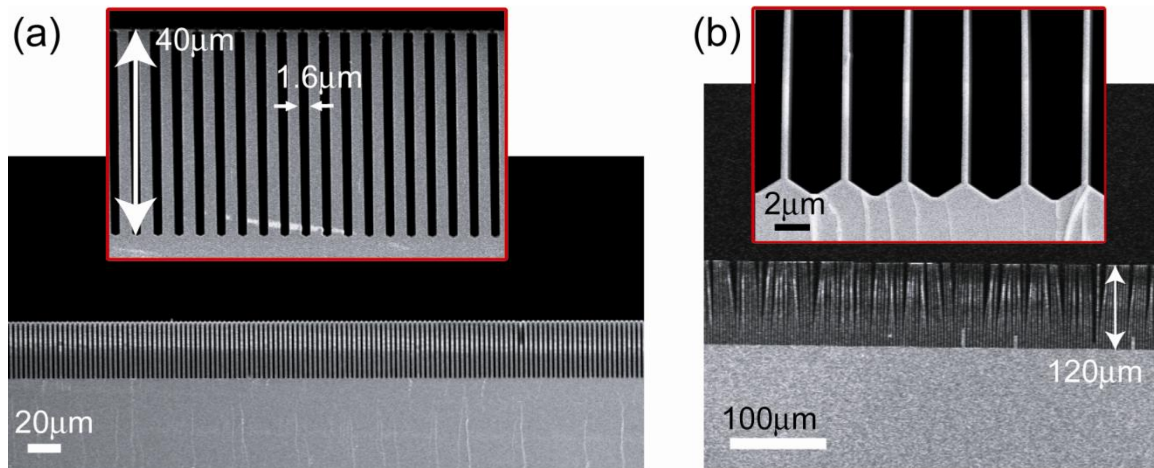

Figure 2.5 Cross-sectional SEM images of 40 μm (**a**) and 120 μm (**b**) deep trenches produced by KOH etching at room temperature. The uniform trench depth has been achieved. In (**b**), some of slot structures collapse and adhere to neighboring ones because of structural instability.

2.3.3 Control of Gap Size

Another important issue is the control of the gap size (trench width). In this technique, the gap size is controlled by growing the approximate thickness of thermal oxide. The typical gap size variation is less than 5% across the 6" wafer. Although the one dimensional thermal oxidation of silicon is described by the well-known Deal-Grove model and can be controlled very well, the oxidation of two-dimensional (2D) or three-dimensional (3D) structures, such as slots and pillars, is more complicated and the oxidation rate is pattern-dependent (*61*). Kao *et al*. (*62, 63*) quantitatively demonstrated that the oxidation of curved silicon surfaces is retarded at sharp curvatures and the retardation becomes more severe on concave than convex structures. They also developed a new model which includes the viscous stress effects caused by two-dimensional viscous flow of the oxide. In the case of planar oxidation, this stress can be released in growth directions. In curved surface, however, a stress perpendicular to the interface occurs (**Fig. 2.6b**) (*64*). We have found out that the oxide of the top surface of silicon pillars is around 50 nm thicker than the oxide on planar surface with a nominal (planar) oxide of about 1 μm in thickness grown, as shown in **Figure 2.6a**. More importantly, this step height will cause a significant problem of failure in traditional bonding methods such as anodic bonding. We also believe that this pattern-dependent oxidation is due to the complex thermal stress during oxidation process. In fact, we observed the non-uniform gap size of a channel when it is shallower than its neighboring channels, as shown in **Figure 2.6c**. The structures seem to be distorted and bent, resulting in a larger gap size. We think this structural asymmetry

results in an inequality of stress in these two walls during thermal oxidation and further the distortion of the structure. Therefore, it is important to produce deep channels with uniform depths in order to achieve uniform gap sizes.

The pattern-dependent oxidation behaviors of 2D or 3D silicon structures could cause challenges in precise control of the final gap size of nanochannels, which demands careful theoretical modeling and numerical simulation of oxidation process as well as experimental investigation to better understand this problem. However, based on both theoretical prediction of planar oxidation and our experimental characterization data, we have been able to control the final gap size of nanochannels within ~5 nm as well as down to ~40 nm by the following procedure. First, the desired oxide thickness is pre-determined by the following calculation: (the original gap size – the desired final gap size)/1.08, where the original gap size of vertical channels is determined by looking at the top-view SEM of the wafer. The corresponding oxidation time can be roughly estimated by the well-known Deal-Grove model of planar oxidation, and then should be correlated for correction with the previous experimental data on oxidation of similar structures. If such data is not available, multiple oxidation processes are often needed to achieve the approximate oxide thickness. The ability of taking wafer-scale SEM images allows us to fabricate the nanochannels with a desired, reproducible gap size without slicing or sacrificing Si wafers. On the other hand, our high-aspect-ratio silicon trenches provide a good experimental platform as well as theoretical model to study these complicated problems of oxidation, which might be explored in the future.

It was previously reported that the oxidation rate deep down in the trench could be retarded due to hindered transport of oxidizing species (*65*). In such cases, the gap size might become non-uniform, especially for very narrow, deep trenches, due to this effect. However, in many applications or situations where the nanochannels are connected to the microchannels or even open reservoirs, the gas species can transport to the nanochannels from the side (connection of microchannels), besides from the top entrance. Therefore, hindered transport of species will have less influence on oxidation process and the limitation can be pushed further.

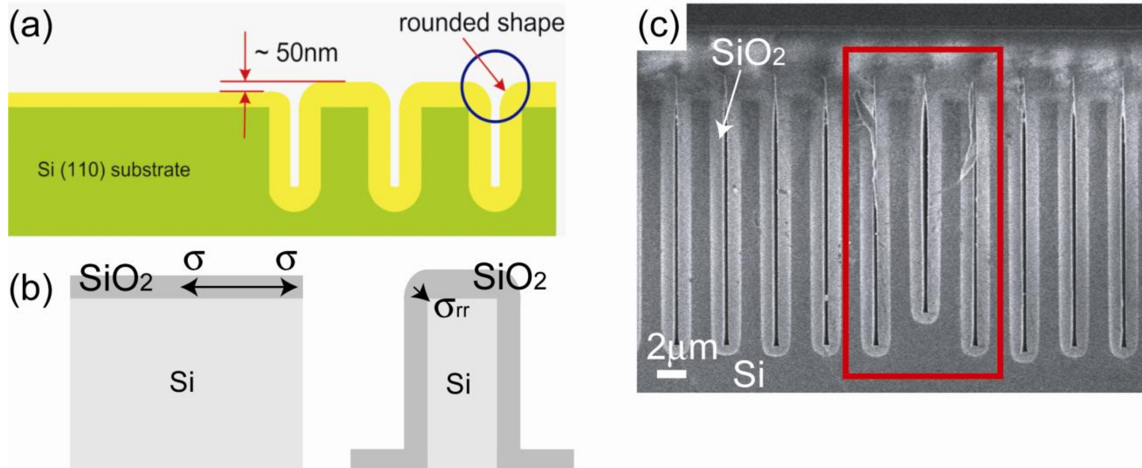

Figure 2.6 (**a**) Schematic showing height difference between the regions of pillars and the plateau after thermal oxidation. The step height is about 50 nm measured by surface profilometer after the 500 nm thick oxide is grown. The rounded shape in the corner is formed due to the edge effect during oxidation process. (**b**) The stress distributions in the thermal oxidation process for the structures of planar surface and slots/pillars. In the case of planar surface, there is no stress perpendicular to the reaction interface. For oxidation of slots or pillars, a stress perpendicular to the reaction interface occurs. (**c**) Cross-sectional SEM image showing the non-uniform gap size after oxidation. The designated trench is shallower than the neighbor ones as a result of KOH etching at high temperature (70 °C). The structural asymmetry causes distortion due to an inequality of stress acting on two channel walls in thermal oxidation process.

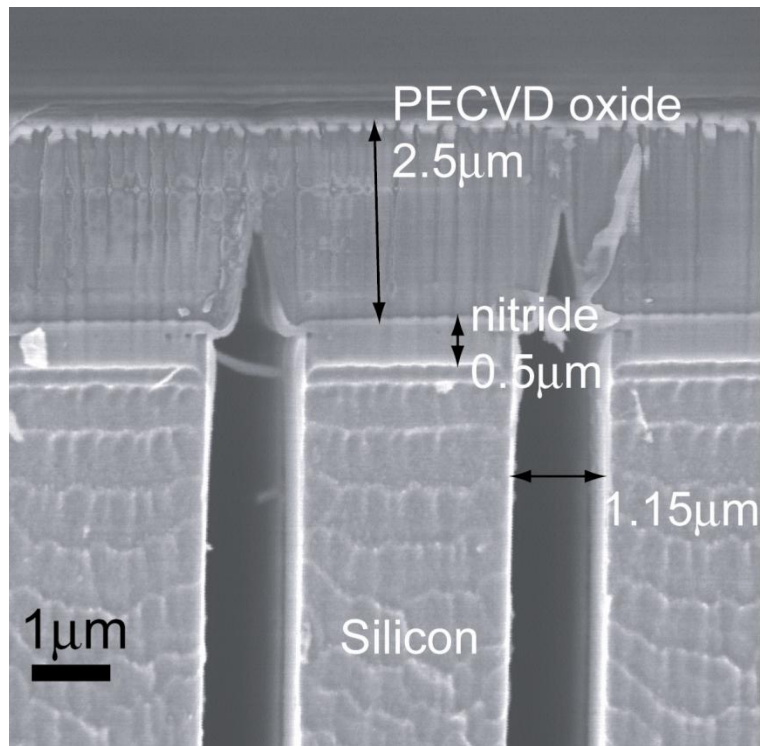

Figure 2.7 Cross-sectional SEM image showing trench sealing by PECVD oxide. The gap size of trenches is 1.15 μm and the thickness of PECVD oxide layer is 2.5 μm.

2.3.4 Sealing and Bonding Issues

Nanochannels are sealed to make enclosed channels by non-conformal oxide deposition from the top. This oxide deposition step serves three purposes. Firstly, it is to seal trenches and to form micro/nanochannels. The non-conformal PECVD oxide deposition is chosen because of its high deposition rate, enabling one to deposit a thick (~10 µm) film within an hour. As shown in **Figure 2.4**, nanochannels can be completely sealed by 3 µm thick PECVD oxide without defects. We also have found that trenches with widths less than 1.5 µm can be easily sealed by 2~5 µm thick PECVD oxide (**Fig. 2.7**). Another benefit of PECVD process is that almost no deposition takes place in the sidewalls so that the uniform gap size of vertical nanochannels will not be affected by the deposition process. Secondly, PECVD oxide sealing is able to eliminate the rounded shape emerging from oxidation process and keep the gap size uniform along the trenches, as shown in **Figure 2.6a**. Lastly, trench-filling eliminates the need for substrate bonding process, which tends to become very challenging or even unfeasible especially with a thick oxide film on the silicon substrate. In fact, as we mentioned before, the thermal oxidation of high-aspect-ratio silicon trench arrays causes step height between the regions with different patterns and then traditional substrate bonding methods such as anodic bonding and fusion bonding would fail.

2.4 Fabrication Method II (Conformal Trench Filling)

The non-conformal trench sealing method with PECVD oxide deposition allows us to fabricate enclosed, robust nanochannels, but it has obvious limitation. In order to seal trenches completely and have negligible influence on channel geometries, this method using non-conformal trench filling described above is only applied to the situation where all of the structural dimensions (gap size, inter-pillar distance, etc) must be small, usually less than 2 μm. In many applications, however, nanochannels need to be connected with large-scale channels (gap size larger than 10 μm) to realize novel functions such as biomolecule preconcentration (*66-68*). A straightforward solution is to create large-scale channels after nanochannels are sealed with the first method. After sealing of nanochannels, the wafer surface becomes flat enough to perform subsequent photolithography and etching processes for creating large-size channels such as microchannels or reservoirs. In the case of electric fields required as driving forces in lots of applications, however, the exposed silicon surfaces of large-size channels need to be passivated either by regrowing thermal oxide or by depositing non-conductive material (e.g. nitride or oxide). These will change the gap size and even the shape of nanochannels, resulting in great challenges in control of nanochannels. Also, deposition process would block nanochannels.

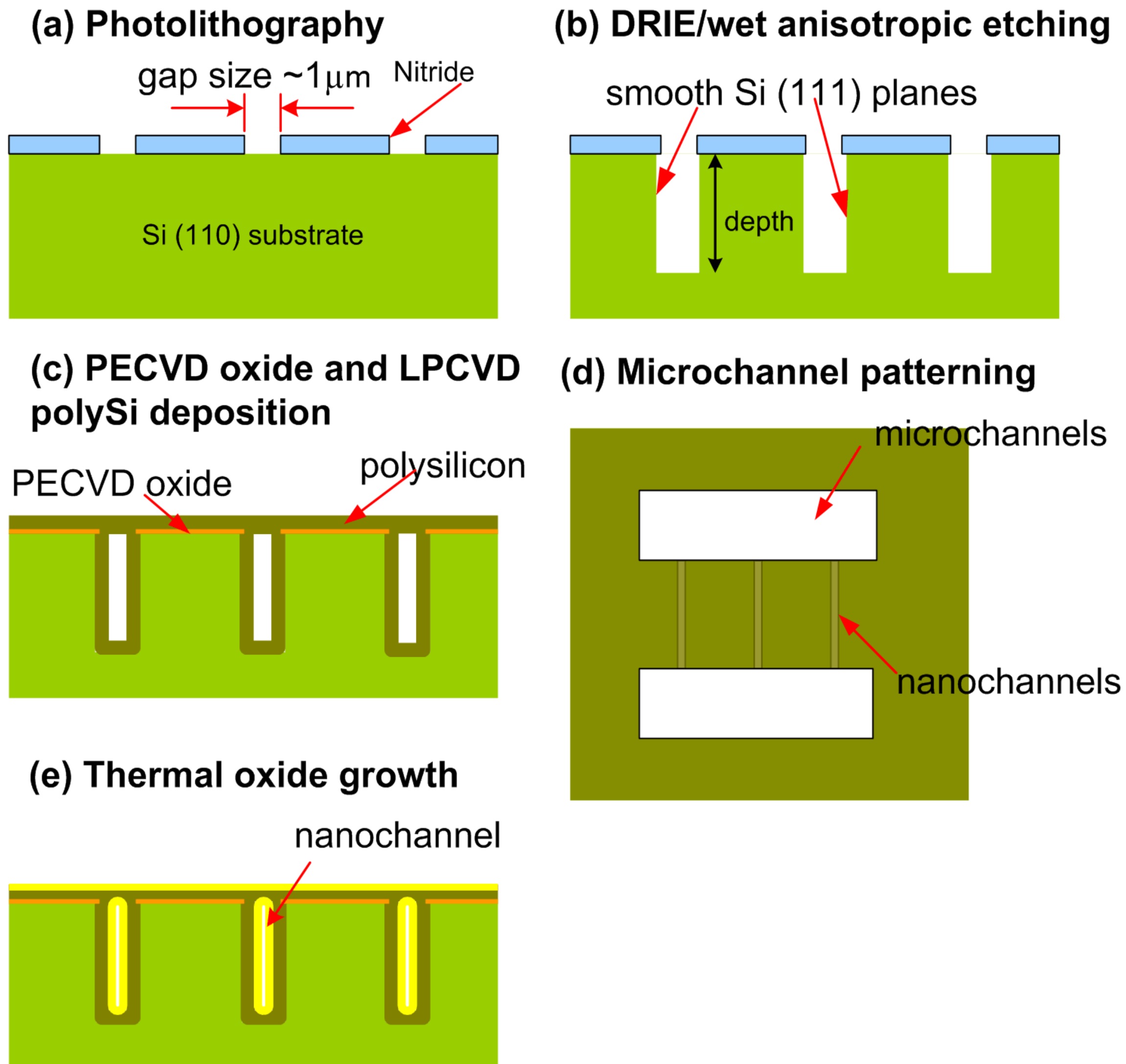

Figure 2.8 Schematic diagram of fabrication process using the method II of conformal trench filling. (**a**) patterning channels by standard photolithography; (**b**) etching deep trenches by either DRIE or anisotropic wet etching (KOH); (**c**) depositing non-conformal PECVD oxide and conformal LPCVD polysilicon to seal trenches sequentially; (**d**) patterning and etching large-sized channels (microchannels or reservoirs); (**e**) growing thermal oxide to decrease the gap size. (**a**), (**b**), (**c**), and (**e**) are the cross-sectional view while (**d**) is the top view.

A modified approach, called the conformal trench filling method, has been developed to overcome this limitation. Instead of performing trench sealing after thermal oxidation, the second method reverses these two steps, *i.e.* trench sealing before thermal oxidation. The fabrication process of the second method is shown in **Figure 2.8**. Narrow channels (~1 µm) are patterned by standard photolithography. After KOH etching of deep trenches, PECVD oxide and LPCVD (low pressure CVD) polysilicon are sequentially deposited on the trenches. Then, if needed, large-sized channels can be defined and created since the wafer surface is planarized after trench sealing. Finally, the thermal oxide is grown to narrow the gap size down to the desired value. This method allows easy connection between micro- and nano-channels and offers much flexibility in device design and fabrication.

2.5 Characterization of Fabrication Method II

2.5.1 Various Trench Sealing Methods

We have attempted many deposition methods to seal trenches and form embedded nanochannels. A straightforward way is to simply reverse the deposition and oxidation steps described in the first method. The channels as narrow as 1 µm can be completely sealed by 2 µm thick PECVD oxide, and very little influence on the channel geometry has been demonstrated above. However, significantly large-sized gaps are observed on the top of nanochannels, as shown in **Figure 2.9a**. It is due to the fact that the top surface of nanochannels is oxide and remains stationary during oxidation process, hence causing no shrinkage of gap size in that area and, as a result, large pores.

It turns out silicon material is required in all surfaces in order to reduce gap sizes uniformly. With this in mind, PECVD amorphous silicon (a-Si) deposition at 400 ^{o}C has been investigated. Trench sealing with a-Si of more than 1 μm in thickness shows the same profile as PECVD oxide, but unfortunately a-Si film is peeled off from the wafer during the step of thermal oxidation at 1000 ^{o}C. We believe that high stress in thick a-Si film causes cracks and even peeling-off of films during oxidation at high temperature.

LPCVD process is believed to be much more conformal than PECVD process and have the excellent capability of conformally depositing materials in trenches, since it takes place in much lower pressure and hence has much longer mean free path of molecules. We have examined the capability of two LPCVD processes (LTO oxide and polysilicon) in depositing materials in high-aspect-ratio channels. As shown in **Figure 2.9b**, non-uniform deposition of low temperature oxide (LTO) has been observed throughout the depth of the trench. Thicker film occurs near the top (entrance) of trench sidewall while thinner film is deposited near the bottom of trench sidewall. In contrast, in the case of trench sealing with LPCVD polysilicon, the film at the bottom sidewall is thicker than the one at the top (**Fig. 2.9c**). This different deposition behavior can be explained by the fact that polysilicon deposition occurs at 620 ^{o}C, much higher than 400 ^{o}C at which LTO oxide is deposited at similar pressure (~250 mTorr). Based on this observation, it is reasonable to assume that tuning the appropriate parameters of LPCVD process such as temperature and pressure could achieve better step coverage and uniform coating in high-aspect-ratio trenches. However, these parameters would vary for the trenches with different aspect ratios. In addition, deposited films would

possess different properties (e.g. polycrystalline or amorphous) under different conditions. Therefore, it turns out to be much challenging and problematic in achieving the task of conformal coating in high-aspect-ratio channels.

Recently, atomic layer deposition (ALD) has become an attractive technique for depositing thin films in semiconductor industry because it offers the advantages of pinhole-free, large area uniformity, and excellent conformality (*69*). ALD might have the capability of achieving deposition as uniform and conformal as thermal oxidation but could be more time-consuming and expensive, with a limited materials choice readily available. Besides, it will be very challenging to deposit thick films of more than 500 nm with ALD, which is typically required in this work to narrow down gap sizes. We do not have access of ALD to test it yet.

Interestingly, we have found out that with the combination of PECVD amorphous silicon and LPCVD polysilicon, we can achieve conformal, uniform deposition in the 27 μm deep trenches, as shown in **Figure 2.9c**. The original gap size of 1.2 μm is uniformly reduced to 365 nm. Since amorphous silicon tends to peel off at high temperature as described above, we replace the PECVD a-Si deposition with PECVD oxide deposition.

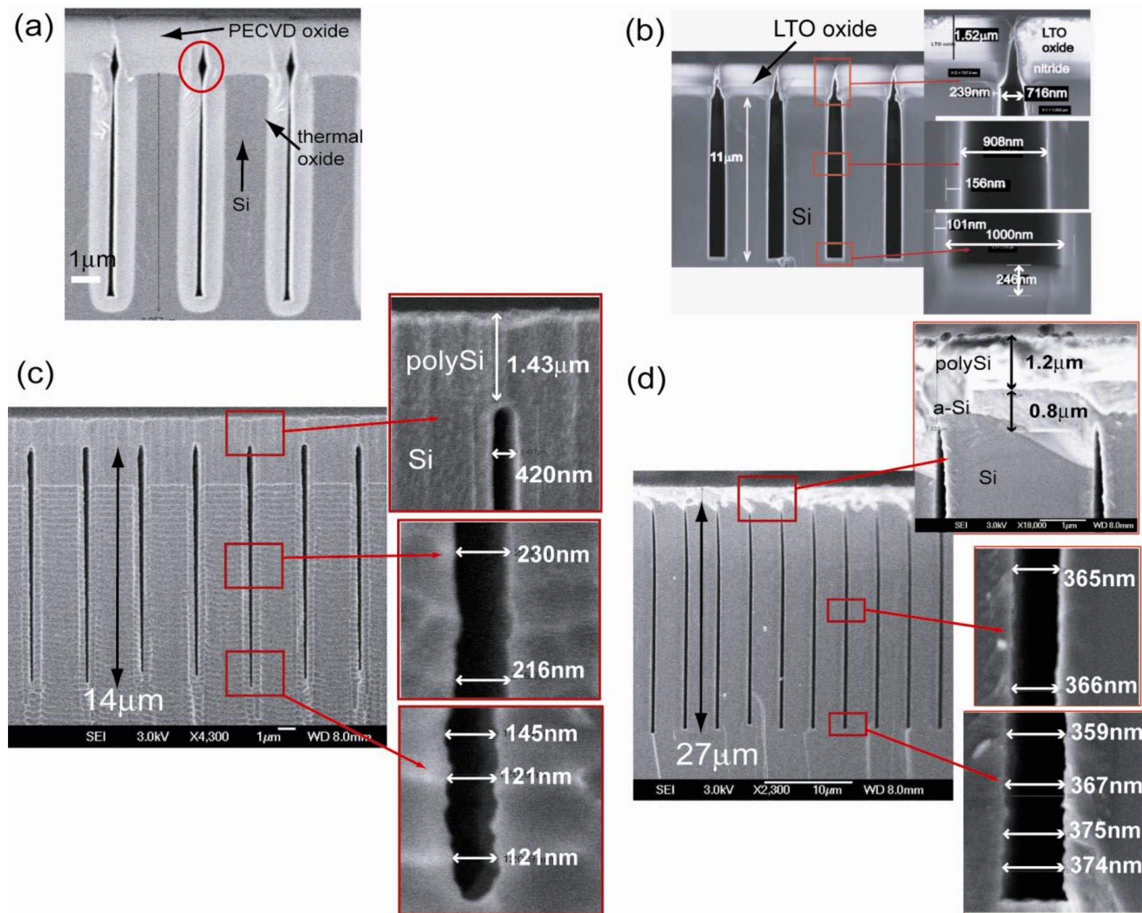

Figure 2.9 Cross-sectional SEM micrographs showing the behaviors of trench sealing by various deposition methods. (**a**) Trenches are first sealed by PECVD oxide deposition, followed by thermal oxidation. A large open pore, designated by the circle, is formed due to the oxide surface of top part of sealed channels. (**b**) Trenches are completely sealed by depositing 1.5 µm thick LTO oxide. The trench is 1.2 µm wide and 11 µm deep. Nonconformal deposition takes place along the trench sidewalls with thicker film near the entrance and thinner film in the bottom. (**c**) Trench sealing by LPCVD polysilicon deposition. Nonconformal deposition is observed in the sidewalls. The gap size, originally 1.1 µm, is reduced to 420 nm (top) and even to 121 nm (bottom). (**d**) Trench sealing by PECVD amorphous silicon of 0.8 µm and LPCVD polysilicon of 1.2 µm, sequentially. Very conformal deposition occurs along the trench of 27 µm in depth. The gap size is uniformly reduced from 1.2 µm down to 365 nm.

2.5.2 Combination of PECVD and LPCVD Processes

Figure 2.10 clearly shows that PECVD oxide deposition at 400 ^{o}C is a rather non-conformal process while successive LPCVD polysilicon deposition at 620 ^{o}C occurs uniformly on the sidewalls and seals the trenches completely. The combination of these non-conformal and conformal processes allows us to maintain a uniform gap size along the trench, except very near the trench entrance, after deposition. The trench opening can be engineered in such a way to help regulate subsequent LPCVD process to achieve conformal deposition. Our method provides an alternative way to realize conformal LPCVD deposition in high-aspect-ratio trenches by controlling the profile of trench openings with PECVD deposition.

Interestingly, their final gap size becomes almost the same although the trenches differ in width by 0.5 µm before deposition as shown by comparison of the case (**a**) and (**b**) in **Figure 2.10**. It turns out that the final gap size after deposition doesn't depend on the initial gap size, but is the difference between the initial gap size and the trench opening after the PECVD oxide deposition, which is determined by PECVD process. In fact, when the initial gap sizes of two channels differ slightly (less than 1 µm, for instance), their film profiles of oxide by PECVD deposition are very much identical, resulting in the same final gap sizes. Therefore, it is very straightforward to control the final gap size by tuning PECVD oxide deposition time as well as oxidation time. This is a very important result because it can cancel out the defects of large gap sizes due to the photolithography or etching process to some degree. Also, this strong capping layer can prevent structures from bending or distorting during thermal oxidation process, as

described above. We believe that this approach will allow the generation of robust high-aspect-ratio embedded nanochannels with precise control on structural parameters and much flexibility in device design, although further investigation on the limitation of this approach is needed.

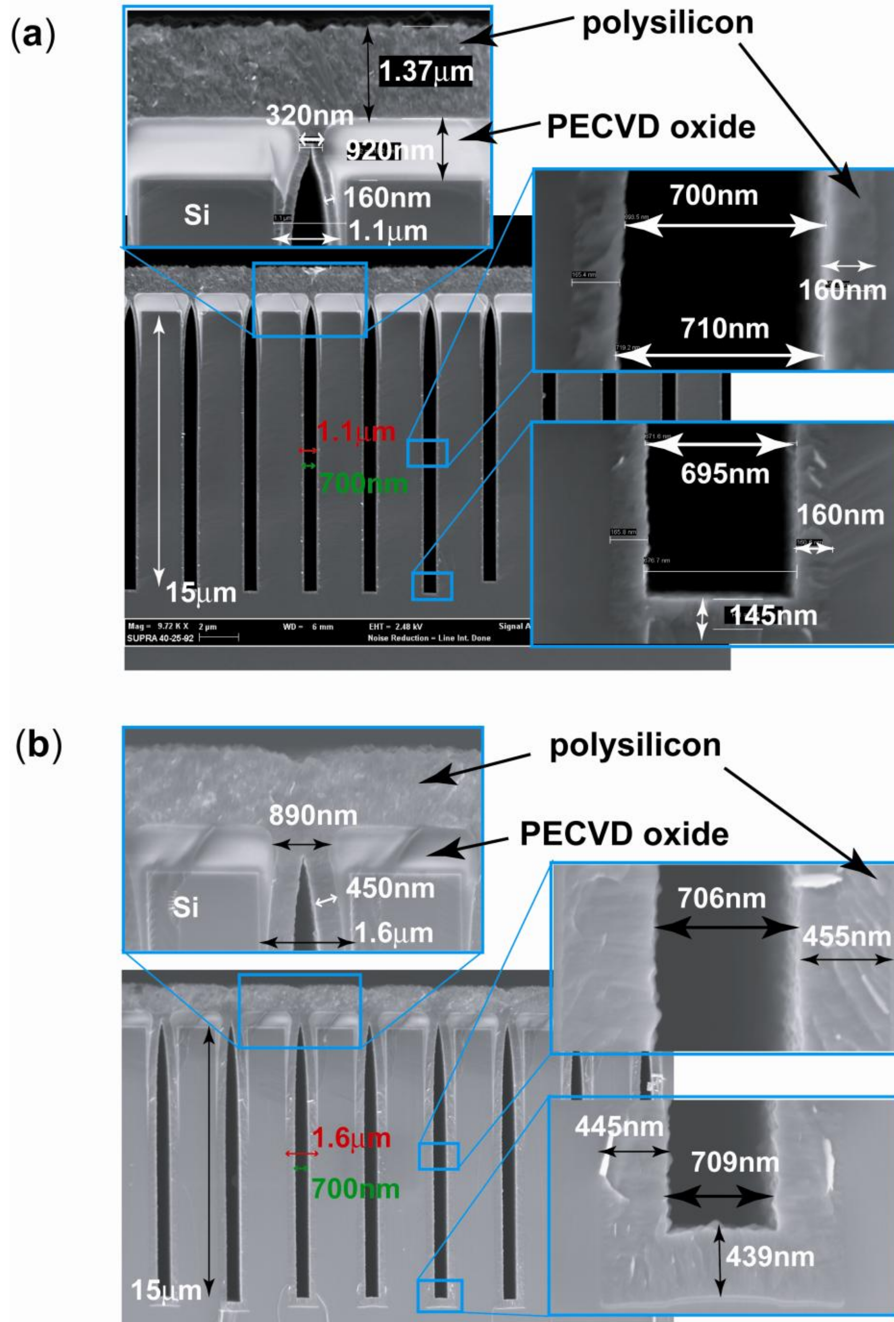

Figure 2.10 Cross-sectional SEM images of 15 μm deep trenches deposited with 900 nm thick PECVD oxide and 1.37 μm thick LPCVD polysilicon sequentially. The gap size uniformly changes from 1.1 μm to 700 nm (**a**) and from 1.6 μm to 700 nm (**b**) after deposition, respectively. It shows that their final gap after LPCVD polysilicon deposition becomes almost the same although their initial gap size differs by 0.5 μm.

2.5.3 Micro-Nanochannel Connection

As described above, the second method allows easy integration of micro-sized with nano-sized channels. For one example, using this conformal trench filling method, we have fabricated a nanofluidic preconcentration device, which consists of two parallel microchannels bridged by an embedded nanochannel array. The connection between the microchannels and nanochannels is clearly shown in **Figure 2.11**. The nanochannels and microchannels are formed by KOH etching and DRIE etching, respectively. This vertical preconcentration device allows much higher concentration volume, compared to the previous reported similar device with planar nanochannels (*66*).

2.6 Summary

In conclusion, this chapter describes two fabrication methods for creating massively-parallel, ultrahigh-aspect-ratio nanochannels by a combination of anisotropic etching and thermal oxidation. Nanochannels are sealed by CVD deposition, which eliminates the need for substrate bonding. Vertical nanochannels with a uniform gap size of 55 nm and aspect ratio as high as 400 have been demonstrated. Our fabrication processes are inexpensive, completely CMOS-compatible, without any nanolithography or non-conventional fabrication tools required. Gap sizes can be well controlled, and connection between microchannels and nanochannels can be created in a seamless way. These ultrahigh-aspect-ratio nanochannels have the merit of large open volume, enabling their use in high-throughput applications.

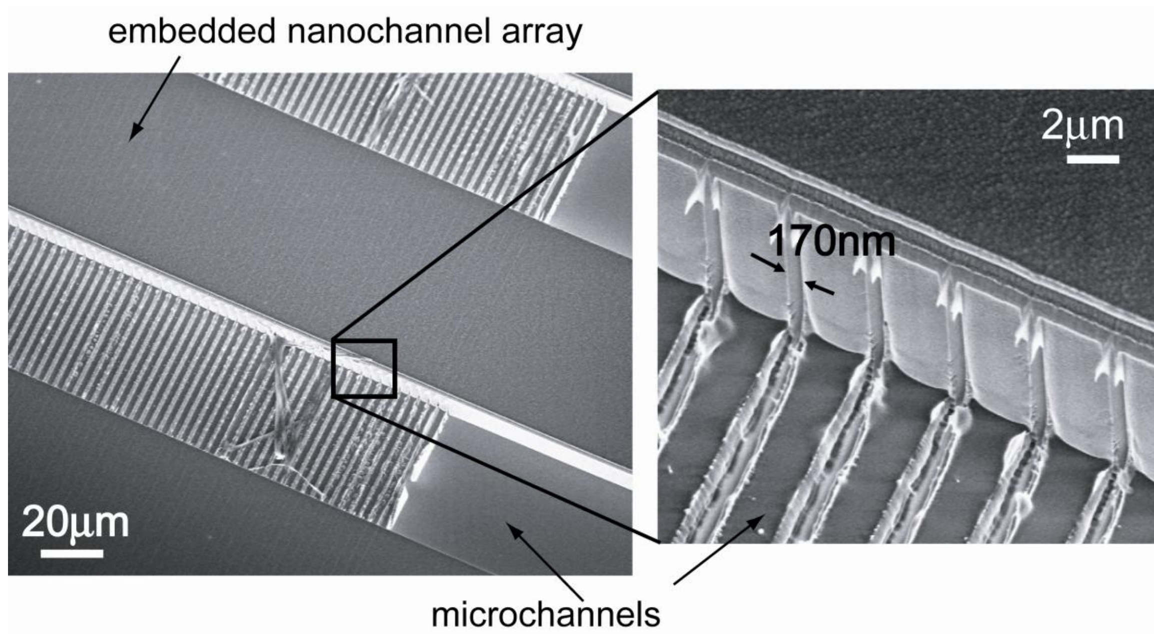

Figure 2.11 Tilted-view SEM images showing the interfaces between micro- and nano-channels. It consists of two parallel 50-μm-wide channels, bridged by an embedded nanochannel array. The gap size of a nanochannel is 170 nm. All the channels have the same depth of 12 μm. The microchannels and nanochannels are produced by DRIE and KOH etching, respectively. The trenches in the bottom surface of microchannels near the nanochannel array are due to the overetching of the nanochannel array pattern during DRIE etching of the microchannels.

Chapter 3

Vertical Nanofilter Array for Continuous-Flow Separation of DNA and Proteins

3.1 Introduction

The ability to identify and separate different molecules out of a complex mixture (DNA, proteins, e.g.) is crucial in biology and biomedical engineering. As an alternative to the conventional nanoporous structures (such as gel), the development of artificial nanofluidic sieving structures holds great promise to improve separation efficiency, optimize biomolecule separation methods and further integrate them in an on-chip format into complete microanalysis systems (*30*). One interesting example is to employ the standard microfabrication techniques to create planar nanochannels or nanofilters for molecular sieving. Han *et al.* designed an entropy-based separation system, in which the entropic trap array consists of alternating shallow channels and deep channels, and applied it to separate long DNA (*70*). Using the same fabrication method, Fu *et al.* developed a one-dimensional (1D) nanofilter array system that extended separation to physiologically-relevant macromolecules such as short DNA molecules and proteins (*59*). Recently, Fu *et al.* further devised a two-dimensional anisotropic nanofilter array (ANA) that continuously sorted DNA and proteins within a few minutes (*33*). The ANA represents a significant advance compared to the batch separation operation in 1D

nanofilter arrays, since the continuous-flow operation of the ANA permits continuous-harvesting of the subset of biomolecules of interest to enhance the specificity and sensitivity for downstream biosensing and detection. In addition, the continuous-flow operation greatly enhances sample throughput. However, due to the fact that these planar nanochannels exhibit extremely small open volume for sample processing, the sample throughput of these systems is still low, compared with traditional gel-based membrane systems such as 2D slab-gel, and needs to be further enhanced for practical applications of artificial sieving systems.

In the previous chapter, the fabrication of high-aspect-ratio nanochannels has been described and it has been shown that the large open volume of vertical nanochannels enables high throughput applications. Hence, it is rational to apply it for high-throughput biomolecule separation. In this chapter, we describe the design and fabrication of 2D vertical anisotropic nanofilter array (ANA) device and demonstrate its implementation for continuous-flow separation of large DNA and proteins. The designed structural anisotropy of the ANA causes biomolecules of different sizes or charges to follow distinct trajectories, leading to efficient continuous-flow separation. The sample throughput in vertical ANA device can be as high as ~µL/hour, which is much higher than ~nL/hour in planar ANA device. The separation mechanism in vertical ANA device is also discussed.

3.2 Molecular Sieving and Filtering Mechanism

Transport of biomolecules through a sieving or filtering structure is a complex process determined by many factors, including steric interaction, hydrodynamic interaction, electrostatic interaction, and conformational dynamics of molecules. Along with development of artificial sieving structures for bioseparation, significant efforts have been made towards understanding molecular sieving and filtration through nanofluidic systems. Many sieving mechanisms have been proposed and reviewed in the literature (*30, 31*). Here, in particular, we will give an overview of separation mechanisms taking place in nanofilter systems.

Ogston Sieving

In Ogston sieving, biomolecules of interest have diameters smaller than the size of the nanofilter constriction. At relatively high ionic strength buffer conditions, the *Debye* length (surface effect) becomes negligible compared to the nanofilter size. Therefore, molecules experience sieving effects mainly caused by steric interaction when they migrate through a nanofilter region. Due to steric repulsion from channel walls, the configurational freedom of molecules inside the nanofilter region is limited, which is well described by hindered transport or partitioning theory (*71*). This results in a size-dependent configurational entropic energy barrier for molecules to transport from the open space or large-sized region (*e.g.*, microchannels) to the confined nanofilter region. The Ogston sieving process has been suggested as an electric-field-driven (equilibrium-like) partitioning process between the nanofilters/pores and open space (*72*).

Specifically, the electrophoretic mobility of a molecule in a nanopore/filter system relative to its mobility in a free solution is equal to the fractional free volume available to the molecule, *e.g.*, partition coefficient. Smaller-sized biomolecules are favored to jump across the nanofilter constrictions due to their greater retained configurational freedom or higher accessible free volume. Therefore, smaller-sized biomolecules jump across the nanofilter constriction with higher probability than larger ones, leading to faster migration speed or higher mobility through the nanofilter array.

Entropic Trapping

Entropic trapping applies when the radius of gyration of flexible biopolymer (such as long DNA) is larger than (or comparable to) the nanofilter size. Obviously, rigid particles with diameter larger than the nanofilter will be clogged in front of it (hard, mechanical filtration), but flexible or semi-flexible molecules can be deformed or stretched to enter nanofilters. This requires additional energy to deform and stretch the molecule to fit into the nanofilter. In the case of long DNA molecules, the energy barrier to overcome comes from their internal entropic free energy landscape, which favors unstretched, spherical conformation over extended conformation. Han *et al.* observed that long DNA molecules are favored to enter the nanofilter structure over shorter DNA molecules. It is believed that DNA molecules form hernias and only a small portion of DNA molecules is required unraveled in order to initiate the escaping process (*73*). In addition, longer molecules have a larger surface area contacting the constriction and thus have a higher probability of forming the hernias than smaller ones. As a result,

longer ones have a higher jump rate across the nanofilter constriction in entropic trapping.

Reptation

When the radius of gyration of molecules becomes much larger than the nanofilter size, the migration of molecules into sieving structures is explained by the reptation theory. Reptation can be envisioned as a long linear flexible macromolecule occupying multiple pores threading its way through the gel in a snake-like fashion. DNA molecules tend to get stretched out and be lined up along the direction of the applied field, which would make size-based separation difficult. By using the operation of pulsed fields, stretched DNA molecules are driven into two different directions, and can relax themselves and adopt highly collapsed configurations upon switching the direction of electric fields(*74*). In general, shorter molecules have a higher jump rate than longer ones.

Electrostatic Sieving

For low ionic strength solutions, the *Debye* length of the nanofilter / nanopore becomes comparable to the nanofilter constriction size, and electrostatic interactions (either repulsive or attractive) between charged biomolecules and charged nanofilter walls become prominent and start to affect jump dynamics across the nanofilter. Co-ions or molecules with the same charge polarity as the surface charge of nanofilters will be hindered from entering the nanofilters, compared with the counter-ions or molecules with the opposite polarity. Therefore, similar sized biomolecules bearing different

polarity or net charges are energetically favored to different extents for passage through the nanofilter, resulting in efficient separation across the nanofilters (*30, 33*). In addition, electrostatic repulsion between negatively charged biomolecules and like-charged nanofilter walls can result in an effective decrease in the nanofilter constriction size and hence further enhance size-based separation.

3.3 Device Design and Fabrication

Following the pioneering work of planar ANA device developed by Fu *et al.* (*33*), the design of the vertical ANA consists of a two-dimensional (2D) period nanofilter array, as shown in **Figure 3.1**. The anisotropic pillar array of 5 mm x 5mm contains horizontal narrow channels in the *x*–direction and longitudinal wide channels in the *y*–direction. The pitch size of pillars is 3.5 µm in the *x*-direction and 4 µm in the *y*-direction, respectively. The supplemental microfluidic channels are designed to connect sieving matrix and fluid reservoirs, where voltages are applied. Furthermore , the microfluidic channels direct fractionated sample stream to reservoirs for collection, and also act as electric-current injectors to create uniform electric fields of E_x and E_y over the entire ANA structure (*75*). The initial sample stream is continuously injected from sample injection channels, which is 1 mm away from the bottom corner of ANA, into the wide channels of ANA. Sample injection a little away from the corner is beneficial since the field distribution in the corner is usually non-uniform.

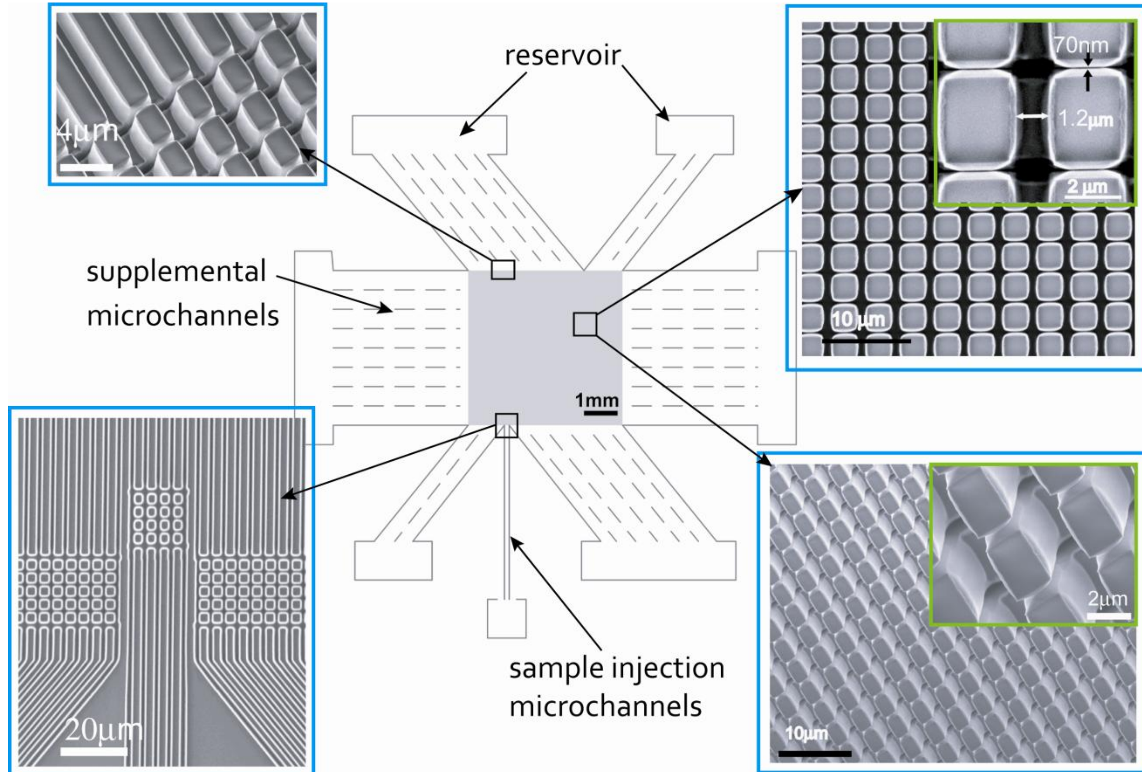

Figure 3.1 Schematics of a two-dimensional, vertical, anisotropic nanofilter array device. Scanning electron microscopy (top- and tilted-view) images show the details of different device regions including sample injection channels, supplemental microchannels, and ANA. The sieving matrix, 5 mm by 5 mm, consists of periodic horizontal nanochannels with a width of 70 nm and longitudinal microchannels with a width of 1.2 μm. The pitch size of pillars is 3.5 μm in the *x*-direction and 4 μm in the *y*-direction, respectively. The supplemental microchannels of 1.5 μm in width are used to connect the sieving matrix and reservoirs. Sample is injected from the sample injection microchannels which include five 1.5 μm-wide individual channels. All of the channels are 15 μm in depth.

(a) KOH etching to produce the narrow ANA channels

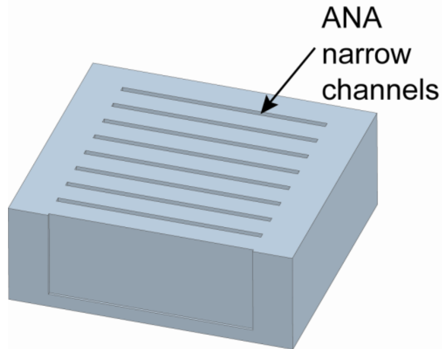

(b) DRIE etching to produce the wide ANA channels

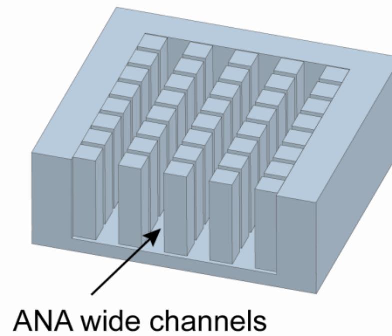

(c) thermal oxidation to narrow down gap size

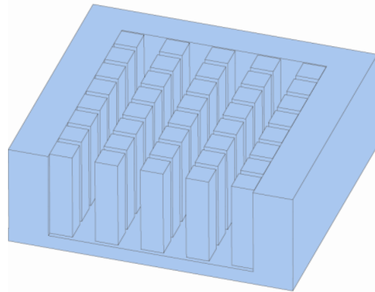

(d) PECVD oxide deposition to seal ANA devices

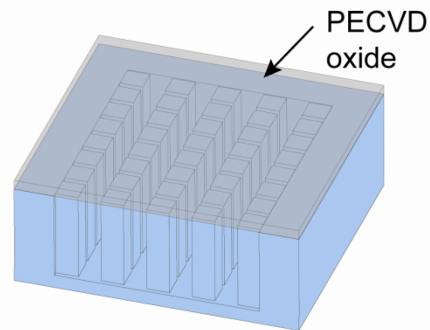

(e) Buffer access holes

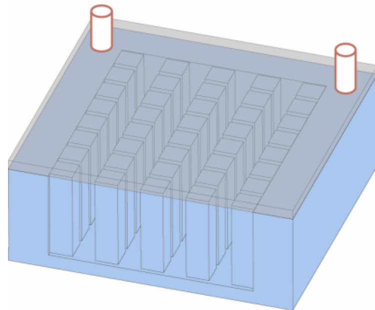

Figure 3.2 Schematic of the fabrication process for the vertical ANA device. (a) the narrow channels of ANA device are created using KOH etching; (b) the wide channels of ANA device are created using and DRIE etching; (c) thermal oxide layer is grown to narrow down the gap size as well as to provide an electrical isolation between the conductive silicon substrate and buffer solution; (d) PECVD oxide is deposited to seal the ANA device; (e) buffer access holes are generated by RIE etching of PECVD oxide layer.

The vertical ANA devices are batch fabricated using conventional semiconductor microfabrication techniques on a (110) silicon wafer in a cleanroom environment. First, high-aspect-ratio vertical nanochannels (narrow channels) are produced using KOH etching (**Fig. 3.2a**) by the first fabrication method as described in the chapter 2. Then, wide channels are patterned and etched by standard photolithography and DRIE technique (**Fig. 3.2b**). In this step, the channel depth is controlled to match the one of narrow channels. Thermal oxidation is followed to narrow down the gap size of narrow channels to the desired value (~ 50 nm) (**Fig. 3.2c**). In addition, the entire surface is passivated with thermal oxide to provide isolation between silicon substrate and buffer solution. After that, all the channels including nanochannels and microchannels are sealed by PECVD oxide deposition to form enclosed channels (**Fig. 3.2d**). Finally, buffer access holes are patterned and generated by standard photolithography and RIE etching of oxide layer. Much care must be taken to make sure that the holes are etched deep enough to be open to the sealed channels but the oxide layer should not be etched through, which will cause exposure silicon surface. The detailed fabrication procedures of the vertical ANA device are listed in Appendix I. Buffer or sample reservoirs are provided by bonding another PDMS layer with well-positioned holes to the silicon device or by making a custom-machined plastic gadget. The gadget with holes can be screwed to the ANA device with a silicone rubber gasket.

We have also characterized the DRIE process for generating high-aspect-ratio trenches since it has to be used in creating wide channels here. By tuning the DRIE parameters, we have been able to obtain 35 μm deep channels with an undercut less

than 1 μm and sidewall angle less than 1° deviation from the vertical direction, as shown in **Figure 3.3**. The scallops are less than 20 nm in the entrance region and become negligible in the other regions a few micrometer away from the channel entrance. In addition, SEM shows rather smooth sidewalls when looking from the side.

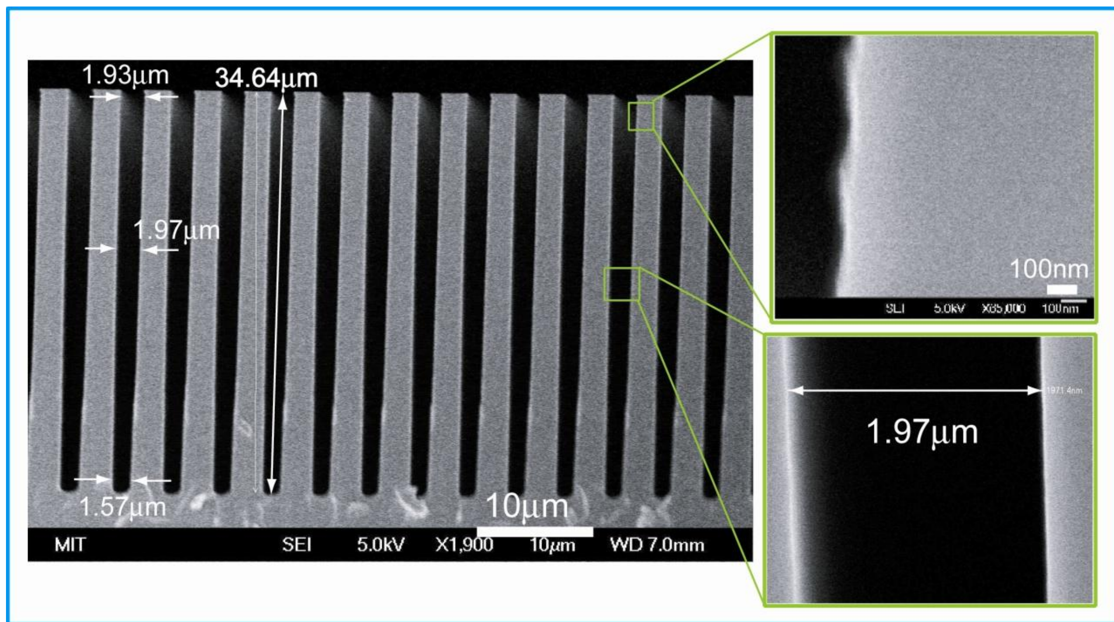

Figure 3.3 Cross-sectional SEM images of 35 μm deep trenches etched by DRIE. The initial width is 1 μm and the sidewall angle is 89.3°. The close-up shows the sidewalls with small scallops (less than 20nm at the top and negligible in the other regions).

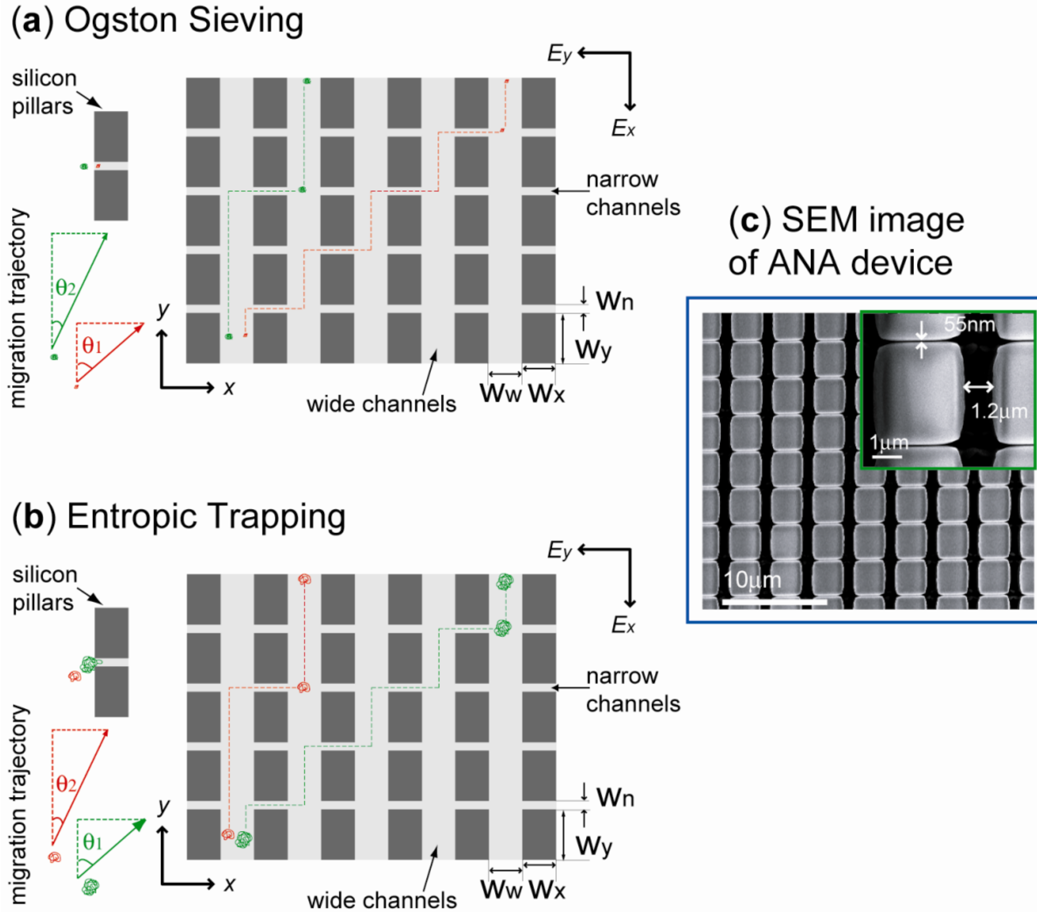

Figure 3.4 Schematic showing bidirectional motion of negatively charged macromolecules in a vertical ANA device in two orthogonal electric fields of E_x and E_y. Dashed lines and arrows indicate migration trajectories projected onto the *x*-*y* plane. Narrow channels with gap size (width) of W_n and Wide channels with gap size of W_w are spaced by W_y and W_x, respectively. All the channels have the same depth. (**a**) Ogston sieving. The sizes of molecules are smaller than W_n. Shorter molecules (*red*) have a higher nanofilter jump passage rate than longer ones (*green*). Hence shorter molecules have a larger stream deflection angle θ that is defined with respect to the *y*-axis. (**b**) Entropic trapping. The sizes of molecules are greater than W_n. Longer molecules (*green*) have a higher probability to form hernia and thus a greater nanofilter passage rate than shorter ones (*red*). As a result, longer ones have a larger stream deflection angle θ. (**c**) Top-view SEM image of ANA device.

Two sieving regimes, Ogston sieving and entropic trapping, are explored in vertical ANA devices, where the relevant nanoscale constriction is the horizontal narrow channel with gap size of W_n in contrast with the depth of shallow channels in planar ANA. Both regimes deal with relatively high ionic strength solutions where the surface effects can be neglected. Two orthogonal electric fields of E_x and E_y are applied in the ANA device to drive molecules as shown in **Figure 3.4**. Biomolecules won't experience any sieving effect in wide channels (*y*-direction) upon E_y, but with E_x superimposed in *x*-direction they are driven to jump across narrow channels (nanofilter). Due to the sieving effects, biomolecules experience different passage rates across the narrow channels, resulting in their traveling different distances in the *y*-direction between two consecutive nanofilter crossings. The mean drift distance between two consecutive nanofilter crossings determines the migration trajectory and hence the stream deflection angle ϑ of the biomolecules, which is defined with respect to the positive *y*-direction. As summarized in the previous section, in Ogston sieving, where the sizes of biomolecules are smaller than the gap size W_n of narrow channels, smaller ones are preferred for passage through the nanofilter due to their greater retained configuration freedom than larger ones, leading to a higher nanofilter jump passage rate. Therefore shorter molecules have a larger stream deflection angle ϑ than larger ones (**Fig. 3.4a**). In contrast, in entropic trapping regime where the sizes of biomolecules are greater than W_n, longer ones have more surface area in contact with the constriction and thus have a higher probability of forming the hernias to initiate the escape process. As a result, longer ones have a higher jump rate across the nanofilter and then a larger stream

deflection angle ϑ than smaller ones (**Fig. 3.4b**). The designed structural anisotropy of the ANA is the key to cause different sized- or differently-charged biomolecules to follow their distinct trajectories.

3.4 Experimental Setup and Sample Preparation

The vertical ANA device is mounted on an upright epifluorescence microscope (IX-71, Olympus, Melville, NY). The fluorescence microscope is equipped with a high resolution CCD camera (C4742-80-12AG, Hamamatsu, Japan) for fluorescence imaging. A 100W mercury lamp (Chiu Technical Corp., Kings Park, NY) is used for illumination. The images are further analyzed with image processing software of Image-Pro (Media Cybernetics, Bethesda, MD). The device was wetted first with PLL-g-PEG (o.1 mg/mL) solution for a few hours to coat the surface and prevent non-specific binding of biomolecules. In addition, this coating significantly reduces electroosmotic flow. Then Tris-Borate-EDTA (TBE) 0.5× buffer was introduced to replace PLL-g-PEG solution by applying electric fields. The device can be kept in TBE 0.5× at room temperature for a few months. Right before the separation experiment, TBE 0.5× was replaced with buffer TBE 5× or 10×. After the experiment, the solution will be changed back to TBE 0.5× for storage. During experiments, platinum wires were dipped into the fluid reservoirs to connect buffer solution with external power supply.

The Hind III digest of lambda DNA, obtained from New England Biolabs Inc., contains six fragments from 2,027 bp to 23,130 bp. The DNA molecules were custom labeled with intercalating fluorescence dye YOYO-1 (Invitrogen Inc., CA) to be visualized.

The dye to basepair ratio was about 1:4 and the final concentration in TBE 5× was about 20 μg/mL. Dithiothreitol (DTT) was also added with a concentration of 10 mM to minimize photobleaching of molecules. The native proteins of R-Phycoerythrin (R-PE) and Alexa Fluor 488 conjugated bovine serum albumin (BSA) as well as fluorescein isothiocyanate (FITC) were obtained from Invitrogen Inc. When diluted in TBE 5× or 10×, the final concentrations of R-PE, BSA, and FITC were about 0.2 mg/mL, 0.2 mg/mL, and 0.1 mg/mL, respectively. DTT was also added to prevent photobleaching. The sample can be stored in 4^oC for about a month.

3.5 Continuous-Flow Separation of Long DNA

To examine the sieving effects in vertical ANA device, we first tried with long DNA molecules (λ-DNA Hind III digest) since they have been well studied and have well-recognized structures. To minimize sieving effects due to surface charge, high ionic strength buffer TBE 5× is used, which leads to a *Debye* length of about 0.84 nm (*33*), negligible compared to the gap size of narrow channels (W_n=70 nm). As shown in **Figure 3.5**, the λ-DNA Hind III digest was continuously separated into four distinct streams in a few minutes with the decent electric fields applied in two orthogonal directions. The shortest two fragments (2,322 bp and 2,027 bp) were missing, which is most likely due to their low concentration and weak signal. Further observation with high magnification lens reveals that, as expected, longer molecules have a larger deflection angle than shorter ones. It suggests that longer ones have a higher jump passage rate through a nanofilter. This observation can be explained by the entropic trapping mechanism,

consistent with the results of separating long DNA in planar ANA device (*33, 73*). In fact, the radii of gyration of these DNA fragments range from ~140 nm to 520 nm, which are all greater than the nanofilter gap size of 70 nm. Therefore, DNA crossing of the nanofilter requires deformation of molecules and hernia formation at the cost of internal conformational entropy.

To compare with the planar ANA device, we characterize the separation resolution, defined as $R_s = \Delta X/(2\sigma_1 + 2\sigma_2)$ where ΔX is the distance between two adjacent peak locations (peak separation), and σ_1 and σ_2 are the respective standard deviations of two Gaussian zones (*76*). The separation resolution R_s (size selectivity) achieved in the vertical ANA device between two adjacent peaks is around 1.5, not as good as the resolution value of more than 2 in the planar ANA device. In addition, we observed much larger sample dispersion (stream broadening) in vertical ANA devices than in planar devices. It has been demonstrated both theoretically and experimentally in entropic trapping array devices that the size selectivity is inversely proportional to both the nanofilter period (pitch size) and the nanofilter gap size (*33, 77, 78*). The gap size (W_n) of the vertical nanofilter is 70 nm, which is larger than 55 nm of the planar nanofilter size. Also, the period of the vertical nanofilter array is 4 µm ($W_w + W_x$), which is twice as much as the planar nanofilter period of 2 µm. Therefore the total number of nanofilters in vertical ANA devices is only half of that in planar ANA devices, thus leading to a lower separation resolution, since the dimensions of their sieving matrix are the same. In fact, the number of vertical nanofilters used for DNA separation in this

experiment was 250 (*i.e.*, 1000/4), which is much less than the number of planar nanofilters of 1000 employed in planar devices to achieve high resolution.

In addition, the ratio of the gap size between wide channels (W_w) and narrow channels (W_n) plays an important role in separation resolution. This ratio corresponds to the ratio of the depths between deep region and shallow region in planar ANA devices (*77*). In this device, the ratio ($\gamma = W_w/W_n$) is about 20 (1.5/0.07), much larger than 6 (300/55) in the planar ANA device (*33*). It has been shown that increasing γ will result in an increase in t_{travel} , which is the time for a DNA molecule to travel one nanofilter period, thus decreasing separation resolution (*77, 79*). In addition, we have found that the significantly large ratio γ tends to cause the serious non-uniformity of the electric fields over the ANA device due to the electrical resistance mismatch of channels in two directions. That is why the stream curvature of the DNA molecules near the injection point was observed (**Fig. 3.5**). Hence it is important to choose a moderate ratio of gap size to maintain approximately uniform electrical fields as well as to sustain effective entropic trapping. The angle (slope) of slanted channel walls is another factor that affects the energy barrier for trapping (*80*). Further observation reveals that our device has similar rounded shapes of nanofilters as planar ANA devices and thus little effect on separation resolution should be expected. We believe that these issues can be solved accordingly and easily by optimizing the device design, and the separation resolution can be improved further, at least to be comparable to the resolution accomplished in planar ANA devices.

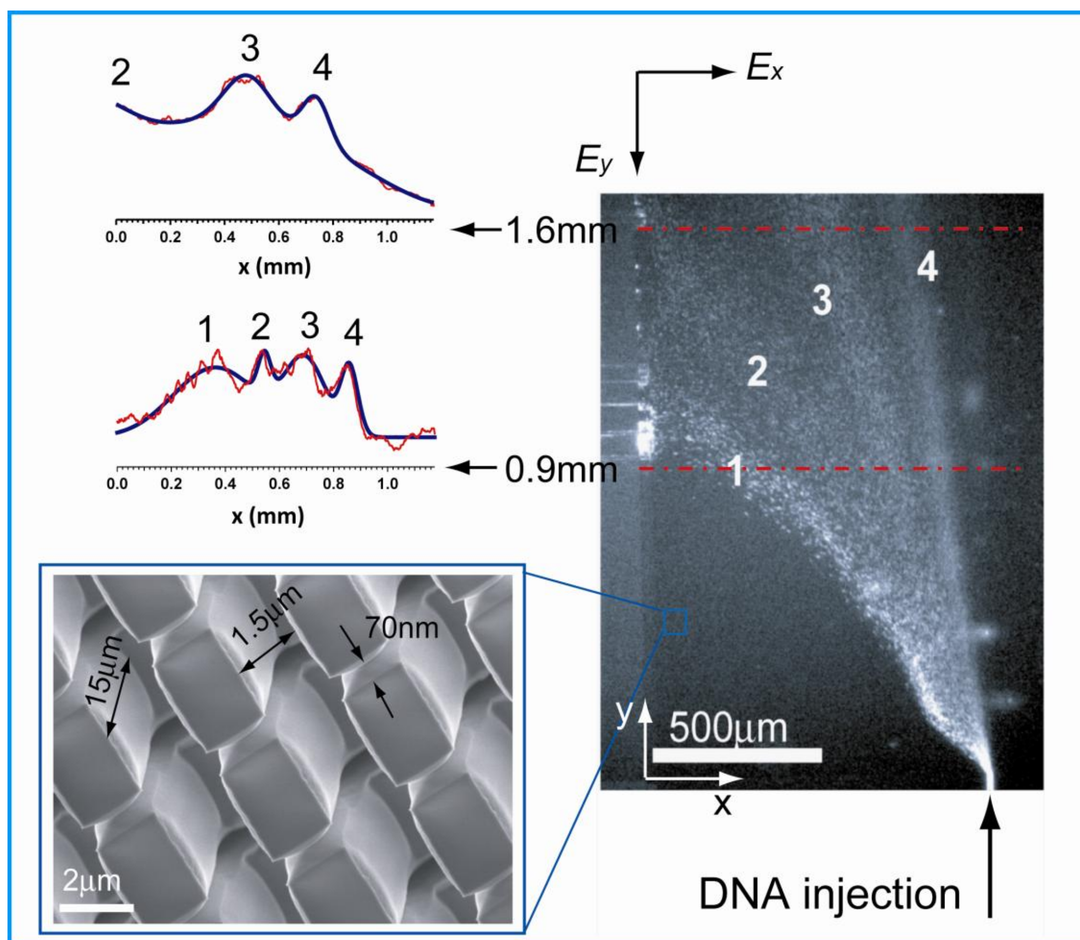

Figure 3.5 Fluorescence micrograph and intensity profiles along the red dash lines showing continuous-flow fractionation of the λ-DNA Hind III digest through the vertical ANA device. The titled-view SEM image shows the device dimensions (W_n=70 nm, W_w=1.5 μm, W_x=2.5 μm, W_y=3.5 μm, and depth of 15 μm). The electric fields of E_x and E_y applied both in the *x*- and *y*- directions in ANA are 80 V cm^{-1} and 30 V cm^{-1}, respectively. Band assignments are: (1) 23.13 kbp; (2) 9.4 kbp; (3) 6.58 kbp; (4) 4.36 kbp. Long DNA molecules have a larger deflection angle than shorter ones, consistent with entropic trapping. The resolution values $R_{s,12}$, $R_{s,23}$, $R_{s,34}$ between two adjacent peaks at 0.9 mm from the injection point are 0.71, 1.07 and 1.08, respectively. At y=1.6 mm, the resolution values $R_{s,23}$ and $R_{s,34}$ are 1.73 and 1.39. The Gaussian fitting (blue lines) is performed to determine separation peaks and peak parameters.

3.6 Continuous-Flow Separation of Native Proteins

The planar ANA device has demonstrated the capability of separating the mixture of proteins based on their size (molecular weight, MW) (*33*). As proof of concept, we first prepared the mixture of R-phycoerythrin (R-PE) and fluorescein isothiocyanate (FITC) in TBE 10×. The ANA device with a smaller gap size of ~ 40 nm was used. As shown in **Figure 3.6**, R-PE (MW~240 kDa) and FITC (MW~389 Da) were clearly separated into two streams in about 5 minutes. Non-specific adsorption in the device was negligible after PLL-g-PEG coating. The fluorescence micrograph is composite and obtained by combining two fluorescence micrographs taken in the same run and the same area but with two different filter sets (R-PE with a Texas Red filter set and FITC with a FITC filter set). The stream deflection angles of R-PE and FITC are about 4.0^{o} and 7.4^{o}, respectively, and the resolution value R_s is 1.30. Hence, as expected, the stream of FITC has a higher deflection angle than R-PE stream, suggesting that smaller molecules have a greater jump passage rate than larger ones. This result agrees well with Ogston sieving. Based on our observations, we believe that the molecular sieving behaviors in vertical ANA devices would be quite similar to the relevant phenomena taking place in planar ANA devices, although more experiments on complex sample, characterization of structural parameters, and field dependence need to be done in the future.

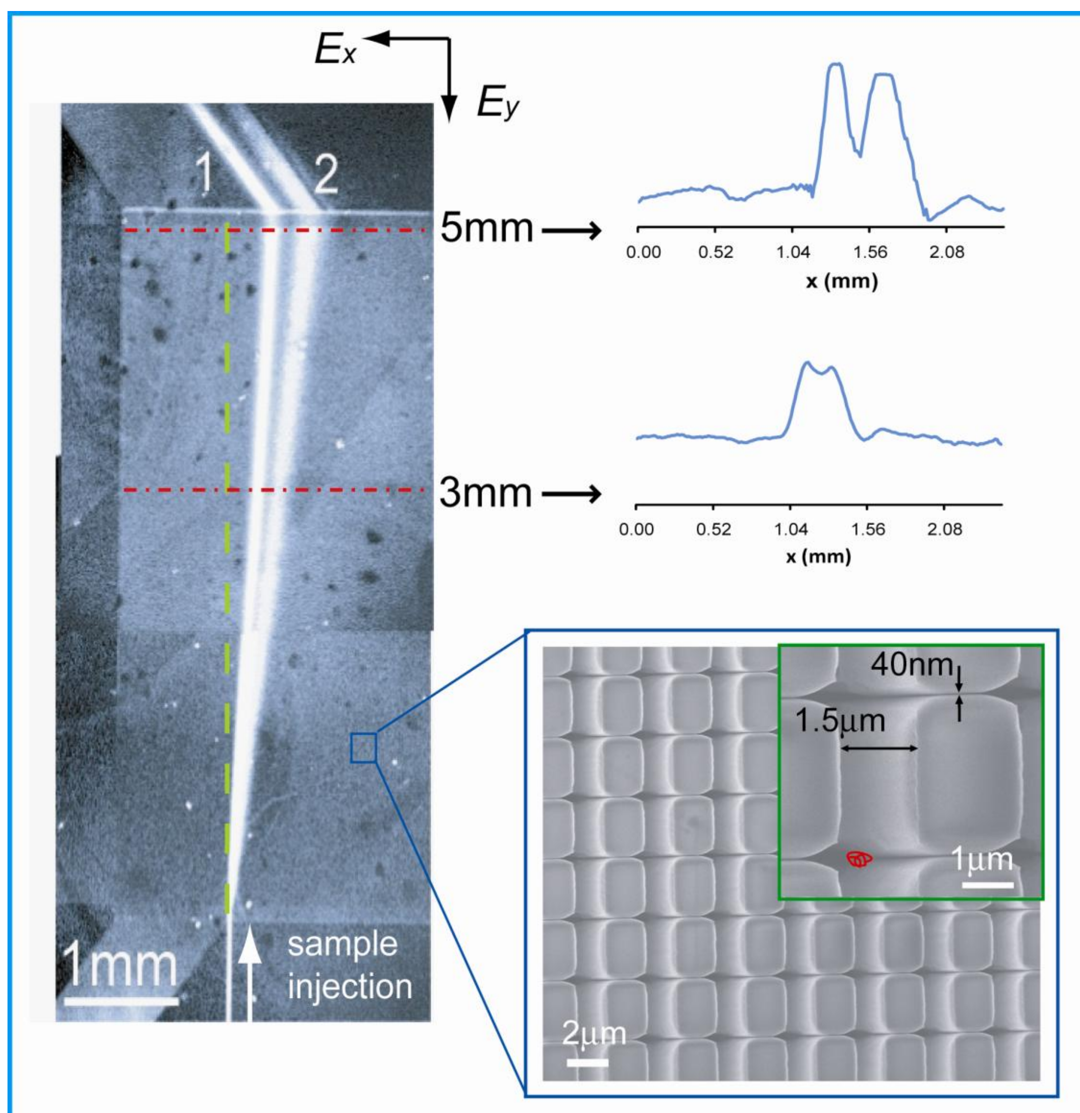

Figure 3.6 Fluorescence micrograph and intensity profiles along the red dash lines showing continuous-flow separation of FITC (band 2, MW~389 Da) and R-PE (band 1, MW~240 kDa) through the vertical ANA device. The composite image is obtained by combining two fluorescence micrographs taken in the same run but with two different filter sets (R-PE with a Texas Red filter set and FITC with a FITC filter set). The titled-view SEM shows its device dimensions (W_n=40 nm, W_w=1.5 µm, W_x=2.5 µm, W_y=3.5 µm, and depth of 15 µm). E_x=250 V cm^{-1} and E_y=40 V cm^{-1}. FITC has a larger deflection angle than R-PE stream, consistent with Ogston sieving. The resolution values R_s at 3 mm and 5 mm from the injection point are 0.41 and 1.30, respectively.

3.7 Sample Throughput of Vertical ANA Devices

The important feature of our vertical ANA devices is high sample processing rate (sample throughput) of ~ 1 μL $hour^{-1}$, and further improvement of sample throughput can be achieved simply by upscaling the channel depths. This throughput is much higher than that in planar ANA devices, which is about nL/hour (*33*). Our device is the first one that has achieved such high sample throughput using the nanofilter array. Also, the throughput of our ANA device is comparable to some continuous-flow microfluidic devices (*30, 81*). As an example, a DNA prism was reported to achieve separation of long DNA with comparable throughput, but it remains challenging or even unfeasible for protein separation because its critical dimension (inter-obstacle/pillar distance) is a few micrometer (*74*). For traditional gel-based separation technologies (such as 2D slab gel electrophoresis), typically ~10 μL samples can be processed in a batch mode (one elution separation after another), with each elution requiring 30~60 minutes typically. It looks like that the achieved throughput of our device would still be somewhat less than that of the current gel techniques. However, we would like to point out that such throughput in gel is achieved simply because the gels are ~10 mm in thickness and ~10 cm in size, while our device is much smaller. Parallelization of our device on a wafer scale would definitely bring about higher throughput, if such high-throughput is deemed necessary.

3.8 Summary

In summary, we have successfully implemented high-aspect-ratio nanochannels as sieving structures to achieve continuous-flow separation of biomolecules. The sample throughput achieved in the vertical ANA device is a few orders of magnitude higher than that in planar ANA device which utilizes planar nanochannels as sieving structures. It is important to recognize that sample throughout in nanofluidic systems should be enhanced for opening up wider applications as well as new opportunities in using artificial sieving systems. More efforts need to be made in optimizing this ANA device for its separation efficiency and extending its utilization for separation of complex native proteins as well as other important biomolecules such as carbohydrates. We believe that this vertical ANA device could be a key to the efficient proteomic sample-preparation microsystems as well as purifying and separating various bioparticles and nanoparticles.

Chapter 4

Layer-by-Layer Assembly of Polyelectrolytes in High-Aspect-Ratio Nanochannels

4.1 Introduction

Layer-by-layer (LbL) assembly of polyelectrolytes provides a versatile means to fabricate functional multilayer films and engineer surface properties of various substrates (*82*). The LbL assembly technique involves the sequential adsorption of two polymer materials that interact with each other through intermolecular interactions including electrostatic attraction and hydrogen bonding. The concept of LbL assembly is shown in **Figure 4.1**. The substrate is alternately exposed to the solutions of polycations and polyanions. Each deposition step leads to the spontaneous adsorption of polymers and the charge reversal of the multilayer surface, enabling the next layer of materials to be deposited by electrostatic interactions. The process can be repeated many times to achieve growth of polyelectrolyte multilayers (PEM). While deposition is usually achieved by the dipping method (simply dipping a substrate into each solution), the other methods including spin coating and spraying methods also are available (*83*). This LbL assembly technique is simple, easy, highly reproducible, and the thickness of film is precisely controlled. The film properties (thickness, hydrophobicity, charge polarity and density, etc) can be well tuned by varying the assembly conditions such as polymer

materials, salt ionic strength, concentration, pH, adsorption time, and temperature. In addition, this technique allows deposition of a wide range of functional polymers on surfaces of almost any kind and any shape, thereby widening further the applicability.

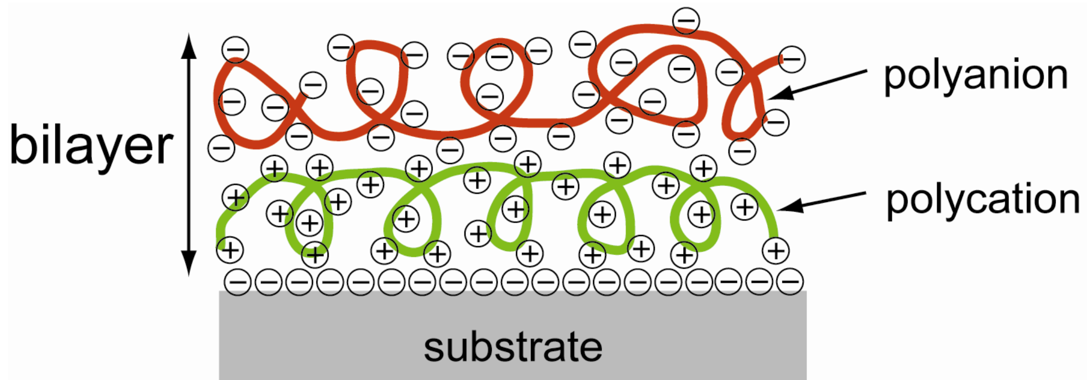

Figure 4.1 Schematic showing the concept of layer-by-layer assembly of polyelectrolytes. A bilayer represents a pair of oppositely charged polyelectrolytes. The polyion conformation and layer interpenetration are an idealization of the surface charge reversal with each adsorption step which is the basis of the electrostatically driven multilayer buildup depicted here.

LbL assembly of polyelectrolytes is interesting to nanofluidic membrane engineering due to the following two reasons: 1) It is a highly-controlled (down to a monolayer) film growth technique, which can be an alternative to the thermal oxide growth used in Chapter 2 and 3 to 'narrow down' the nanochannel membrane gap. Potentially, this method could be used to obtain truly nanometer-scale pores (~10 nm or less). 2) It is an effective method for modifying surface chemistry of the nanochannels.

It is well-known that surface interactions play an important role in governing transport and reaction in nanofluidic systems. The ability to tailor surface interactions in micro/nanofluidic systems will add uniqueness and open up new opportunities for a wide range of applications, in particular, biological applications. Because of its great advantages described above, LbL assembly has demonstrated great successes in tailoring and engineering surface properties (*82, 84, 85*). For example, Savariar *et al.* functionalized nanoporous membranes with polymers and used them to separate molecules based on size, charge, and hydrophobicity (*86*).

Besides surface modification, LbL assembly has been recognized as a versatile bottom-up method to fabricate micro/nanostructures such as capsules, nanowires, and nanotubes, since it enables conformal coverage on substrates (*85*). One of the strategies is that after the films are LbL assembled on a template of colloidal particles or nanoporous membranes, dissolution of the template leads to formation of hollow capsules or nanotubes (*87*). This requires polymer materials to be transported into confined structures such as polycarbonate nanoporous membranes. Unfortunately, LbL deposition in confined spaces has been not well understood and no systematic study has been undertaken, although the mechanism of LbL assembly in planar substrate has been well studied. It has been speculated that the confinement of polymer chains in pores of small size might affect significantly the growth mechanism of the multilayers (*88*).

LbL assembly in confined geometries has been studied previously in the context of coatings for microporous and nanoporous materials. Lee *et al*. (*89*) reported that PAH/PSS multilayers were successfully assembled within 400 and 800 nm cylindrical

pores. Bilayer thicknesses within the pores were found to be about 20% larger than on a flat substrate, a result that was attributed to incomplete drainage of solution from the pores during the assembly process. Lee *et al*. also reported that as the multilayers swell within the pores, they fail to completely close the cylindrical pores; interfacial stress caused by the shrinking cross section and electrostatic repulsion were offered as possible explanations for this observation. Similar PEM deposition experiments on nanoporous substrates were carried out by Alem *et al*. using poly(vinylbenzylammonium chloride) and PSS (*88*). They reported bilayer thicknesses within the pores that were forty times higher than those on a flat substrate and attributed this result to the formation of a dense gel within the pore due to higher local polymer concentrations. Another example of layer-by-layer polymer deposition in confinement is the tuning of photonic crystals using PAH and PSS as well as organometallic polyelectrolytes as reported by Arsenault *et al*. (*90*). Arsenault reported five times smaller bilayer thicknesses within the crystal than on the surface of the crystal and attribute this result to exclusion of polyelectrolytes due to confinement. Wang *et al*. (*91*) have also reported LbL deposition of PAH and poly(acrylic acid) (PAA) in mesoporous silica particles with 3 – 40 nm pores to form nanoporous polymer spheres after selective dissolution of the silica template. They showed that stable nanoporous polymer spheres could not be formed using porous silica particles with 2 – 3 nm pores, suggesting that these pores were too small to allow polyelectrolyte infiltration. These findings all indicate that the mode of multilayer growth during confinement would significantly differ from what occurs on planar substrate, but the reasons behind this are not known. In addition, it is not clear

whether LbL deposition would achieve conformal coverage in confined nanochannels/nanopores, especially in the case of high-aspect-ratio structures.

The regular high-aspect-ratio nanochannels, described in the chapter 2, would provide a well-controlled experimental platform to study this behavior. In this chapter, we study the growth behavior of polyelectrolyte multilayer (PEM) under confinement of high-aspect-ratio nanochannels. Conformal and uniform coating along the thickness of nanochannels has been observed. Slower deposition in nanochannels has been found than that on planar substrate. In addition, we have performed dc conductance measurements to obtain wet-state PEM thickness, allowing us to monitor film properties in situ (such as swelling/deswelling). PEMs can be used to impart a broad set of novel functionalities to a nanochannel device including stimuli-responsiveness, reversible switching of the channel gap thickness (*89*), manipulation of the sign and/or the density of the surface charge, chemical functionality and wettability of the channel walls. LbL assembly can also be used to incorporate functional nanoparticles and biomacromolecules within a surface coating, serving as a simple and general method for surface functionalization within the confined geometry of the nanochannels.

4.2 Experimental Section

4.2.1 Materials

Poly(allylamine hydrochloride) (PAH) (M_w = 56,000) and poly(sodium 4-styrenesulfonate) (PSS) (M_w = 70,000) were purchased from Sigma-Aldrich. NaCl was purchased from Mallinckrodt. Poly(dimethylsiloxane) (PDMS) was made using the Sylgard 184 kit from Dow Corning. The polymer mixture was cured with base and curing agent (10:1) at 65 °C overnight. Ag/AgCl electrodes were purchased from A-M Systems, Inc. and the conductivity probe and meter were obtained from VWR.

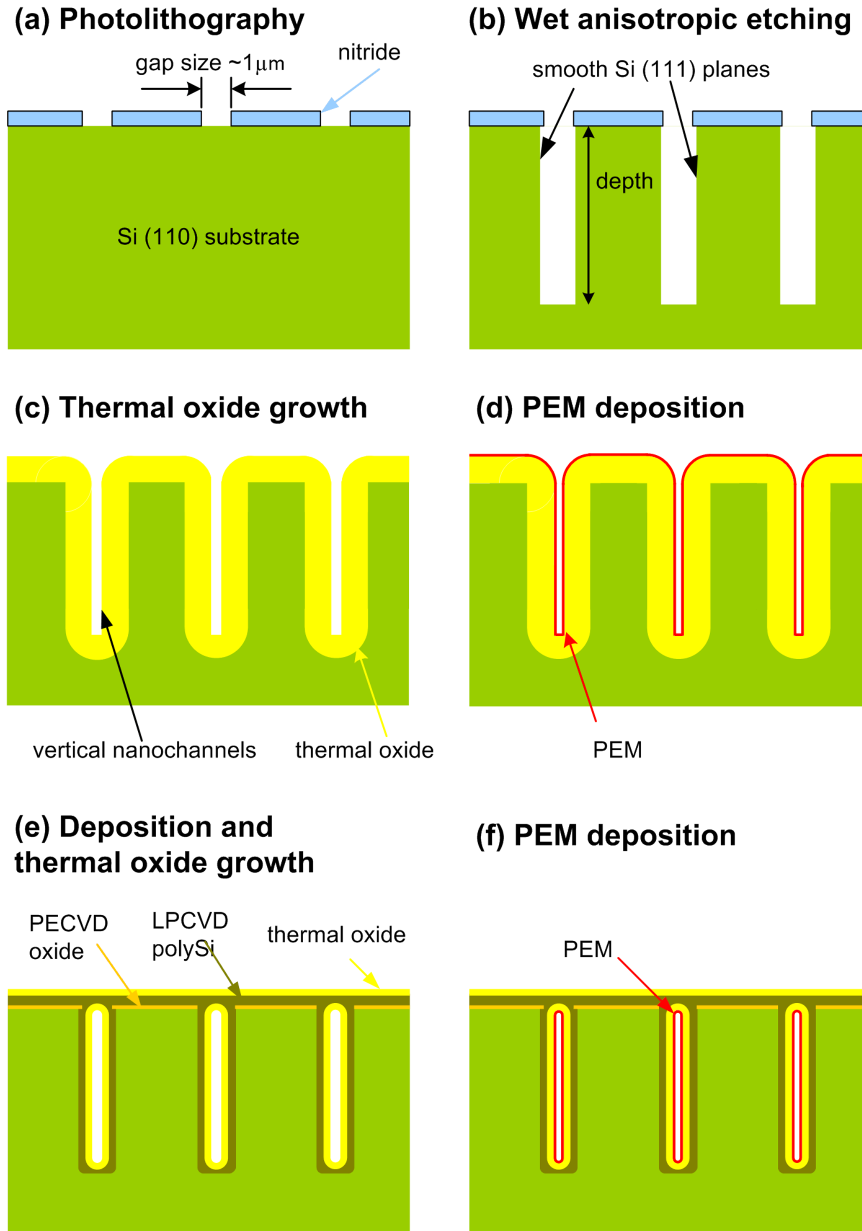

Figure 4.2 Schematic showing the fabrication process of nanofluidic-PEM channels. Two types of devices are used. (**a,b**) Channels are patterned and etched by photolithography and anisotropic wet etching. (**c,d**) For open nanochannel arrays, PEM is deposited on nanochannels from the top after thermal oxidation which narrows down gap size to form nanochannels. (**e,f**) For enclosed nanochannel arrays by the fabrication method II, thermal oxidation is performed after PECVD oxide and LPCVD polysilicon are deposited sequentially. PEM is deposited on nanochannels from the side.

4.2.2 Device Fabrication

The high-aspect-ratio nanochannels were fabricated using conventional semiconductor microfabrication techniques as described in Chapter 2 (*57*). Two types of devices were used in this work. The first device consists of a nanochannel array for characterizing PEM growth in open nanochannels. This device was fabricated with the first method shown schematically in **Figure 4.2(a-d)**. Briefly, a thin layer of low-stress, low-pressure chemical vapor deposition (LPCVD) silicon nitride was deposited on a (110) silicon substrate to provide a mask for KOH etching. Channel patterns were then defined by standard photolithography and etched to form narrow, deep trenches using anisotropic KOH etching (**Fig. 4.2ab**). After removal of the silicon nitride layer, an oxide layer with appropriate thickness was grown by thermal oxidation to narrow the gap size (trench width) down to the desired value (**Fig. 4.2c**). Finally, multilayers were grown in nanochannels from the top (nanochannel entrance) with dipping method described in the following section (**Fig. 4.2d**).

The second device consists of embedded nanochannel arrays bridged by microchannels for conductance measurements. The device layout is shown in **Figure 4.3**(**a**) and the fabrication process is outlined in **Figure 4.2**. In order to create both nanochannels and microchannels, the fabrication method II was utilized. Basically, after photopatterning and KOH etching of deep trenches (**Fig. 4.2ab**), PECVD oxide and LPCVD polysilicon were sequentially deposited on the trenches (**Fig. 4.2e**). The combination of the non-conformal PECVD and conformal LPCVD processes allows us to maintain a uniform gap size along the trench after deposition while sealing the trenches completely.

After sealing nanochannel arrays, microchannels were defined by standard photolithography and etched to the same depth as nanochannel arrays using deep reactive ion etching (DRIE) technique. Then, thermal oxidation was used to narrow the gap size within the nanochannel arrays to the desired value (**Fig. 4.2e**). All silicon surfaces were passivated with oxide to form an insulation layer for conductance measurements. Finally, multilayers were deposited in nanochannels from the side (interface between microchannels and nanochannels) with dipping method described in the following section (**Fig. 4.2f**).

In order to form functional devices, a bonding protocol was developed to cap all the channels (microchannels) after PEM deposition. As reported previously, O_2 plasma can be used to selectively etch a PEM film from an exterior surface, while leaving the same coating intact within small pores (*92*). We decided to utilize this method to remove the exposed PEM on device surface, which was covering the bonding surface, while leaving the coating inside the nanochannels intact. **Figure 4.4** shows cross-sectional SEM images of a nanochannel array which has been coated with 40 bilayers of PAH/SPS and subsequently etched in O_2 plasma at 100 mTorr and 100W for 2 min and 5 min, respectively. This micrograph shows that most of the polymer from the tops of the “posts” has been removed while the walls of the channel are still coated with the exception of the curved surface near the top of the post after 5 min of plasma treatment. Therefore, 8 sec of O_2 plasma etching per bilayer of PAH/PSS deposited is sufficient to remove the PEM film on the top surface while keeping the film inside the nanochannels intact. In fact, in the actual device, for which the nanochannel array is already capped

with a layer of SiO_2, we should expect less etch rate from the side than that from the top. These results show that we can expect etching from the side to remove less than 1 µm of polymer from each side of the 30 µm long nanochannels. After removing polymer films on the top surface, a slab of PDMS with pre-punched holes corresponding to the device reservoirs and the plasma-cleaned device were subjected to O_2 plasma for 1 min, and then aligned and brought into contact. The bonded device was then placed on a hotplate at ~90 °C for a few hours to increase the bonding strength.

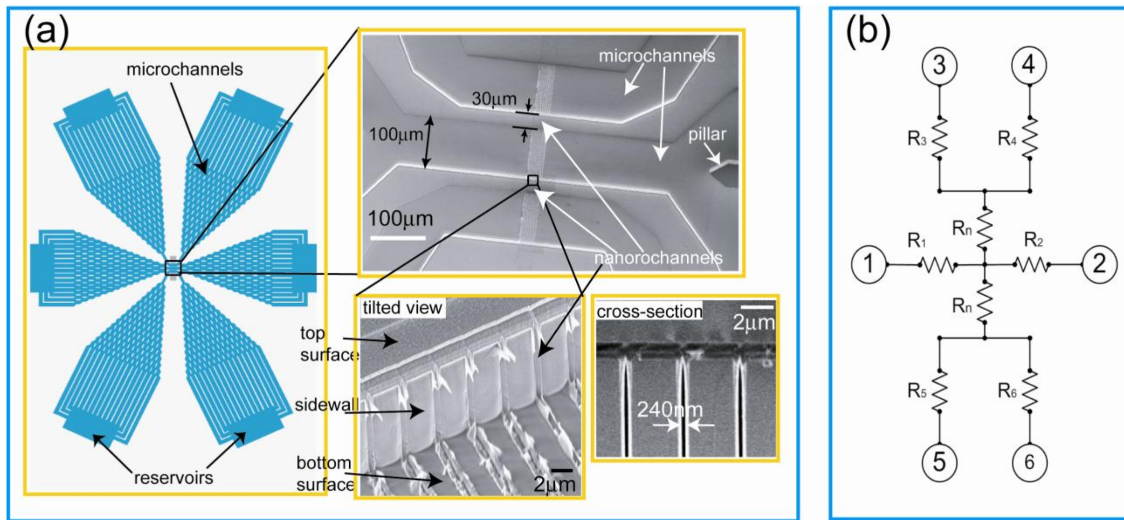

Figure 4.3 (**a**) Schematic and SEM images of the device used for the dc conductance measurement. The device consists of a nanochannel array which is bridged by two microchannels. The pyramid-shaped microchannels are used to ensure low resistance relative to the nanochannels and the pillars are required to prevent the channels from collapsing. The interface between the nanochannels and microchannels is shown in the tilted-view and cross-sectional SEM images. The nanochannel is 30 μm long and 240 nm wide. The width of the microchannels is 100 μm. All channels have a depth of 15 μm. The trenches in the bottom surface near the nanochannel array are due to the overetching of the nanochannel array pattern during subsequent etching of the microchannels. (**b**) The simplified equivalent circuit of the device employing the assumption of ideal, inert channels.

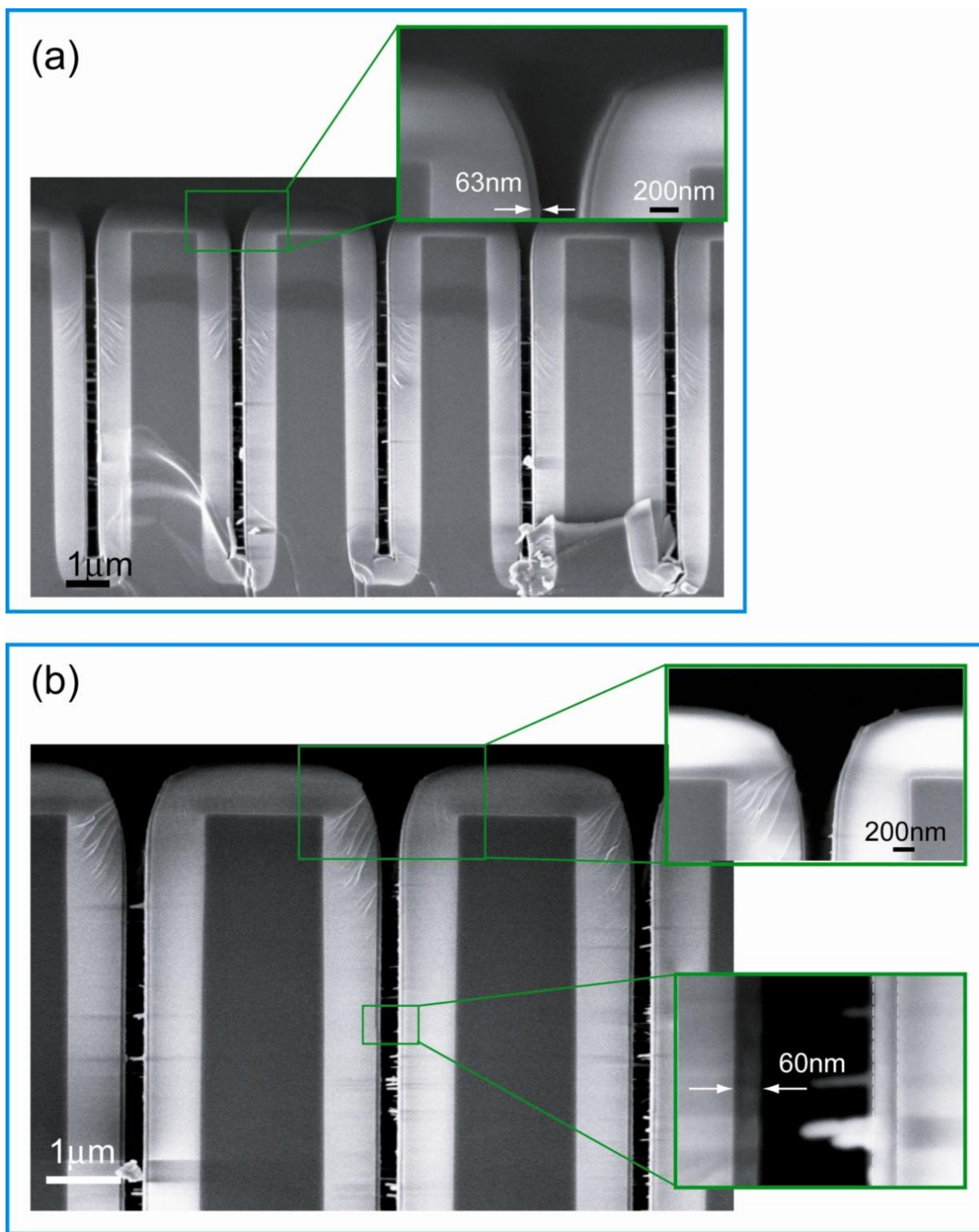

Figure 4.4 Cross-sectional SEM micrographs showing nanochannel arrays coated with 40 bilayers of PAH/SPS after plasma etching of 2 minutes (**a**) and 5 minutes (**b**), respectively. Most polymer film from the tops of the “posts” has been removed but the walls of the channel are still coated with the exception of the curved surface near the top of the post after 5 mins of treatment (**b**), while the film on top surface still remains with 2 mins of etching (**a**).

4.2.3 PEM Deposition

This step was done in Prof. Cohen's lab by Jonathan DeRocher, who was the main collaborator of this research. Silicon devices were mounted on glass slides using double-sided tape (468MP, 3M). Polyelectrolyte solutions consisting of 10 mM polyelectrolyte (on a repeat unit basis) and varying salt (NaCl) concentrations were prepared using deionized (DI) water (18 MΩ·cm, Millipore) and adjusted either to pH 4.0 using 1.0 M HCl (Sigma-Aldrich). The pH of the rinse water was also adjusted to match that of the polyelectrolyte solutions in order to avoid pH drift over the course of an experiment. The samples were dipped into baths containing polyelectrolyte and rinse solutions using a programmable slide stainer (Zeiss, Inc.). Since oxide surface is negative charged, the substrates were first dipped into the polycation (PAH) solution, followed by dipping into three rinse baths. The substrate was then dipped into the polyanion (PSS) solution followed by three rinses. This process, which constitutes one bilayer, was then repeated to form the PEM. Unless otherwise noted, the dip times for the polycation/polyanion and three rinse baths were 40, 10, 10, and 10 min respectively. Upon completion of PEM deposition, the samples were immediately dried with compressed air.

4.2.4 Multilayer Film Characterization

The thickness and conformality of PEM films assembled within the nanochannels were determined using scanning electron microscopy (SEM) (JEOL 6320, Zeiss Supra-40). The SEM samples were prepared by fracture of the coated silicon substrates using a diamond scorer. The fracture surface was along a crystal plane which was not

perpendicular to the channels, and hence in mounting the sample care was taken to ensure that the SEM view is as close to straight down the channels as possible. The dry film thicknesses of PEM films on the channel walls were measured using image analysis tools built into the SEM software. The micrographs were also used to qualitatively evaluate the roughness and conformality of the polymer coating.

To determine the dry PEM thickness on flat substrates, spectroscopic ellipsometry (XLS-100, J.A. Woollam Co., Inc.) was used. The thickness of the PEM in equilibrium with an aqueous solution was determined using *in situ* ellipsometry. In these experiments, the sample was placed in a custom-made quartz cell which was filled with the solution of interest. The resulting data were fit to a Cauchy model to determine the film thickness.

4.2.5 dc Conductance Measurement

The dc conductance measurements were used to determine the ionic flux through the channels, from which estimates of the gap thickness could be made. These experiments were performed using a Keithley 236 source / measurement unit. Before measuring the electrical conductance of a device, it was first soaked in a solution of 1M KCl overnight. The device was flushed with fresh KCl solution and allowed to stand for a few minutes to allow the liquid level in each reservoir to equilibrate. This was done to prevent pressure-driven flow from affecting the conductance measurements. The device was connected to the voltage source by two Ag/AgCl electrodes placed into two specified reservoirs. Ag/AgCl electrodes were used to prevent overpotential during the

measurement. We applied a low voltage sweep from -0.5 V to +0.5 V at a rate of 0.01 V/s. The Keithley 236 was controlled using a custom-made LabView 7.0 program. The dc conductances of channels were determined by fitting the slope of the ionic current as a function of the applied voltage (*I-V* plot). These plots always showed very linear behavior, confirming that we have an ohmic system.

The nanochannel conductance *S* can be simplified as (*93*)(in our case, *w* has the nanoscale dimension) :

$$S = \frac{1}{R} = (\mu_{K^+} + \mu_{Cl^-}) n_{KCl} e \frac{WH}{L} + 2\mu_{K^+} \sigma_s \frac{H}{L} \qquad (1)$$

Where *R* is the resistance, μ_i is the mobility of species *i*, n_{KCl} is the concentration of KCl, *e* is the elementary charge, σ_s is the surface charge density, and *W*, *H*, and *L* are the width, depth, and length of the nanochannel. At high salt concentrations (for example 1 M KCl), where $W \gg \lambda_D$ (*Debye length*) and $|\sigma_s| \ll enW$ we can ignore the second term, which is governed by surface charge, and assume idealized, inert channel behavior, modeled as ideal resistors (*94*). The equivalent channel circuit of the device is shown in **Figure 4.3b**.

To determine the conductance of the nanochannels, one must first account for the resistance due to the microchannels which connect the reservoirs to the nanochannel array. For the circuits between the reservoirs (1) and (2) we know that:

$$R_{12} = R_1 + R_2 = \frac{1}{S_{12}} \qquad (2)$$

Similarly, between (3) and (4), we have

$$R_{34} = R_3 + R_4 = \frac{1}{S_{34}} \qquad (3)$$

For the circuits which include the nanochannels we have:

$$R_{13} = R_1 + R_3 + R_n = \frac{1}{S_{13}} \tag{4}$$

$$R_{24} = R_2 + R_4 + R_n = \frac{1}{S_{24}} \tag{5}$$

Where R_n is the resistance of the nanochannel array. Solving for R_n we can write:

$$R_n = \frac{R_{13} + R_{24} - R_{12} - R_{34}}{2} = \frac{1/S_{13} + 1/S_{24} - 1/S_{12} - 1/S_{34}}{2} \tag{6}$$

The resistance of the nanochannels of cuboid shape is given by:

$$R_n = \frac{\rho L_n}{N H_n W_n} \tag{7}$$

Where ρ is the resistivity of the electrolyte (KCl) solution, L_n is the length of the nanochannel array, N is the number of nanochannels in the array, and H_n and W_n are the height and width of each nanochannel respectively. Solving for the channel width (W_n) gives:

$$W_n = \frac{2\rho L_n}{N H_n \left(\frac{1}{S_{13}} + \frac{1}{S_{24}} - \frac{1}{S_{12}} - \frac{1}{S_{34}} \right)} \tag{8}$$

Here S_{13}, S_{24}, S_{12}, and S_{34} are experimentally determined from the *I-V* curves. For the devices used in this paper, N = 10, L_n =30 µm, and H_n =15 µm. The conductivity values for 200 mM, 1 M, and 3 M KCl solutions were measured to be 25.01, 113.8, and 290.1 mS/cm, respectively, by a conductivity probe. From the gap size (width: W_n) of nanochannel, we can obtain the film thickness inside the nanochannel, which is:

$$d = (W_0 - W_n)/2 \tag{9}$$

Where W_0 is the gap size of nanochannel before PEM coating. Here we assume that the ionic transport inside the hydrated multilayer is negligible compared to the ionic flux through the open nanochannel. This assumption is justified since PEMs have conductivities of order 10^{-7} S/cm (*95*), while our electrolyte solutions have conductivities of order 10^{-1} S/cm.

4.3 Results and Discussion

4.3.1 Polyelectrolyte Multilayer Growth in Nanochannels

The assembly of PAH/PSS multilayers in open nanochannel arrays was investigated using SEM. **Figure 4.5** shows the cross-sectional SEM images of nanochannel arrays which were successfully coated with multilayers of PAH/PSS at pH 4.0. The figure shows that good coating uniformity was achieved along the entire depth of multiple channels. The nanochannels with 400 nm in width have been reduced to a gap size of 260 nm by the LbL deposition of a 70 nm thick PEM (**Fig. 4.5b**). We found the conformality of the coating to be sensitive to the deposition conditions. All depositions were performed with pH-adjusted rinse solutions and the sample was not allowed to dry until deposition was complete to improve the coating quality. Drying of the sample in the course of deposition leaded to bumpy films with bad surface quality. To further quantify the coating uniformity, SEM micrographs of various regions of coated nanochannel arrays were analyzed to determine the PEM thickness. Samples coated with 10, 20, 30, 40, and 60 bilayers of PAH/PSS assembled at pH 4.0 were used to perform this analysis. The results are summarized in **Figure 4.6**. The comparison of film

thickness in the various regions of nanochannels show that there is no systematic variation in the bilayer thickness along the depth into the nanochannel, suggesting that deposition under these conditions is not limited by diffusion of the polyelectrolytes into the nanochannels. In fact, the characteristic diffusion time for polyelectrolytes to travel through a nanochannel can be roughly estimated from the scaling of $\tau = L^2/D$, where diffusion constant D is around 10^{-7} cm^2/s (*89*). With a nanochannel depth of 15 μm, this leads to diffusion time one the order of ~ 1 min. Both the deposition time (40 min) and rinse time (30 min) used in this work are sufficient for the polyelectrolytes to get in and interact with surface (channel wall or polymer surface) as well as be removed in the rinse step. Hence, LbL assembly is not a transport-limited process but reaction (electrostatic interaction)-limited process, resulting in conformal coverage on surfaces. In Chapter 2, we have shown that the chemical vapor deposition (CVD) method proven to be challenging in achieving good step coverage in high-aspect-ratio channels. While CVD requires high-cost vacuum equipment, LbL assembly is quite inexpensive and easy. More importantly, LbL achieves uniform deposition along high-aspect-ratio nanochannels, enabling to build a novel surface-based device, nanofluidic-PEM membrane structures, with better performance and functionalities.

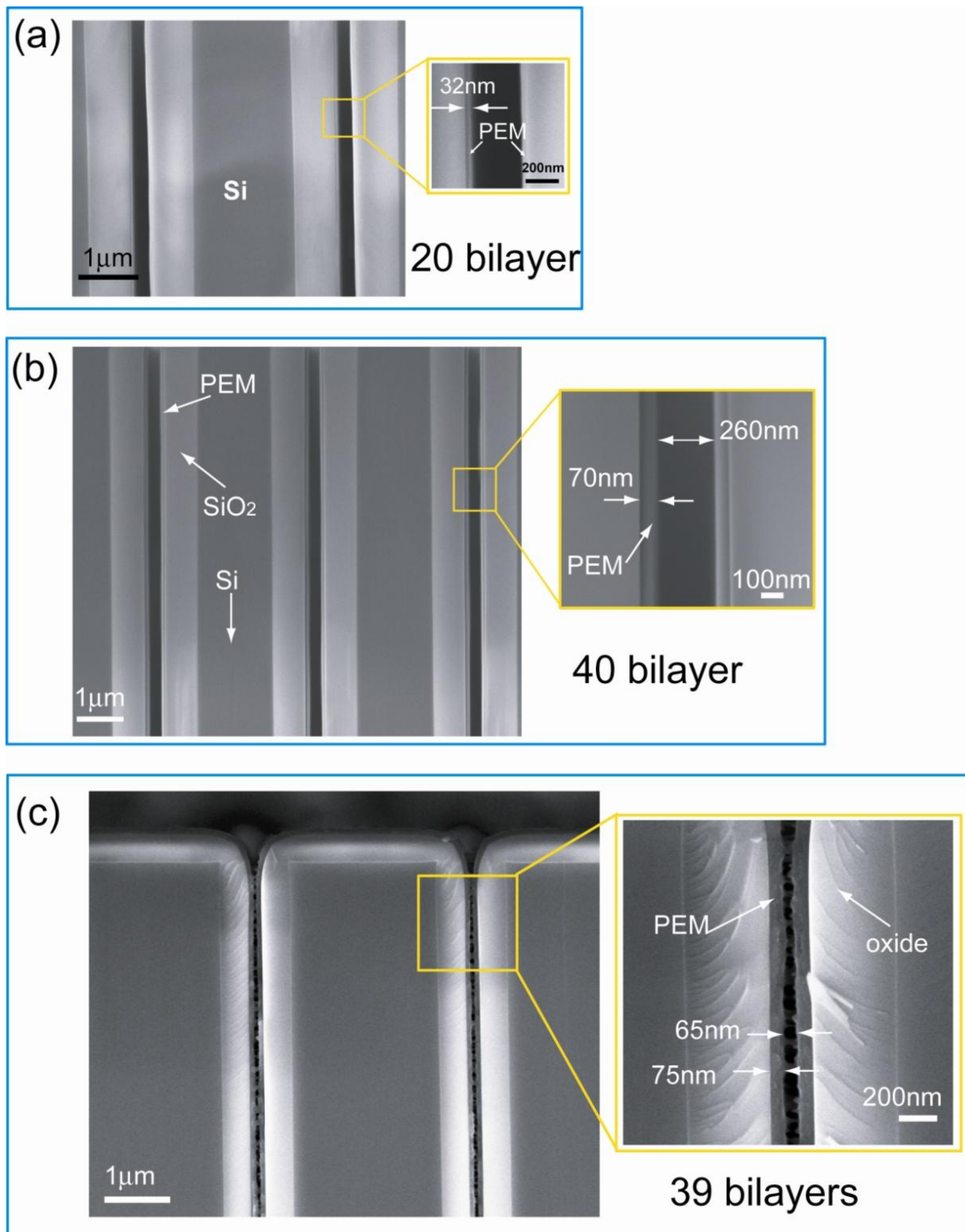

Figure 4.5 Scanning electron micrographs depicting conformal coating of 20 (**a**), 40 (**b**), 39 (**c**) bilayer PEM of PAH/PSS in an open nanochannel array. The silicon, thermally-grown oxide, and PEM layers are clearly visible and identifiable. The insets show the film thickness and gap size of the nanochannel. When the gap size becomes quite small, non-uniformity of film thickness along the channel depth as well as bridging effect emerges.

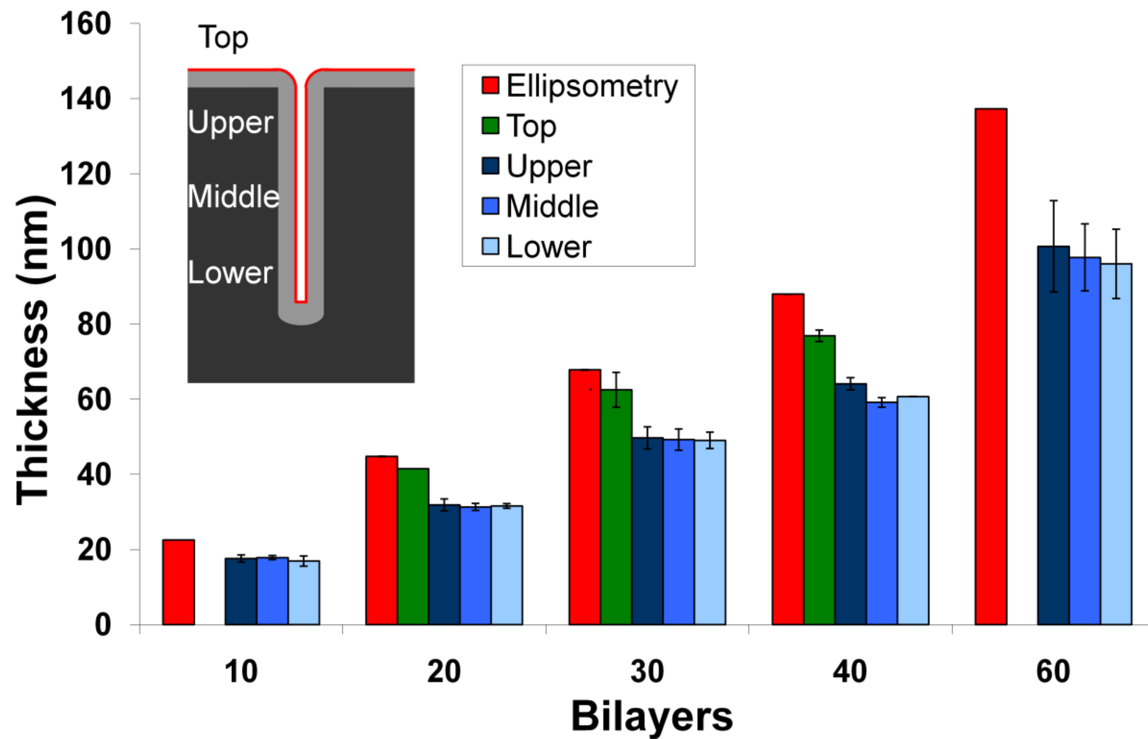

Figure 4.6 Comparison of dry state PEM thickness outside of and inside of a nanochannel with PEM thickness grown on flat surface. The red bars ("Ellipsometry") correspond to ellipsometry measurements on a flat silicon wafer. The green bars ("Top") correspond to SEM measurements of the unconfined PEM thickness on the top of the posts. The various blue bars ("Upper," "Middle," and "Lower") correspond to SEM measurements of the confined dry PEM thickness along the height of the nanochannel. Some of SEM measurements (green bars) are unavailable.

Interestingly, a significant difference between the multilayer thickness inside and outside (Top region) the nanochannel is observed (**Fig. 4.6**). Also, the multilayer thickness (green bars) on the top of posts qualitatively agreed with characterization of flat silicon control samples (red bars), which were coated using LbL under the same conditions as the nanochannel arrays. This indicates that SEM measurement of film thickness is in good agreement with ellipsometry measurement. Unfortunately, it is quite challenging to measure film thickness on the top of posts because of low contrast in SEM. Therefore, we compare PEM thickness in nanochannels with that on flat substrate measured by ellipsometry.

Table 4.1 Bilayer Thickness

Salt Concentration (M)	Flat Surface Bilayer Thickness (nm)	Nanochannel Bilayer Thickness (nm)
0.1	2.31	1.69
0.25	2.94	1.86
0.5	3.78	-
1.0	5.14	-

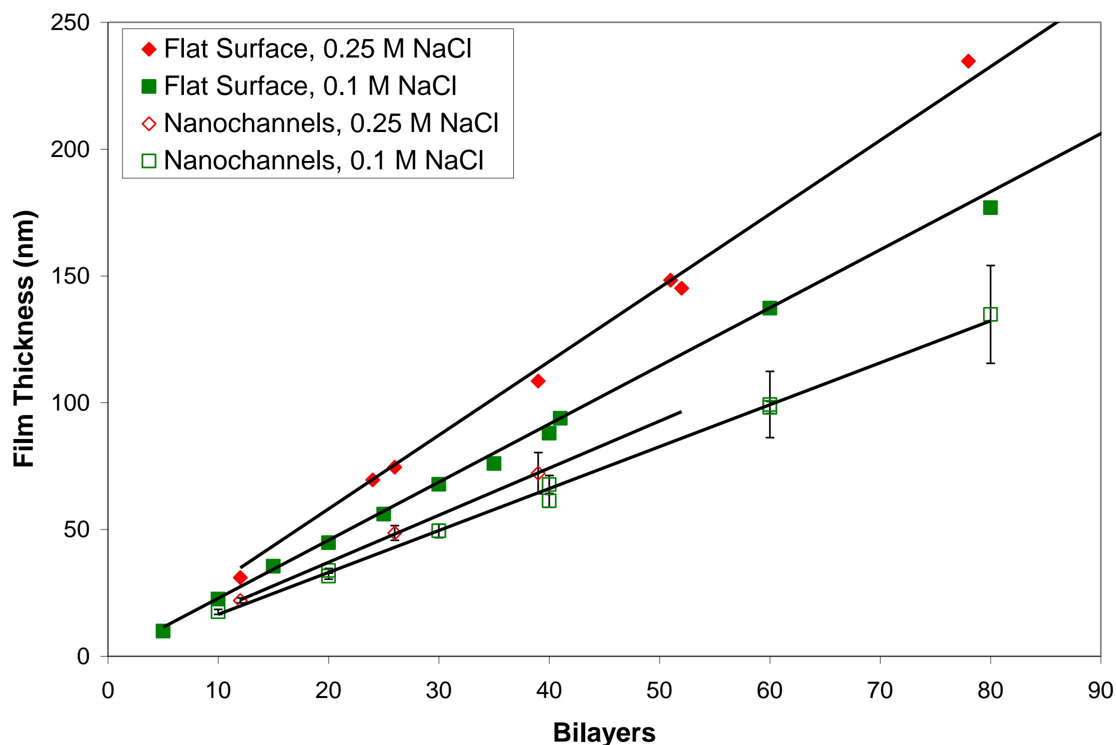

Figure 4.7 Comparison of dry-state PEM thickness in channels and on a flat surface at different ionic strengths. The filled red diamonds and filled green squares represent ellipsometry measurements of film thickness on a flat surface for 0.25 M and 0.1 M respectively. The open red diamonds and open green squares are the corresponding SEM measurements of film thickness within the channels. Linear growth is observed both on flat substrate and in nanochannels.

The PEM thickness on a flat Si substrate for various assembly cycles was measured using the spectroscopic ellipsometry to produce growth curves. Varying salt concentrations were also used in an attempt to determine how the bilayer thickness changes with increasing ionic strength in the polymer solutions. The data for 0.1 M and 0.25 M NaCl both in nanochannels and on flat substrates are shown in **Figure 4.7**. The fitted slopes of these growth curves, which represent the bilayer thickness, are presented along with results for 0.5 M and 1 M NaCl in **Table 4.1**. These data raise a few interesting points. First, both nanochannel and flat surface substrates show linear growth with all best fit lines going nearly through the origin. The linear growth in nanochannels indicates that the growth behavior is almost identical between 400 nm wide channels and 200 nm wide channels. Second, we see that the bilayer thickness on flat substrates is proportional to the square root of the ionic strength as observed by others (*82*). Most importantly, the data show that deposition within the nanochannels exhibit bilayer thicknesses clearly lower than those observed on flat surfaces. This result is contrary to the previous reports where significantly faster deposition within confined nanopores was observed (*88, 89*). One notable difference between the nanochannel and nanopore system is the confinement in one or two dimensions. In our nanochannel, the confinement only occurs in the width direction while both lateral directions are confined in nanopores. Presumably, we should expect less confinement effect on LbL deposition in nanochannels than in nanopores. However, the opposite effects (slower and faster) should not be expected to occur for deposition in nanochannels and nanopores. Polyelectrolyte complexation was attributed to explain much faster growth

(100 times) in nanopores (*88*), but we would think that non-uniform coating might occur in nanopores, and the film structure and properties might be much different from the films deposited on flat surface.

We believe that slower growth observed in nanochannels is due to the partitioning effect (*71*). The radius of gyration of polyelectrolytes used in this work is about 20 nm so the steric effect for polymer molecules would be very subtle in 400 nm wide channels. However, the highly charged surface would influence the transport as well as the conformation of polymers. More specifically, We believe that this result can be attributed to depletion of unadsorbed polyelectrolyte within the channel after charge reversal of the coated nanochannel walls occurs. Suppose that we start with a negatively charged surface which is dipped into a polycation solution. In the planar case, the positively charged polymer molecules are readily adsorbed at the surface creating a concentration gradient which results in a flux of more polycation molecules towards the surface. This continues until the surface charge reverses and increases to a point at which further adsorption is impossible due to electrostatic repulsion. In the nanochannel case, an additional step is added, namely diffusion of polymer molecules from the bulk into the confined channel. Now when surface charge reverses and increases, polycation molecules are essentially prevented from diffusing into the channel due to the repulsion of the closely-spaced, positively charged walls. This causes the concentration within the channel to drop uniformly, preventing further adsorption. In contrast to the planar case, adsorption in this case is limited by transport into the channel instead of electrostatic repulsion at the surface. This explains our observation

of thin, but uniform multilayers along the length of the channel. This effect is attenuated by the presence of ions in the solution due to electrostatic screening, thus at high ionic strengths we would expect to see similar bilayer thicknesses regardless of confinement. Depletion of polyelectrolytes confined between two charged surfaces has been predicted by Böhmer *et al*. using self consistent field simulations (*96*). More experiments and modeling will be performed to better understand this interesting behavior.

As we mentioned before, the uniformity and conformality of the PEM coating allow us not only to functionalize the surface of nanochannels, but also to tune the nanochannel gap size and reduce it uniformly to a desired value, which is crucial for nanofluidic applications. An important issue for this technique is how small the uniform gap size can be narrowed by growing multilayers in nanochannels. We have been able to reduce the gap size (open width of nanochannel) from 215 nm to 65 nm after deposition of 39 bilayers, as shown in **Figure 4.5**(**c**). Bridging of polymer between the sidewalls of the nanochannel was observed when the gap size was reduced to about 150 nm. More severe bridging took place as the gap size became smaller. As the gap size was further decreased down to ~ 50 nm, the entrance of the nanochannels became clogged. We believe the incomplete drainage of solutions during LbL deposition causes bridging inside the nanochannels. Increasing the rinsing time should attenuate this bridging effect. One the other hand, hindered diffusion of polyelectrolytes into nanochannels will emerge when the gap size of nanochannels is comparable to the radius of gyration (~10 nm) of the polyelectrolytes used here. This steric hindrance effect will cause the

conformational changes of polymer molecules and likely more severe bridging. The choice of lower molecular weight polymers will reduce these effects and bring the limitation of minimum gap sizes down to below 50 nm. Another improvement would be to perform LbL assembly using a high-flow filtration process (*88*), instead of the dipping method which relies on diffusion.

4.3.2 Wet-State Thickness of PEM Film

It has been well-established that polyelectrolyte multilayers swell significantly when immersed in salt solution (*88*). Thus the wet-state thickness of a PEM film should vary significantly from its dry-state thickness, which is measured by SEM or ellipsometry. In this thesis, dc conductance measurements are used to determine the wet-state thickness of a PEM film in a nanochannel as described above. Since high-aspect-ratio nanochannels have the advantage of high throughput (large open volume), the electrical resistance of the nanochannels is comparable to or even significantly smaller than that of the microchannels, especially for the nanochannels with large gap sizes. This fact raises the potential for significant errors in calculating the nanochannel gap size of using Equation (8). In order to improve the measurement resolution, we have significantly reduced the resistance of the microchannels by employing large, pyramid-shaped microchannels, as shown in **Figure 4.3a**. The dc conductances of channel circuits (S_{13}, S_{24}, S_{12}, and S_{34}) were determined by fitting the slopes of the *I-V* curves. All the *I-V* plots showed linear behaviors. **Figure 4.8** shows representative *I-V* curves from dc conductance measurements. This indicates that the measurements took place in the Ohmic regime (*97*), which verifies our ideal resistor model.

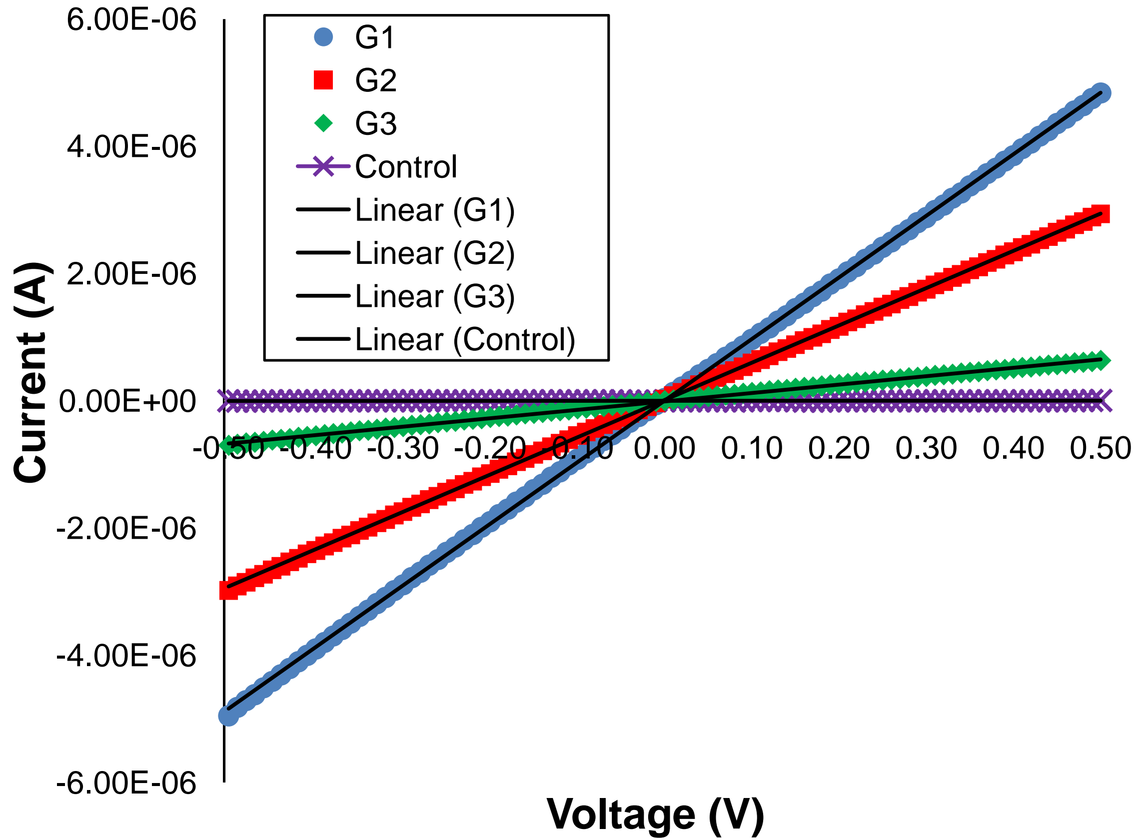

Figure 4.8 Representative *I-V* curves to determine the gap size of nanochannels. 40 bilayers of PEM is deposited in the nanochannels. The lines G1 (equivalent to S_{12}) and G2 (S_{34}) represent the *I-V* characteristics for the channel circuits between the reservoirs (1)-(2), and (3)-(4) respectively. G3 (S_{13} or S_{24}) represents the channel circuit which includes nanochannels. The control line shows the *I-V* characteristics for open-circuit with infinite load, indicating the resolution of the equipment Keithley 236. The dc conductances of channel circuits can be obtained by linearly fitting the slopes of *I-V* curves. All the curves show linear behaviors, verifying the idealized resist model.

Stein and his coworkers studied surface-charge-governed transport in nanofluidic channels (*94*). They observed that at low salt concentrations the electrical conductances of nanochannels saturated and became independent of both the concentration and channel height. For 70 nm deep planar nanochannels, the transition for salt concentrations between the bulk fluid behavior and surface-charge-governed behavior occurred around 10 mM, thus more concentrated electrolyte solutions were used in our experiments. To further verify our assumption of the bulk behavior and negligible surface charge effects on nanochannel conductance, we performed conductance measurement of nanochannels with various concentrations of KCl solution. **Figure 4.9** shows the measured final gap size of nanochannels, as a function of deposited bilayers ranging from 0 up to 60, in three salt concentrations of 200 mM, 1 M, and 3 M KCl. As expected, the nanochannel conductance varied linearly with salt concentration. No significant difference between the narrowed (final) gap sizes inferred from the measurements using the three different electrolyte solutions was observed. Therefore, the measured wet-state film thicknesses showed no dependence on the concentrations of salt solutions used. This confirms the validity of our treatment of the PEM-coated nanochannels as idealized, inert channels at high salt concentrations (for example, 1 M KCl).

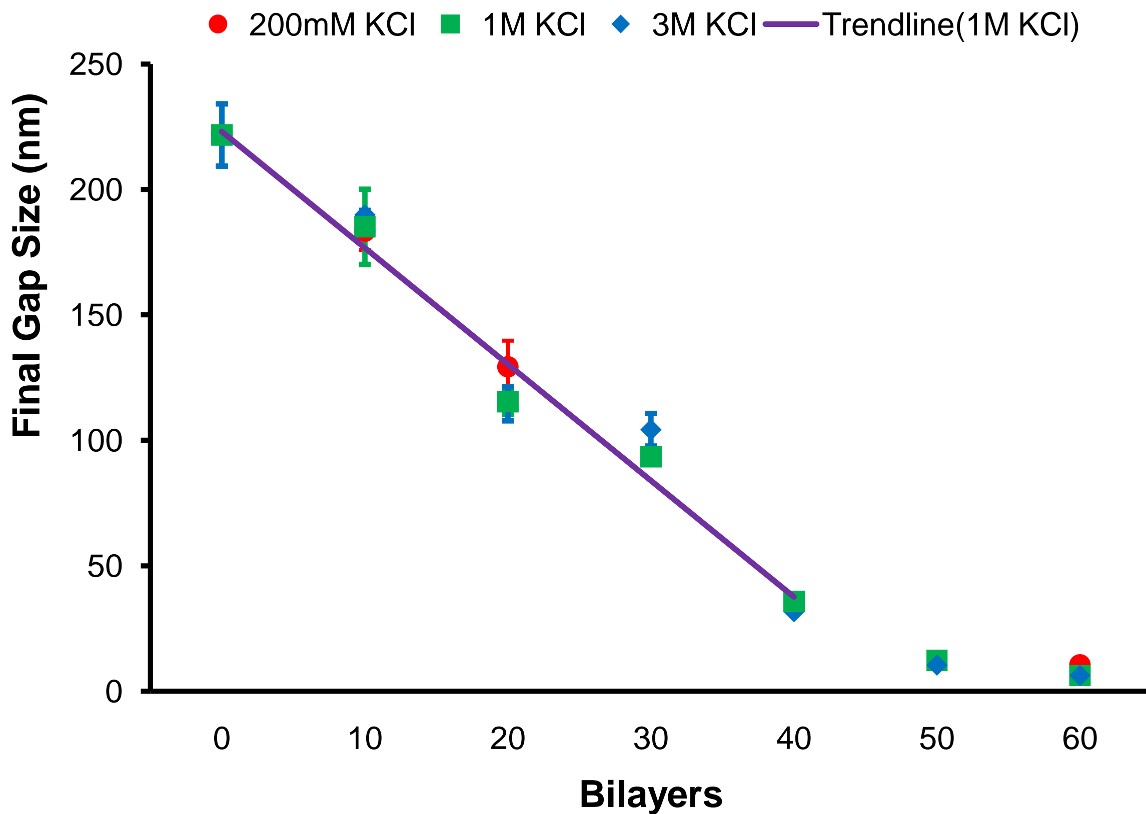

Figure 4.9 Comparison of the final gap sizes of nanochannels obtained by dc conductance measurements in 0.2M (red circle), 1M (green square), 3M KCl (blue diamond). No significant difference is observed. The straight trendline shows linear film growth behaviors from 0 to 40 bilayers, but after deposition of 50 bilayers the gap size becomes extremely small and plateaued. The no-coating gap size is about 225 nm.

We found out that the initial nanochannel gap size without coating of PEM was 225 nm from conductance measurements, which is nearly identical to 240 nm from SEM measurement as shown in **Figure 4.3a**. We also noticed that the measured swollen film thicknesses exhibited a linear growth behavior before deposition of 40 bilayers but saturation after 50 bilayers. This is due to the fact that the gap size of the nanochannels became extremely small and plateaued after more than 50 bilayers of PEM were deposited. In fact, the gap size of the nanochannels was only about 35 nm after 40 bilayers of PEM were deposited. This value is comparable to the radius of gyration of the polyelectrolytes (~ 10 nm), thus we would expect to see severe hindered transport of the polymer molecules, resulting in a failure to sustain uniform LbL assembly within the nanochannels after 50 bilayers. On the other hand, even with 60 bilayers of PEM coating, we were still able to obtain substantial readout of dc conductances of nanochannels. These results show that dc electrical conductance measurements are an accurate, efficient, nondestructive method for measuring the channel gap thickness.

For comparison, we used ellipsometry to measure both the dry state and wet state thicknesses of a PEM film on a flat silicon wafer. These results are compared in **Figure 4.10**. The percent (%) swelling of the multilayers deposited on flat substrate, defined as (wet thickness - dry thickness)/dry thickness × 100%, was calculated to be about 23%. This value agrees fairly well with the swelling ratio of 1.22 for PAH/PSS, defined as the ratio between the swollen and dry thickness, reported previously (*98*). We also compared the dry and swollen thicknesses of multilayers in nanochannels, as shown in **Figure 4.10**. The wet-state bilayer thickness was obtained by fitting the slope

of the wet thickness as a function of bilayers from 0 to 50. Comparing with the dry bilayer thickness obtained by SEM, the multilayers in nanochannels swelled by about 39%, which is a little larger than 22% of the swelling percentage on flat substrates. A part of this difference could be due to the small error brought in by conductance measurement. In spite of this, we believe that this measurement of wet state PEM thickness is consistent with SEM results, indicating that the mode of LbL assembly under confinement in nanochannels would not significantly differ from the one on flat substrate. In addition, the structure and property of multilayers grown in nanochannels would be similar to that grown on planar substrates.

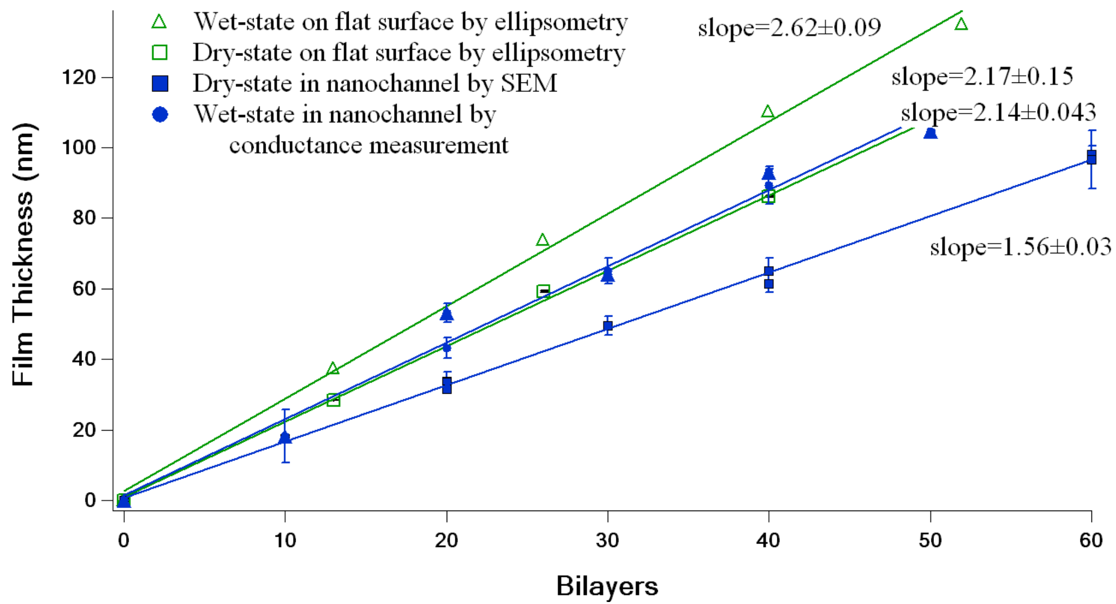

Figure 4.10 Comparison of the dry-state (diamonds) and wet-state (circles) multilayer thicknesses both on flat substrate (open) and in nanochannels (filled). Both the dry- and wet-state film thicknesses on flat surface are determined by ellipsometry. The wet-state PEM thicknesses in nanochannels are obtained by dc conductance measurements in 1M KCl. The bilayer thickness of PEM film is obtained by fitting the slope linearly.

4.3.3 Applications

Wang *et al.* has reported that planar nanofluidic channels can be used as a perm-selective membrane to generate an ion depletion region and highly efficient sample preconcentration (1 million fold) has been achieved (*66*). It is interesting to see that, even at the ionic strength as high as 10 mM (*Debye* layer ~ a few nm) and in the channel as deep as 40 nm, one could observe the effect caused by electric double layer. However, they also found that the concentration plug would not be stable with microchannels deeper than 10 μm and concentration polarization would fail with high ionic strength buffer (such as 100 mM). The novel nanofluidic-PEM channels are believed to have strong depleting force and hence allow concentration polarization at high ionic strength buffer, because of highly changed PEM surface. As proof of concept, we fabricated a preconcentration device using the second fabrication method of vertical nanochannels as shown in **Figure 4.11a**. The layout design is similar to the chip as reported by Wang *et al.* (*66*), except the planar nanochannel array replaced with vertical nanochannel array. After coated with 40 bilayers of PEM, the original gap size, 170 nm, of this nanofluidic-PEM device before coating is reduced to less than 20 nm.

We first tested 100 mM phosphate buffer (*Debye* length ~ 2nm). As expected, after applying voltage across the vertical nanochannel coated with PEM, FITC was trapped in front of nanochannels and concentration plug was formed (**Fig 4.11b**). More than 100 fold increment of fluorescence intensity was observed within a few minutes. Interestingly, we observed the concentration effect even in 1M KCl, although weird phenomenon happened. Our observation suggests that at high ionic strength conditions,

the nominal *Debye* length becomes negligible compared to the gap size of nanochannel, but the effect due to surface charge would play a dominant role in transport of ions/molecules into a nanochannel. Other merits of this device are its high throughput and at least 10 times higher sample concentration volume has been achieved than in the planar nanochannel device. The potential of vertical PEM nanochannels has been demonstrated to improve the performance as well as bring new functionality to nanofluidic systems. More work is required to investigate the applicability of this novel device.

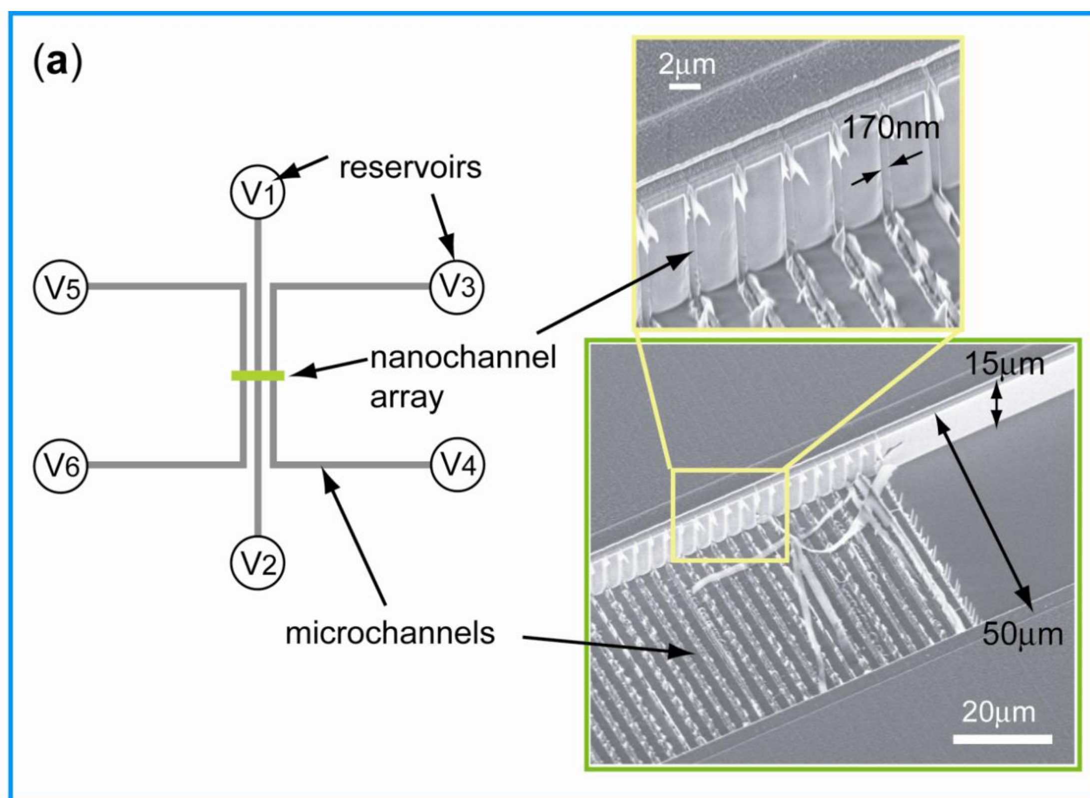

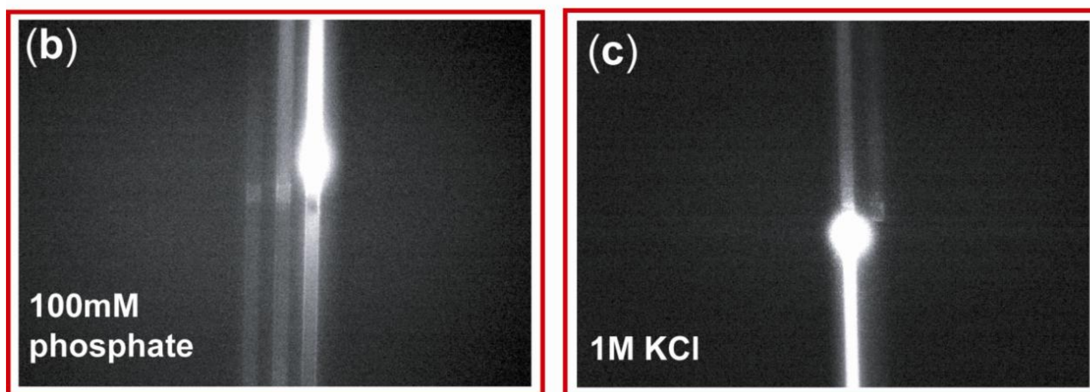

Figure 4.11 The high-throughput concentration device. (**a**) The layout of the device. The vertical nanochannel array is bridged by two microchannels, which are 15 μm deep and 50 μm wide. The gap size of nanochannel is 170 nm before PEM deposition. (**b**) Fluorescence micrograph showing sample concentration. The sample is FITC with a concentration of 1 μg/mL in 100 mM phosphate buffer. V_1=V_2=0, V_3=70v, V_4=50v, V_5 and V_6 are floated. (**c**) Fluorescence micrograph showing sample concentration in 1M KCl. V_1=V_2=0, V_3=80v, V_4=50v, V_5 and V_6 are floated.

4.4 Summary

In summary, we have studied the layer-by-layer deposition of weak polyeletrolytes within confined high-aspect-ratio nanochannels. Conformal, uniform deposition has been achieved along the entire depth of the nanochannel, and linear growth has been observed. Compared with the growth on flat substrate, significantly slower deposition per bilayer within nanochannels was found, which we would attibute to the partioning effect. The reasons for this behavior are still under investigation. We also have performed dc conductance measurements to determine the wet-state thickness of PEM. The swelling percentage of PEM deposited in nanochannels is a little higher, but close to the one on flat surface, indicating that the mode of growth of LbL assembly under confined nanochannels is not significantly different from that of flat LbL multilayers. Our results are contrary to the observations previously reported on nanopores.

We believe that these novel nanofluidic-PEM channels (vertical nanochannels coated with PEM) would provide an ideal experimental platform to study this interesting behavior and contribute to better understand fundamental physics of transport in confined environments. In addition, this novel device could be useful in many applications with better performance and new functionalities. As proof of concept, we have demonstrated high-throughput preconcentration at high ionic strength buffer.

Chapter 5

Conclusions and Outlook

5.1 Thesis Contributions

Sample preparation has been the bottleneck in proteomics because protein samples are diverse, complex, and of enormous dynamic range. Recent advances in micro/nanofluidic technologies have opened up new opportunities for sample preparation of proteomics, aiming at the integration of miniaturized, automated, multi-step bioanalysis systems. In contrast with the microchip-based CE and LC systems which still utilize conventional polymeric gel materials as sieving matrix, the development of regular artificial nanofluidic structures holds great promise as an alternative to random gel materials towards optimization of performance as well as complete chemical and bioanalysis microsystems. However, most microfabricated nanofluidic channels, such as planar nanochannels and square nanochannels, suffer from small open volume and, as a result, low sample throughput, compared to conventional gel-based systems. For practical and wider applications of artificial nanochannels, it is of crucial importance to enhance sample throughput of nanofluidic systems. To address this severe problem, we have built high-aspect-ratio vertical nanochannels, which have the advantage of large open volume, enabling for high-throughput applications.

This thesis is the first to demonstrate the development and implementation of high-aspect-ratio nanochannels for high-throughput biological applications. Two

fabrication methods for creating massively-parallel, ultrahigh-aspect-ratio nanochannels have been developed by using a combination of anisotropic wet etching and thermal oxidation. Vertical nanochannels with a uniform gap size of 55 nm and aspect ratio as high as 400 have been demonstrated. As an example of application, we have implemented high-aspect-ratio nanochannels into a two-dimensional anisotropic nanofilter array (ANA) device and demonstrated continuous-flow separation of DNA and proteins. Compared with other nanofilter devices, the vertical ANA device achieves comparable speed and efficiency but allows a much higher sample throughput. In addition, these vertical nanochannels are robust and scaled-up and would be ideal artificial nanofluidic structures as an alternative to the conventional gel-based systems. This thesis will pave the way for widespread application of solid-state, regular nanofilters in various membrane / filtration / separation applications, without suffering from the volume throughput limitation.

Also, this thesis is the first to demonstrate the uniform layer-by-layer deposition of polyelectrolyte multilayers within high-aspect-ratio nanochannels. Conformal, uniform deposition has been achieved along the entire depth of the nanochannel and linear growth has been observed. Compared with the growth on flat substrate, significantly slower deposition per bilayer within nanochannels was found, which we attibute to the partioning effect. We also have performed dc condutance measurements to determine the wet-state thickness of PEM. The comparison of dry-state and wet-state thicknesses indicates that the mode of growth of LbL assembly under confined nanochannels is not significantly different from that of LbL multilayers on flat substrate.

We believe that these novel nanofluidic-PEM channels would provide an ideal experimental platform to better understand fundamental physics of transport in confined environments. Besides, the ability of PEM coating provides new functionalities on nanofluidic systems. As proof of concept, we have demonstrated high-throughput preconcentration at high ionic strength buffer.

5.2 Ongoing Work:

Multi-Scale Continuous-Flow Filtration of Raw Biosamples

In most cases, the biological samples are a highly complex fluid mixture of objects of various sizes and shapes. Sample preparation of raw biosamples such as blood involves a broad size range of its components ranging from several microns for cells (white blood cells and red blood cells) down to a few nanometers for proteins and small molecules. To filter out specific molecules, several disjointed removal steps are often required, which can be time-consuming and can lead to a substantial sample loss after each sorting step. In general, multi-scale size-based sorting, if available, could provide an efficient separation method for all biological samples requiring separation of components with different size scales.

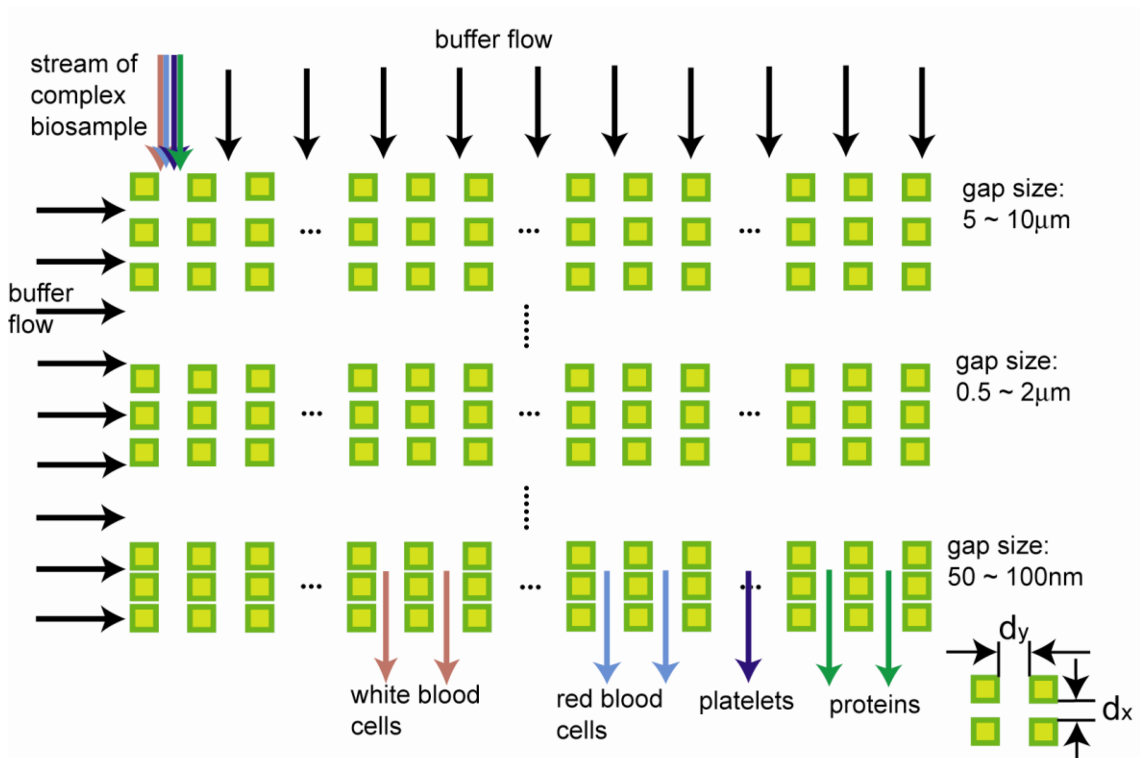

Figure 5.1 The concept of integrated multi-scale continuous-flow sorter. The vertical filter gap size decreases progressively from ~10 μm down to ~50 nm, in order to realized the continuous flow sorting of both cells and DNA/proteins. The size of the filter as well as its number can be freely varied in each segment to accommodate different sample sizes. The fractionated sample can be harvested into different outlet reservoirs after separation.

Inspired by the concept of the anisotropic nanofilter array (ANA), we propose to integrate a series of filters with gradually decreasing filter sizes into a single chip while allowing high sample throughput in a continuous mode. This continuous-flow filtration based on ANA can be equally applied to both molecular (10 nm or less) and cellular (1~20 μm) size scales. As a result, one can build a cell and/or large particle separation system and combine it with a molecular separation filter using the same asymmetric filter concept, as shown in **Figure 5.1**. To achieve this multi-scale filtration in a continuous-flow fashion, we fabricate a different set of filters with different sizes and arrange them in a gradually decreasing order of the filter size. When a raw sample is injected into the ANA device, the large components of the complex biosample in the order of few microns and higher, e.g., white blood cells in the case of blood sample, are filtered out first. At the following filter set with a filter size between 0.5-2um, objects such as RBC, organelles, viruses and vesicles are filtered out and collected. At the last filter with a filter size smaller than 100 nm, molecules such as large proteins, DNA and RNA are filtered out while small proteins, DNA/RNA and cytokines pass through and collected at the end of ANA. Using the microfabrication technique, the gradient of the filter size and the number of the filters can be varied flexibly to accommodate the different sizes of the raw sample and to increase the sorting resolution and purity. For instance, we can easily put more of the filter arrays to increase the trapping efficiency of specific cell types. In order to multiplex the sample processing, we can also fabricate several separators on a single wafer in the radial direction with a common inlet for the

sample injection. The proposed hybrid nanofilter sorting device has the potential to become a generic sample preparation tool.

The integrated multi-scale continuous-flow sorter will be unique in the following aspects. First, most previous cell-sorting micro devices suffer from relatively low throughput, due to the small depth of the channel fabricated (*99, 100*). With the new high-aspect-ratio nanochannel fabrication technology, our device allows more than 50 fold higher throughput than any of the demonstrated devices. Another important advantage is the significantly reduced clogging of filters. For most previous microdevices, it has been an intrinsic problem of the particle clogging at the filter when large particles are trapped at the small filter, thus interrupting the separation process. Our two-dimensional ANA device circumvents this problem by applying a two-directional flow. All the particles larger than the filter size are flushed away from the filter by the vertical component of the flow continuously and therefore, the membrane remains intact for the continuous operation. This self-cleaning effect of the membrane is a major advantage of the 2D continuous fractionation over the conventional 1D method.

5.3 Outlook and Future Direction

This thesis focuses on the development of high-aspect-ratio nanochannels, which represents a major step towards developing ideal artificial nanofluidic structures as a replacement of gel-based systems for sample preparation of proteomics. The fabrication of vertical nanochannels has been well characterized in this thesis, but the limitations of the two methods have not been completely explored, which should be explored in the future. In addition, thermal oxidation of three-dimensional structures such as silicon pillars has not been well understood, but it is important to precisely control the final gap size of nanochannels. Hence, more theoretical and simulation modeling approaches should be undertaken to study the effects of stress involved in oxidation process.

In this thesis, the 2D vertical ANA device has been built to accomplish continuous-flow separation of DNA and proteins. Although the proof-of-concept results have been achieved, the ANA device should be further optimized to improve its separation efficiency (size selectivity) comparable to the gel-based techniques. As mentioned in Chapter 3, scaling down the structural parameters such as nanofilter gap size and pitch size, which increases the number of nanofilters, will improve the separation resolution of ANA device. In addition, it is possible to extend the separation functionality of the ANA structure by utilizing the *Debye* layer, electro-osmosis, and surface chemistries, together with the geometrical constraints of the ANA, to achieve biomolecule separation based on a suite of molecular properties.

In the last part of this thesis, it is demonstrated that layer-by-layer assembly of polyelectrolyte multilayers can be incorporated into nanofluidic channels to provide new

functionalities with desired surface properties such as surface charge density, charge polarity, and hydrophobicity. This will open up numerous opportunities for wider applications of nanofluidics. The potential for sample preconcentration has been demonstrated in the thesis and more work is required to characterize concentration performance in the future. Another application is that proper surface polyelectrolytes can be chosen to coat vertical nanochannels to simulate Nafion membranes for fuel cell applications. Also, since some PEM swells as a function of solution PH, the fabrication of stimuli responsive nanofluidic-PEM membranes can be used to regulate or gate nanochannels for separation and detection of biomolecules such as proteins. From a scientific point of view, the regular nanofluidic-PEM channels will provide an ideal platform to study ion transport characteristics in nanochannel system as well as to understand the growth mechanism of LbL assembly in confined environments.

Appendix I

FABRICATION of VERTICAL ANA DEVICES

Patterning alignment marks to find (111) planes of (110) wafer

● TIMING ~ 2 d

1 | Start with a new 6” (110) wafer, immerse the wafer in the RCA-1 solution (1:1:5 solution of NH_4OH + H_2O_2 + H_2O) at 80°C for 10 min, and dump rinse the wafer with DI water for 10 min.

2 | Transfer the still-wet wafer to the diluted HF solution (DI:HF=10:1) for 1 min to remove hydrous oxide film formed during Step **1**, and dump rinse the wafer with DI water for 10 min.

3 | Immerse the still-wet wafer from Step **2** into the RCA-2 (1:1:6 solution of HCl + H_2O_2 + H_2O) solution at 80°C for 15 min, dump rinse the wafer with DI water for 10 min, and spin dry the wafer.

! CAUTION RCA-1 and RCA-2 are extremely corrosive. HF is an extremely hazardous liquid and vapor, and is highly corrosive to eyes and skin. Proper goggles, aprons, and gloves must be used during operation.

4 | Deposit a thin layer of low-stress silicon nitride on both sides of the wafer in the VTR vertical LPCVD furnace. The thickness of the nitride film is about 300 nm.

▲ CRITICAL STEP The nitride film should be deposited as quickly as possible after Step **3** to minimize re-growth of the oxide. Only the low-stress silicon nitride film can serve as a suitable etch mask for the KOH etching, since the conventional high-stress silicon nitride film tends to possess pinholes and cracks during the KOH etching step.

5 | Measure the nitride film thickness with the spectroscopic ellipsometer.

■ PAUSE POINT The wafer is stable in a dry and clean environment for a long period.

6 | Bake the wafer at 200°C for 10 min on a contact hotplate to dehydrate the wafer, let the wafer cool down to room temperature, and prime the wafer with HMDS vapor in a vacuum desiccator for 10 min.

! CAUTION HMDS is a flammable liquid and vapor. It is harmful if inhaled or absorbed through skin. Handle HMDS in a vented chemical hood with care.

7 | Static dispense the Shipley SPR700-1.0 photoresist (~5 ml) on the center of the wafer, spin at 500 rpm for 8 s to spread a uniform photoresist layer across the entire wafer, accelerate the wafer quickly to a final spin speed of 4600 rpm, and spin for 30 sec.

▲ CRITICAL STEP The wafer should be coated with photoresist as quickly as possible after HMDS priming, and it is recommended that coating be performed no later than 60 min after completing the priming step.

8 | Soft bake the wafer at 95°C for 60 s on a contact hotplate to drive off solvent from the spun-on photoresist.

9 | Expose the wafer using the EV620 mask aligner for 3 s with an exposure dose of 170 mJ/cm^2. The chrome photomask I with the alignment marks for determining the (111) planes of Si (110) wafers is used.
10 | Post-exposure bake the wafer at 115°C for 60 s on a contact hotplate.
11 | Develop the wafer with Shipley CD-26 developer for 30 s, dump rinse the wafer with DI water for 10 min, and spin dry the wafer.
12 | Inspect the wafer under the optical microscope to determine if the desired patterns on the mask have been successfully transferred to the photoresist. If not, strip the photoresist with the Piranha solution, and restart the coating process from Step 6.
▲ CRITICAL STEP The after-develop-inspection step is critical for monitoring if a) the correct mask has been used; b) the qualities of the photoresist film are acceptable; c) the critical dimensions are within the specified tolerances; d) the registration or mask alignment is within specified limits.
13 | Hard bake the wafer at 130°C for 60 s on a contact hotplate.
14 | Measure the thickness of patterned photoresist film after the hard bake step with the surface profilometer. The thickness of the photoresist layer should be about 1.0 µm.
■ PAUSE POINT The wafer patterned with photoresist is stable in a dry and clean environment for at least one week.
15 | Etch the nitride layer through the opened photoresist area using CF_4 and O_2 plasma, the etch rate of which can be tightly controlled to be about 3.4 nm/s using the SiN-etch recipe listed below.
Gas: CF_4 (8 sccm), O_2 (6 sccm)
Pressure: 50 mTorr
RF Power: 250 W
Nitride etch rate: 3.4 nm/s
16 | Strip photoresist with the Piranha solution for 10 min, dump rinse the wafer with DI water for 10 min, and spin dry the wafer.
! CAUTION The Piranha solution is hot and corrosive. Proper goggles, aprons, and gloves must be used during operation.
17 | Measure the nitride etch depth with the surface profilometer to ensure the nitride layer etched through. The uniformity of the nitride etch profile can be monitored with the surface profilometer to be less than 8% across the entire wafer.
18 | Dip the wafer into the diluted HF solution (DI:HF=50:1) for 30 s to remove native oxide on the wafer, dump rinse the wafer with DI water for 10 min, and spin dry the wafer. Etch the wafer with the KOH solution (44% by weight) at 73°C for at least 30 min to find the (111) planes. The Si etch rate in the 73°C KOH solution is about 1 µm/min.
! CAUTION The KOH solution is extremely hot and corrosive. Proper goggles, aprons, and gloves must be used during operation.
19 | Dump rinse the wafer with DI water for 10 min, and spin dry the wafer.
20 | Immerse the wafer in the Piranha solution for 10 min, and dump rinse the wafer with DI water for 10 min.
21 | Immerse the still-wet wafer from Step **20** into the second Piranha solution for 10 min, and dump rinse the wafer with DI water for 10 min.

22 │ Immerse the still-wet wafer from Step **21** into the diluted HF solution (DI:HF=50:1) for 1 min, dump rinse the wafer with DI water for 10 min, and spin dry the wafer.
▲ **CRITICAL STEP** Steps **20**-**22** are necessary to remove KOH contaminants.
23 │ Inspect the fan-shaped alignment marks under the optical microscope to locate the etched trench with the minimum undercut after KOH etching (**Fig. I a**), which represents the real (111) planes. An alignment mark with the diamond-shaped window is also designed for additional confirmation of the (111) planes (**Fig. I b**).
▲ **CRITICAL STEP** Step **23** is critical to find the (111) planes on the (110) Si wafer. The Si etch should be deep enough for sharp contrast between the adjacent trenches with different levels of undercuts.
■ **PAUSE POINT** The wafer is stable in a dry and clean environment for a long period.
? TROUBLESHOOTING

Patterning alignment marks for Nikon stepper ● TIMING 4~6 h

24 │ Repeat from Steps **6** to **17** to pattern the photoresist layer for the alignment marks of the Nikon stepper, etch the nitride layer, strip photoresist with the piranha solution, dump rinse the wafer with DI water, spin dry the wafer, and measure the nitride etch depth with the surface profilometer. The chrome photomask II with the alignment marks for the Nikon stepper is used.
▲ **CRITICAL STEP** During the exposure step, the features on the mask must be aligned to the (111) planes as determined in Step **23**, not to the wafer flat. The etch depth of the nitride layer should be around 100 to 200 nm, less than the total thickness of the nitride layer. Exposing the underlying silicon surface (if the nitride layer is etched through) will cause damage to the Nikon stepper alignment marks during the following KOH etching.
■ **PAUSE POINT** The wafer is stable in a dry and clean environment for a long period.

Fabrication of ANA narrow channels ● TIMING ~1 d

25 │ Repeat from Steps **6** to **23** to pattern the photoresist layer for the ANA narrow channels, etch the nitride layer, strip the photoresist with the piranha solution, dump rinse the wafer with DI water, spin dry the wafer, measure the nitride etch depth with the surface profilometer, etch the wafer with the KOH solution, and clean the wafer to remove KOH contaminants. The stepper reticle (mask III) with channel patterns is used.
▲ **CRITICAL STEP** Please note that the vertical ANA narrow channels are etched in the KOH solution at room temperature. The Si etch rate of the KOH solution at room temperature is about 75 nm/min. Si trenches with uniform etch depths across the entire wafer can be fabricated under this condition. The stepper is used instead of EV1 to define narrow channels.
■ **PAUSE POINT** The wafer is stable in a dry and clean environment for a long period.
? TROUBLESHOOTING

Fabrication of ANA wide channels and other microfluidic channels

● TIMING 2~3 d

26 | Deposit a thick layer of oxide (~ 3 µm) on the wafer using the PECVD system to seal the ANA narrow channels.
Gas: SiH_4 (50 sccm), N_2O (800 sccm)
Pressure: 2.7 Torr
Temperature: 400 ^oC
RF Power: 270 W
Oxide deposition rate: 10 nm/sec

▲ CRITICAL STEP Step **26** is critical to cover deep trenches of the ANA narrow channels and therefore ensure uniform photoresist coating on the wafer. The thickness of this PECVD oxide layer might vary with different trench dimensions.

27 | Repeat from Steps **6** - **14** to pattern the ANA wide channels and other surrounding microfluidic channels. The stepper mask III is used.

? TROUBLESHOOTING

28 | Etch PECVD oxide through the exposed area using CHF_3/CF/Ar plasma. The oxide etch rate is about 3.5 nm/s using the oxide-etch recipe listed below.
Gas: CHF_3 (45 sccm), CF_4 (15 sccm), Ar (100 sccm)
Pressure: 100 mTorr
RF Power: 200 W
Etch rate: 3.5 nm/s

29 | Repeat Steps **15** - **17** to etch the nitride layer, strip the photoresist, and measure the etch depth with the surface profilometer to ensure both the oxide and nitride layers etched through.

30 | Etch the wafer with the DRIE machine for the ANA wide channels. The etch rate is about 1.47 µm/min using the SiDRIE-etch recipe listed below. Measure the silicon etch depth with the surface profilometer.

	Etch mode	Passivation mode
Process time:	6 s	4.5 s
Overrun:	0.5 s	0 s
Platen generator power:	80 W	60 W
Coil generator power:	600 W	600 W
Gas:	SF_6 (70 sccm)	C_4F_8 (35 sccm)
Etch rate:	1.47 µm/min	N/A

▲ CRITICAL STEP The Bosch process used in the DRIE etching should end with the SF_6 etching cycle. The SiDRIE-etch recipe listed above is well-characterized with a minimum side-wall roughness and a near-vertical etch profiles. The DRIE Si etch depth should be equal to the ANA narrow channel depth.

? TROUBLESHOOTING

31 | Run O_2 plasma with the O_2 plasma Asher to clean the wafer for at least 4 hours.
Gas: O_2 (45 sccm)
Pressure: 100 mTorr
RF Power: 200 W
Time: 240 min

▲ **CRITICAL STEP** Step **31** is critical to remove the Teflon-like polymer layer left after the DRIE Bosch process.

32 | Clean the wafer with the piranha solution for 10 min, dump rinse the wafer with DI water for 10 min, and spin dry the wafer.

33 | Immerse the wafer in the concentrated HF solution (49% HF) for 2 hours to strip both the oxide and the nitride layer, dump rinse the wafer with DI water for 10 min, and spin dry the wafer. The nitride etch rate in HF is about 200 nm/hour.

34 | Inspect the wafer with SEM and measure the widths of the ANA narrow and wide channels.

▲ **CRITICAL STEP** Besides checking the uniformity of the DRIE etching profile, this step is critical to determine the desired thickness of the thermal oxide to be grown in Step **36**.

35 | Repeat from Step **1** to Step **3** RCA clean the wafer before thermal oxidation.

36 | Thermally grow an oxide layer with an appropriate thickness in an atmosphere furnace to provide an electrical isolation between the conductive Si substrate and buffer solution.

Gas: H_2 (5 sccm), O_2 (10 sccm)

Pressure: 1 atm

Temperature: 1000 ^{o}C

37 | Repeat Step **34** to determine the final gap sizes of the ANA narrow and wide channels.

? TROUBLESHOOTING

Fabrication of buffer access holes ● TIMING 1~2 d

38 | Repeat Step **26** to deposit a thick layer of oxide (~ 6 µm) on the wafer using the PECVD system.

39 | Repeat from Steps **6** to **13** to pattern the photoresist for buffer access holes. Spin coat a thick layer of AZ4620 photoresist (~ 10 µm) instead of the thin Shipley SPR700-1.0 photoresist. The chrome photomask IV with the access holes is used.

40 | Repeat Step **28** to etch the PECVD oxide. The etch time is controlled to ensure the buffer access holes are open.

▲ **CRITICAL STEP** The etch time should be well controlled so that the holes are completely open and have connection with other channels. In addition, if the wafer is over etched, silicon surface in some areas will be exposed, which will cause current leakage in the separation experiment.

41 | Repeat Step **31** to strip photoresist and clean the wafer with Asher for over 4 hours.

42 | Cut the wafer with diesaw into the individual ANA devices. The final ANA device has a dimension of about 25 mm by 40 mm.

Troubleshooting advice can be found in Table I.

Table I| Troubleshooting table.

STEP	PROBLEM	POSSIBLE REASON	SOLUTION
23	It is hard to determine the real (111) planes	• Nitride mask layer is not completely open. • KOH etching is either too short or too long to distinguish the level of undercuts between adjacent lines. • The real (111) planes are far off from the wafer flat (111) plane so that it is beyond the detection limitation of the alignment mark.	• The thickness of the nitride film and the RIE etch rate for nitride need to be carefully characterized to ensure the nitride layer etched through. • Carefully adjust KOH etching time. • The wafer should be positioned properly during photolithography. Pay attention to wafer specifications and make sure the alignment mark can account for the offset between the real (111) plane and wafer flat orientation.
25	Irregular trenches (*e.g.*, non-uniform width or depth) for the ANA narrow regions are generated after KOH etching	• The mask pattern is not well reproduced during photolithography. • There is a thin layer of native oxide on the wafer that prevents KOH etching. • KOH etching conditions are not set right. • The alignment process to find the real (111) planes is not successful.	• The exposure dose and development time need to be carefully characterized empirically. • Quickly dip the wafer into diluted HF solution (DI:HF=50:1) for 30 s to remove native oxide on the wafer. • Double check the temperature and concentration of the KOH solution. • Double check the alignment process.
27	The spin-coated photoresist can not uniformly cover the wafer	• The ANA deep trenches are not completely sealed by PECVD deposited oxide.	• Strip the photoresist and deposit additional oxide layer to ensure complete sealing.
30	DRIE etching doesn't reproduce the features on the mask with good	• Severe undercuts occur during DRIE process. • The etch mask is etched away during DRIE process.	• Double check the DRIE etch recipe. If necessary, adjust the etching parameters for minimized undercuts. • Use a thicker layer of resist or

	fidelity		oxide mask if very deep Si etching is desired.
37	The final gap size of the ANA narrow regions is not as desired (either too small or too large)	• Thickness of the thermal oxide layer is not accurate. • Depth of the ANA wide channels is different from of the ANA narrow channels. • Nitride mask layer is not completely removed, or there is some Teflon-like polymer left in the deep trenches after the DRIE process.	• Double check thermal oxidation conditions such as temperature, time, and gas flows. Run thermal oxidation again if more oxide is desired. • Take cross-sectional SEM of the ANA device to make sure the depths of the ANA narrow and wide regions are the same. Otherwise, further adjustment of the respective etching time is required. • Immerse the wafer in the HF solution for a longer period to strip the nitride mask layer. Run oxygen plasma for a longer time to remove the polymer layer.

Bibliography

1. Y. Shen, R. D. Smith, *Electrophoresis* **23**, 3106 (2002).
2. S. W. Tam, J. Pirro, D. Hinerfeld, *Expert Rev. Proteomics* **1**, 411 (2004).
3. A. Görg, W. Weiss, M. J. Dunn, *Proteomics* **4**, 3665 (2004).
4. K. S. Lilley, A. Razzaq, P. Dupree, *Current Opinion in Chemical Biology* **6**, 46 (2002).
5. T. Rabilloud, *Proteomics* **2**, 3 (2002).
6. I. D. P. Steven P. Dixon, David Perrett,, *Biomedical Chromatography* **20**, 508 (2006).
7. R. D. Smith, *Trends in Biotechnology* **20**, s3 (2002).
8. P. Gebauer, P. Bocek, *Electrophoresis* **23**, 3858 (2002).
9. N. Gottschlich, S. C. Jacobson, C. T. Culbertson, J. M. Ramsey, *Anal. Chem.* **73**, 2669 (2001).
10. N. A. Guzman, T. Blanc, T. M. Phillips, *Electrophoresis* **29**, 3259 (2008).
11. D. A. W. D.A. Wells, *Liquid Chromatogr. Gas chromatogr.* **21**, 522 (2003).
12. D. R. Reyes, D. Iossifidis, P.-A. Auroux, A. Manz, *Anal. Chem.* **74**, 2623 (2002).
13. P.-A. Auroux, D. Iossifidis, D. R. Reyes, A. Manz, *Anal. Chem.* **74**, 2637 (2002).
14. T. Vilkner, D. Janasek, A. Manz, *Anal. Chem.* **76**, 3373 (2004).
15. J. Han, A. K. Singh, *J. Chromatogr. A* **1049**, 205 (2004).
16. S. Yao *et al.*, *Proc. Natl. Acad. Sci. U. S. A.* **96**, 5372 (1999).
17. N. Chiem, D. J. Harrison, *Anal. Chem.* **69**, 373 (1997).
18. D. J. Harrison *et al.*, *Science* **261**, 895 (1993).
19. Y. Zeng, H. Chen, D. W. Pang, Z. L. Wang, J. K. Cheng, *Anal. Chem.* **74**, 2441 (MAY 15, 2002).
20. R. D. Oleschuk, L. L. Shultz-Lockyear, Y. Ning, D. J. Harrison, *Anal. Chem.* **72**, 585 (2000).
21. D. J. Throckmorton, T. J. Shepodd, A. K. Singh, *Anal. Chem.* **74**, 784 (FEB 15, 2002).
22. C. Yu, F. Svec, J. M. J. Frechet, *Electrophoresis* **21**, 120 (2000).
23. R. S. Foote, J. Khandurina, S. C. Jacobson, J. M. Ramsey, *Anal. Chem.* **77**, 57 (2005).
24. J. Lichtenberg, E. Verpoorte, N. F. d. Rooij, *Electrophoresis* **22**, 258 (2001).
25. C. Yu, M. H. Davey, F. Svec, J. M. J. Frechet, *Anal. Chem.* **73**, 5088 (2001).
26. A. V. Hatch, A. E. Herr, D. J. Throckmorton, J. S. Brennan, A. K. Singh, *Anal. Chem.* **78**, 4976 (2006).
27. B. S. Broyles, S. C. Jacobson, J. M. Ramsey, *Anal. Chem.* **75**, 2761 (2003).
28. T. Thorsen, S. J. Maerkl, S. R. Quake, *Science* **298**, 580 (October 18, 2002, 2002).
29. J. C. T. Eijkel, A. van den Berg, *Lab Chip* **6**, 19 (2006).
30. J. Fu, P. Mao, J. Han, *Trends in Biotechnology* **26**, 311 (2008).
31. J. Han, J. Fu, R. B. Schoch, *Lab Chip* **8**, 23 (2008).
32. L. R. Huang, E. C. Cox, R. H. Austin, J. C. Sturm, *Science* **304**, 987 (2004).
33. J. Fu, R. B. Schoch, A. L. Stevens, S. R. Tannenbaum, J. Han, *Nature Nanotechnology* **2**, 121 (2007).
34. Y. Chen, A. Pépin, *Electrophoresis* **22**, 187 (2001).
35. P. Abgrall, N. T. Nguyen, *Anal. Chem.* **80**, 2326 (2008).
36. P. Apel, *Radiation Measurements* **34**, 559 (2001).

37. S. W. Turner, A. M. Perez, A. Lopez, H. G. Craighead, *jvst B* **16**, 3835 (1998).
38. R. H. Austin, J. O. Tegenfeldt, H. Cao, S. Y. Chou, E. C. Cox, *IEEE Transactions On Nanotechnology* **1**, 12 (2002).
39. J. Han, H. G. Craighead, *J. Vac. Sci. Technol., A* **17**, 2142 (1999).
40. P. Mao, J. Han, *Lab Chip* **5**, 837 (Aug, 2005).
41. Y. Zeng, D. J. Harrison, *Anal. Chem.* **79**, 2289 (2007).
42. H. D. Tong *et al.*, *Nano Lett.* **4**, 283 (2004).
43. C. C. Striemer, T. R. Gaborski, J. L. McGrath, P. M. Fauchet, *Nature* **445**, 749 (2007).
44. D. L. Kendall, *Appl. Phys. Lett.* **26**, 195 (1975).
45. Y. Uenishi, M. Tsugai, M. Mehregany, *J. Micromech. Microeng.* **5**, 305 (1995).
46. A. Hölke, H. T. Henderson, *J. Micromech. Microeng.* **9**, 51 (1999).
47. D. R. Ciarlo, *J. Micromech. Microeng.* **2**, 10 (1992).
48. D. L. Kendall, *Annual Reviews of Materials Science* **9**, 373 (1979).
49. M. Madou, *Fundamentals of microfabrication*. (CRC Press, Boca Raton, Florida, 1997).
50. G. Barillaro, A. Nannini, M. Piotto, *Sensors and Actuators A* **102**, 195 (2002).
51. V. Lehmann, H. Föll, *J. Electrochem. Soc.* **137**, 653 (1990).
52. V. Lehmann, U. Grüning, *Thin Solid Films* **297**, 13 (1997).
53. S. E. Létant, T. W. v. Buuren, L. J. Terminello, *Nano Lett.* **4**, 1705 (2004).
54. S. H. G. Teo, A. Q. Liu, J. Singh, M. B. Yu, *J. Vac. Sci. Technol. B* **22**, 2640 (2004).
55. C. Chang *et al.*, *J. Micromech. Microeng.* **15**, 580 (2005).
56. K. B. Mogensen, F. Eriksson, R. P. H. Nikolajsen, O. Gustafsson, J. O. Kutter, paper presented at the Proceedings of the microTAS 2004 symposium, Malmö, Sweden, 2004.
57. P. Mao, J. Han, *Lab Chip* **9**, 586 (2009).
58. P. Mao, S.M., Massachusetts Institute of Technology (2005).
59. J. Fu, P. Mao, J. Han, *Appl. Phys. Lett.* **87**, 263902 (2005).
60. K. Ohwada, Y. Negoro, Y. Konaka, T. Oguchi, *Sensors and Actuators A* **50**, 93 (1995).
61. M. Uematsu *et al.*, *Solid-state Electronics* **48**, 1073 (2004).
62. D.-b. Kao, J. P. McVittie, W. D. Nix, K. C. Saraswat, *IEEE Trans. Electron Devices* **ED-35**, 25 (1988).
63. D.-b. Kao, J. P. McVittie, W. D. Nix, K. C. Saraswat, *IEEE Trans. Electron Devices* **ED-34**, 1008 (1987).
64. H. Heidemeyer *et al.*, *J. Appl. Phys.* **87**, 4580 (2000).
65. H. Jiang, K. Yoo, J.-L. A. Yeh, Z. Li, N. C. Tien, *J. Micromech. Microeng.* **12**, 87 (2002).
66. Y.-C. Wang, A. L. Stevens, J. Han, *Anal. Chem.* **77**, 4293 (2005).
67. R. Mukhopadhyay, *Anal. Chem.* **78**, 7379 (2006).
68. J. H. Lee, S. Chung, S. J. Kim, J. Han, *Anal. Chem.* **79**, 6868 (2007).
69. M. Knez, K. Nielsch, L. Niinistö, *Adv. Mater.* **19**, 3425 (2007).
70. J. Han, H. G. Craighead, *Science* **288**, 1026 (2000).
71. W. M. Deen, *AIChE Journal* **33**, 1409 (1987).
72. J. L. Viovy, *Rev. Mod. Phys.* **72**, 813 (2000).
73. J. Han, S. W. Turner, H. G. Craighead, *Phys. Rev. Lett.* **83**, 1688 (1999).

74. L. R. Huang *et al.*, *Nature Biotechnology* **20**, 1048 (2002).
75. L. R. Huang *et al.*, in *Electron Devices Meeting, 2001. IEDM Technical Digest. International*. (2001), pp. 363-366.
76. J. C. Giddings, *Unified Separation Science*. (John Wiley & Sons, Inc, New York, NY, 1991).
77. J. Han, H. G. Craighead, *Anal. Chem.* **74**, 394 (2002).
78. F. Tessier, J. Labrie, G. W. Slater, *Macromolecules* **35**, 4791 (2002).
79. J. Han, Ph. D thesis, Cornell University (2001).
80. Z. R. Li *et al.*, *Anal. Bioanal. Chem.* **394**, 427 (2009).
81. N. Pamme, *Lab On a Chip* **7**, 1644 (2007).
82. G. Decher, J. B. Schlenoff, *Multilayer Thin Films: Sequential Assembly of Nanocomposite Materials*. (Wiley-VCH Verlag GmbH & Co, Weinheim, 2003).
83. D. Lee, Ph.D, Massachusetts Institute of Technology (2007).
84. J. Rzayev, M. A. Hillmyer, *J. Am. Chem. Soc* **127**, 13373 (2005).
85. K. Ariga, J. P. Hill, Q. Ji, *Phys. Chem. Chem. Phys.* **9**, (2007).
86. E. N. Savariar, K. Krishnamoorthy, S. Thayumanavan, *Nature Nanotechnology* **3**, 112 (2008).
87. Z. Liang, A. S. Susha, A. Yu, F. Caruso, *Adv. Mater.* **15**, 1849 (2003).
88. H. Alem, F. Blondeau, K. Glinel, S. Demoustier-Champagne, A. M. Jonas, *Macromolecules* **40**, 3366 (2007).
89. D. Lee, A. J. Nolte, A. L. Kunz, M. F. Rubner, R. E. Cohen, *J. Am. Chem. Soc* **128**, 8521 (2006).
90. A. C. Arsenault *et al.*, *Langmuir* **21**, 499 (2005).
91. Y. Wang, F. Caruso, *Chem. Mater.* **18**, 4089 (2006).
92. D. Lee, R. E. Cohen, M. F. Rubner, *Langmuir* **23**, 123 (2007).
93. R. B. Schoch, J. Han, P. Renaud, *Reviews of Modern Physics* **80**, 839 (2008).
94. D. Stein, M. Kruithof, C. Dekker, *Physical Review Letters* **93**, 035901 (2004).
95. M. F. Durstock, M. F. Rubner, *Langmuir* **17**, 7865 (2001).
96. M. R. Bohmer, O. A. Evers, J. M. H. M. Scheutjens, *Macromolecules* **23**, 2288 (1990).
97. S. J. Kim, Y.-C. Wang, J. H. Lee, H. Jang, J. Han, *Physical Review Letters* **99**, 044501 (2007).
98. S. T. Dubas, J. B. Schlenoff, *Langmuir* **17**, 7725 (2001).
99. H. Mohamed *et al.*, *IEEE Transactions On Nanobioscience* **3**, 251 (2004).
100. J. A. Davis *et al.*, *PNAS* **103**, 14779 (2006).